MODE- AND WAVELENGTH-DIVISION MULTIPLEXING IN SILICON INTEGRATED PHOTONICS

A Dissertation

Presented to the Faculty of the Graduate School

of Cornell University

in Partial Fulfillment of the Requirements for the Degree of

Doctor of Philosophy

by

Lian Wee Luo

August 2013

MODE- AND WAVELENGTH-DIVISION MULTIPLEXING IN SILICON INTEGRATED PHOTONICS

Lian Wee Luo, Ph.D.

Cornell University 2013

Significant effort in optical-fiber research has been directed in the past few years towards creation of mode-division multiplexing on fiber platforms to further scale the communication bandwidth transmitted per fiber. At the world's leading global conference for optical communications (i.e. Optical Fiber Communication Conference), mode-division multiplexing (MDM) has been one of the hottest topic in the recent years depicted by the large amount of contributed and invited talks in this field. David Richardson et al. [Nature Photonics May 2013] wrote a review letter to discuss the importance of space-division multiplexing in optical fibers to meet the increasing transmission capacity demand.

In contrast, current integrated photonics operate almost exclusively in the single-mode regime and typically utilize wavelength-division multiplexing (WDM) alone. MDM is rarely considered to be implemented in integrated photonics due to several challenges. The challenges include creating mode (de)multiplexers with low modal crosstalk and loss and concurrently support WDM (a key feature of many integrated-optics interconnect designs).

Here in this dissertation we show the first demonstration of simultaneous mode- and wavelength-division multiplexing with low modal crosstalk and low loss in integrated photonics. Our approach would potentially increase the aggregate data rate for on-chip ultra-high bandwidth communications.

We first start off with the discussion of the current status of the data traf-

fic demand by the consumers and why there is a need for silicon photonics to meet this demand. We then propose a new silicon waveguide technique to improve the optical loss of silicon waveguides. We make use of this fabrication technique in fabricating high-quality factor microring resonators. We also investigate the nonlinear effects in microring resonators. Acquiring this knowledge about the nonlinear effects in microring resonators, we can engineer the microring resonators design to suit the needs of our system. We utilize add-drop microring filters as the (de)multiplexers in the wavelength-division multiplexing platform. We also introduce an interleaver based on triple-microring integrated with Mach-Zehnder interferometer to separate a comb of closely located channels. The highlight of the dissertation is to discuss how we can implement mode-division multiplexing simultaneously with wavelength-division multiplexing in integrated photonics. Finally we propose a future work for a truly integration of on-chip multiplexing system.

BIOGRAPHICAL SKETCH

Lian Wee Luo was born in Singapore and spent most of his life in Singapore except for the past five years. He graduated from high school in 1999 and before he can embark his studies in the university, he had to serve in the national service for two and a half years. That was a tough period but the experience was valuable in building him up to face the challenges in life. He was admitted to Nanyang Technological University for his bachelor degree in Electrical and Electronic Engineering. He met many close friends and great mentors during the four years there. He spent the last two years of the undergraduate working on optical fibers research. That was his first experience with photonics. Subsequently after graduation from the univeristy, he decided to try out working in research institute but chose to do research in the field of Bio-MEMS instead so as to acquire a different research perspective. Again the relationship with the colleagues there made his one and a half years there a valuable one. He took up a scholarship awarded by Agency for Science, Technology and Research (A*STAR) to go to Cornell to do his PhD degree. He decided to go back to do research in Photonics and was blessed to join the Cornell Nanophotonics Group led by Professor Michal Lipson. It is a great team and the work environment is good and harmonious. Most of all, Professor Michal Lipson brings out the best of everyone. Under the supervision of Professor Michal Lipson, Lian Wee worked on the integration of different multiplexing systems in silicon integrated photonics.

To my family and wife, Yih Lin, for their constant support and unwavering love.

ACKNOWLEDGEMENTS

The five years in Ithaca have been wonderful and it definitely leaves an important footprint in my life. I feel indebted to many people and no matter how much thanksgivings I write here can hardly describe my gratitude to them.

First of all, I want to thank my advisor, Prof. Michal Lipson, for all the guidance and support that she has given me throughout the years. She is very approachable and supportive that I always feel energized and motivated after each meeting with her. She is definitely one of the reasons why I enjoy my five years of my PhD degree. I am impressed with her energy; she travels a lot for business trips but she can still meet with every single of us the immediate day she comes back. She also creates a good work environment for us so that there is constant discussion among the group-mates.

I also want to thank the other two members of my committee, Prof. Edwin Kan and Prof. Alexander Gaeta. Edwin is my mentor in both academically and personally. He has given much valuable advice that I need during this five years. I am grateful for his care and concern towards me. Alex is a great teacher and mentor. I learnt a lot of valuable knowledge from his class at AEP and also enjoy talking to him during the group get-together. He is very approachable personally. I also want to thank other great teachers in Cornell, in particularly Prof. Fahan Rana and Prof. Frank Wise, for their insightful lectures.

I would like to thank all the members (alumni, current) of Cornell Nanophotonics Group. They are a group of wonderful and brillant people. They have made my time in the group to be a wonderful period. Their presence have made the work environment friendly and colorful. These members include Dr. Carl Poitras, Dr Jaime Cardenas, Dr. Mohammad Soltani, Dr. Sasha Gondarenko, Dr. Danilo Spadoti, Dr. Bernado Kyotoku, Prof. Amy Turner-Foster, Prof. Gus-

tavo Wiederhecker, Dr. Art Nitkowski, Prof. Michael Mernard, Dr. Jake Levy, Dr. Kyle Preston, Dr. Nicholas Sherwood, Dr. Hugo Lira, Dr. Lucas Gabrielli, Debo Olaosebikan, Taige Hou, Biswajeet Guha, Mian Zhang, Yoon Ho Daniel Lee, Shreyas Shah, Lawrence Tzuang, Kevin Luke, Austin Griffith, Avit Dutt, Aseema Mohanti, Chris Phare, Steven Miller and the list goes on. I believe that this group will continue to grow and stay as a prominent contributor in the field of photonics.

In particularly, I would like to thank Prof. Gustavo Wiederhecker for his help and guidance during his three years in Cornell. I had the honor of sitting beside him throughout the three years and he always offers his help in my research whenever I meet an obstacle. I am also indebted by other Brazilians in the group; Dr Hugo Lira and Dr. Lucas Gabrielli offered their knowledge in coding and fabrication.

I have also collaborated with several of Prof. Keren Bergman's students at Columbia University, namely Dr. Noam Ophir, Christine Tan, Kishore Padmaraju, Atiyah Ahsan, Lee Zhu, Michael Wang and Qi Li. I had acquired much knowledge from them in testing my device and setting up experiments in the lab.

My research was funded in part by the U.S. Air Force (AFOSR) program FA9550-09-1-0704 on "Robust and Complex on-chip Nanophotonics" supervised by Dr. Gernot Pomrenke, support from DARPA for award #W911NF-11-1-0435 supervised by Dr. Jagdeep Shah, and by the National Science Foundation under Grant No. 1143893. This work was supported in part by the NSF through CIAN ERC under Grant EEC-0812072, the NSF and Semiconductor Research Corporation under grant ECCS-0903406 SRC Task 2001 and was performed in part at the Cornell NanoScale Facility, a member of the National Nanotechnol-

ogy Infrastructure Network, which is supported by the NSF. I personally also acknowledge a fellowship from Agency of Science, Technology and Research (A*STAR), Singapore that supports the five years of my PhD program in Cornell.

TABLE OF CONTENTS

Biographical Sketch . . . iii
Dedication . . . iv
Acknowledgements . . . v
Table of Contents . . . viii
List of Figures . . . x

1 Introduction and background **1**
1.1 Meeting the exponentially increasing data traffic demand . . . 1
1.2 Silicon photonics for on-chip interconnects . . . 5
1.3 Focus and organization of this dissertation . . . 6

2 Low-loss etchless silicon waveguides **10**
2.1 Silicon is an excellent material for waveguiding . . . 10
2.2 Background of traditional fabricated silicon waveguides . . . 11
2.3 Proposed etchless silicon waveguide fabrication to reduce the scattering and absorption loss . . . 13

3 High-quality factor etchless silicon microring resonators **16**
3.1 Microring resonators . . . 16
3.2 Etchless silicon photonic microring resonators . . . 20
3.2.1 Designing etchless silicon photonic microring resonators . 21
3.2.2 Fabricating etchless silicon photonic microring resonators 21
3.2.3 Results and discussions . . . 23
3.2.4 Conclusion . . . 25

4 Nonlinear Effects in Microring Resonators **27**
4.1 Introduction . . . 27
4.2 Relationship between the FCD blue shift and the TO red shift of the resonance . . . 30
4.3 Nonlinear measurements of the fabricated etchless silicon microring resonator . . . 31
4.4 Engineering the nonlinear resonance shift of the etchless silicon microring . . . 34
4.5 Conclusion . . . 35

5 On-chip Wavelength-Division Multiplexing **37**
5.1 Introduction . . . 37
5.2 WDM microring-based add-drop Demultiplexers . . . 38
5.2.1 Microring-based add-drop filter . . . 38
5.2.2 WDM demultiplexer design . . . 40
5.2.3 WDM demultiplexer fabrication . . . 42
5.2.4 WDM demultiplexer measurements and discussions . . . 42
5.3 On-chip Silicon Interleaver . . . 44

5.3.1 Interleaver design 44
5.3.2 Interleaver fabrication processes 52
5.3.3 Results and discussions 54
5.3.4 Conclusion 57

6 Simultaneous Mode- and Wavelength-Division Multiplexing On-Chip 58
6.1 Introduction 58
6.2 Selective mode coupling by phase matching 59
6.3 Device design and fabrication 61
6.4 Optical modes imaging 63
6.5 Optical crosstalk 64
6.5.1 Crosstalk measurements 64
6.5.2 Minimizing the crosstalk 64
6.6 Mode- and wavelength-division multiplexing link 67
6.6.1 3-Mode × 10-Gb/s multiplexing link 67
6.6.2 2-Mode × 3-Wavelength × 10-Gb/s MDM-WDM link . . . 70
6.7 Conclusion 73

7 Summary and future work 74

Bibliography 77

LIST OF FIGURES

1.1 Peak period traffic composition - North America. Taken from 1H 2013 Global Internet Phenomena Report from Sandvine [1]. . . . 2

1.2 General multiplex scheme: the input optical signals are multiplexed into a single optical medium. The demultiplexer receives the multiplexed data stream and extracts the original channels to be transferred. Figure is modified from a image taken from Wikipedia. 4

1.3 Intel's roadmap on silicon optical interconnects integration. Taken from the presentation by Intel [2]. 9

2.1 Etched silicon waveguide fabrication process flow. (a) Use 250 nm silicon-on-insulator (SOI) as the device layer. (b) Patterning of the waveguides using ma-N 2403 resist, leaving a coupling gap between the ring resonator and bus waveguide. (c) Etching of the silicon layer. (d) Deposition of at least 1.0 µm PECVD silicon dioxide to confine the optical mode. 12

2.2 Scanning electron microscope picture of etched silicon waveguides with simulation of the interaction between the optical waveguide mode and the sidewall of the waveguide. 13

2.3 Etchless silicon photonic ring resonator fabrication process flow. (a) Thermal oxidation of a 500 nm silicon-on-insulator (SOI) to leave behind 140 nm thick silicon layer with 785 nm thick thermally grown oxide on top. (b) Patterning of the waveguides using ma-N 2405 resist, leaving a coupling gap between the ring resonator and bus waveguide. (c) Etching of the thermally grown oxide, leaving behind a thin 50 nm oxide slab. (d) Selective wet thermal oxidation of the silicon. (e) Structural profile of the oxidized silicon waveguides. (f) Deposition of 300 nm HTO and 1.8 µm PECVD silicon dioxide. 15

3.1 An illustration of a waveguide coupled microring resonator. The diagram shows the coupling, κ, and transmission, τ, coefficients for the input and output fields of the device as well as the round-trip loss factor, a. 16

3.2 A simulated transmission spectrum of a critically-coupled silicon microring resonator with a waveguide dimension of 450 nm wide × 250 nm tall and a radius of 20 µm. 19

3.3 (a) SEM picture of the fabricated 50 μm-radius etchless silicon photonic ring resonator. (b) Simulated structural profiles of the etchless silicon ring resonator with coupling gap = 930 nm. (c) Symmetric mode of the bus waveguide and the ring resonator. (d) Cross-sectional SEM picture of the coupling region. (e) Transmission electron microscope (TEM) picture of the thin oxidized silicon slab. 22
3.4 Transverse electric (TE) mode profile (Ex-component) of (a) Etchless silicon waveguide. (b) Etchless silicon inverse nanotaper. . . 24
3.5 (a) Through-port transmission spectrum of the ring resonator in transverse electric (TE) polarization. (b) Normalized transmission spectrum at λ_0 = 1531.416 nm. 26

4.1 Electronic band gap diagram of silicon showing all the absorption and generation mechanisms of photons, phonons, and electrons. The two-photon absorption (TPA) process absorbs photons (which results in TPA loss and degrades the Q) and excites the electrons from the valence band to the conduction band. The phonons takes part in sending the electrons in the conduction band from one state to another state through relaxation process. The generated electrons decrease the refractive index through free carrier dispersion (FCD), and results in a resonance blue shift. The generated carriers also adds free-carrier absorption (FCA) (which degrades the Q). The TPA and FCA nonlinear processes, together with the linear surface absorption at the Si/SiO_2 interface heats the resonator (which results in a resonance red shift). 28
4.2 Measured transmitted power spectrum of a typical microring resonator showing the net red shift of the resonance with increasing laser input power. The laser is swept from shorter wavelength to longer wavelength. 29
4.3 (a) Schematic diagram of the pump-probe setup for the measurement of free carrier lifetime. (b) Transmission spectrum of the etchless microring in quasi-TE polarization with λ_{probe} = 1489.484 nm. (c) Measurement of carrier lifetime. 32
4.4 Measured transmitted power spectrum of the etchless silicon microring resonator showing the net blue shift of the resonance with increasing laser input power (indicated in the inset). The laser is swept from longer wavelength to shorter wavelength. . . 33
4.5 (a) Density plot calculating the resonance shift as a function of thermal resistance and dropped power. (b) Optical microscope picture of the fabricated etchless silicon microring resonator with etched trenches. (c) Schematic diagram of the cross section to illustrate the depth of the trenches (not drawn to scale). 35

4.6 Measured resonance shift power dependence (at $\lambda_0 \approx 1542$ nm) of three different etchless silicon microring resonator devices: one without etched trenches (blue curve), one with just the silicon slab etched (green curve), and one with 300 µm deep trenches (red curve). The schematic insets on the right indicates the corresponding device cross-section, the straight lines connecting the experimental data are guides for the eyes. 36

5.1 WDM demuplexing system proposal using two stages. Interleaver at the DeMux stage to split the densely WDM channels and add-drop microring filters to switch one channel to a desired port. 38
5.2 An illustration of an add-drop microring filter. The diagram shows the coupling, κ, and transmission, τ, coefficients at both coupling regions as well as the round-trip loss factor, a. 39
5.3 A simulated transmission spectrum of a silicon add-drop microring filter with a waveguide dimension of 450 nm wide x 250 nm tall and a radius of 20 µm. 41
5.4 Silicon waveguide with integrated NiCr microheater fabrication process flow. (a) Use 250 nm silicon-on-insulator (SOI) as the device layer. (b) Patterning of the waveguides using ma-N 2403 resist, leaving a coupling gap between the ring resonator and bus waveguide. (c) Etching of the silicon layer. (d) Deposition of 1.0 µm PECVD silicon dioxide to confine the optical mode. (e) Evaporation of 250 nm NiCr on top of the cladding for the integrated microheater. (f) Evaporation of 400 nm Au for the contact wires. 43
5.5 (a) Microscopic image of the 4-channels silicon WDM demultiplexers. (b) SEM image of each individual microring with integrated microheater on top. 44
5.6 (a) Transmission spectrum of the through and drop ports of the demultiplexer. (b) Tuning of the drop port by thermal tuning of the microheater. 45
5.7 Filtering function of an interleaver. (a) Multiplexing and demultiplexing of a comb of WDM signals. (b) Transmission spectra of the interleaver, illustrating the terminologies used in this paper. . 47
5.8 Schematic of ring assisted MZI interleavers. (a) Single ring assisted MZI interleaver. (b) Double ring assisted MZI interleaver. (c) Triple ring assisted MZI interleaver. (d) Calculated cross port transmission spectra of an optimal single ring ($\kappa_1 = 0.89$), optimal double ring ($\kappa_1 = 0.97$, and $\kappa_2 = 0.62$), and optimal triple ring ($\kappa_1 = 0.96$, $\kappa_2 = 0.68$, and $\kappa_3 = 0.25$) assisted MZI interleaver. . . . 49
5.9 Impact of ring loss on the cross port transmission spectra of an optimal triple ring-assisted MZI interleaver. 50

5.10 Triple ring assisted MZI interleaver. (a) Contour plot of the channel crosstalk as a function of κ_1 and κ_2, with the value of κ_3 optimized to be 0.25 for a passband bandwidth requirement of 0.55 *FSR*. (b) Simulated transmission spectra of the interleaver with $\kappa_1 = 0.96$ and $\kappa_2 = 0.68$, indicated by the white cross in the contour plot. (c) $\kappa_1 = 0.8$ and $\kappa_2 = 0.68$, indicated by the black cross. . 51
5.11 Triple ring assisted MZI interleaver. (a) Contour plot of the channel crosstalk as a function of κ_1 and κ_2, with the value of κ_3 optimized to be 0.25 for a passband bandwidth requirement of 0.55 *FSR*. (b) Simulated transmission spectra of the interleaver with $\kappa_1 = 0.96$ and $\kappa_2 = 0.68$, indicated by the white cross in the contour plot. (c) $\kappa_1 = 0.8$ and $\kappa_2 = 0.68$, indicated by the black cross. . 53
5.12 Final fabricated device. (a) Optical microscope picture. (b) Scanning electron microscope (SEM) picture of the racetrack resonator coupled to the arm of the MZI. 54
5.13 Operation of the fabricated device in the ideal coupling regime. (a) Transmission spectra of the bar and cross port. (b) Zoom-in of the section in (a). 56
5.14 Operation of the fabricated device in the non-ideal coupling regime. (a) Transmission spectra of the bar and cross port. (b) Zoom-in of the section in (a). 57

6.1 Phase matching condition for 250 nm tall silicon waveguides. (a) Simulated effective index of the optical modes in waveguide of different widths at $\lambda = 1550$ nm. (b) Selective coupling of the single-mode microrings to a specific spatial mode in the multimode bus waveguide with each section of the multimode waveguide linked by adiabatic tapered waveguides. The insets show the selective coupling of each multiplexer (TE_0, TE_1, and TE_2). 61
6.2 Microscope image of the fabricated device. Inset: SEM showing the heater to tune each individual ring resonator. 62
6.3 Simulated and experimental images of the optical modes at the cross-section of the multimode waveguide. 63
6.4 Optical transmission and crosstalk at the three output ports for signal injection on each of the three input ports. (a) Output port 1. (b) Output port 2. (c) Output port 3. 65

6.5 Coupling strength of different spatial modes (TE_2, TE_1, TE_0) of a 1.41-μm wide waveguide to the TE_0 mode of a 450-nm wide silicon waveguide with a coupling gap of 200 nm. (a) Schematic of the coupling between a 1.41-μm wide waveguide and a 450-nm wide silicon waveguide. (b) Schematic of an add-drop microring with asymmetric input and drop waveguides. (c) The maximum coupling strength of TE1 mode is 0.057. The optimum operating regime for low-crosstalk regime is at $L_{coupling} \approx 6$ μm. 67
6.6 (a) Simulated transmission and crosstalk levels at output port 3 with optimized coupling length of 6 μm. Similar transmission curves for outputs 1 and 2 are expected for optimized coupling lengths of 4 μm and 4.5 μm, with simulated crosstalks <-30 dB and <-25 dB respectively. (b) Coupling strength of different spatial modes (TE_2, TE_1, TE_0) of a 1.41-μm wide waveguide to the TE_0 mode of a 450-nm wide silicon waveguide with a coupling gap of 280 nm. The maximum coupling strength of TE_1 mode is 0.037. The optimum operating regime for low-crosstalk regime is at $L_{coupling} \approx 11$ μm. 68
6.7 3-Mode × 10-Gb/s Multiplexing Link. (a) Experimental setup for performance evaluation including Pulsed Pattern Generator (PPG), Tunable Laser (TL), Amplitude Modulator (AM), Phase Modulator (PM), Erbium-Doped Fiber Amplifier (EDFA), Isolator (→), Standard Single Mode Fiber (SSMF), Tunable Filter (λ), Digital-Communications Analyzer (DCA), Variable Optical Attenuator (VOA), Avalanche-Photodiode (APD-TIA), Limiting Amplifier (LA), and Bit-Error-Rate Tester (BERT). (b) BER measurements for back-to-back (B2B) test case, single port transmission, and MDM operation for all 3 ports. (c) Corresponding eye-diagrams for the inspected signals. 71
6.8 2-Mode × 3-Wavelength × 10-Gb/s MDM-WDM link. (a) Experimental setup for demonstrating combined MDM and WDM operation. (b) BER measurements for back-to-back (B2B) test cases and full MDM-WDM operation for both ports. (c) Corresponding eye-diagrams for the inspected signals. 72

7.1 To integrate WDM microring modulators and MDM multiplexers on the same chip. 76

CHAPTER 1

INTRODUCTION AND BACKGROUND

1.1 Meeting the exponentially increasing data traffic demand

Since the birth of internet in 1980s, the amount of data traffic has increased tremendously. The expansion of broadband wired internet access has introduced many new ways to share video, stream or even real-time stream television and movies, and connect people together through voice and video calls. In the more recent years, wireless and cellular data usage on mobile devices has grown rapidly to bring forth video streaming and teleconferencing. According to the global internet phenomena report compiled by Sandvine (Intelligent Broadband Networks), real-time entertainment (comprised of streaming video and audio) continues to be the largest data traffic contributor [1]. Sandvine expects that its rapid growth will continue with the emergence of longer and high-quality video on all networks globally. In North America, real-time entertainment domainates mainly due to the continued market leadership of Netflix, which accounts for about a third of peak downstream traffic on fixed networks and has seen its share on mobile networks double in 2012 (see Figure 1.1). In other regions of the world, YouTube continues to be the largest single source of real-time entertainment traffic on both fixed and mobile access networks.

To meet the exponentially increasing data traffic demand, the continuation of Moore's Law has resulted in the computing systems with exponentially increasing computational power. Microelectronics has been technologically important since the 1960s. As the name Microelectronics implies, transistors used in microelectronic chips are on the order of a micrometer in size. As predicted

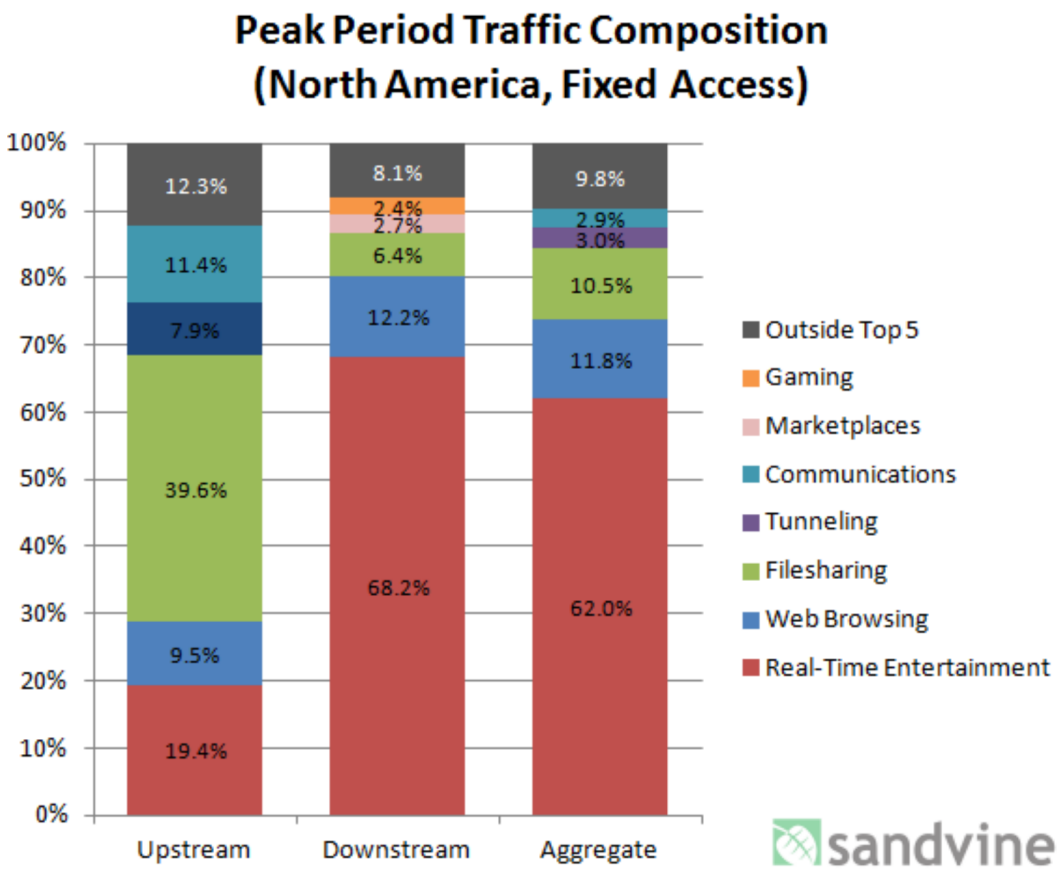

Figure 1.1: Peak period traffic composition - North America. Taken from 1H 2013 Global Internet Phenomena Report from Sandvine [1].

by Moore's law, transistor technology has continued to shrink over the decades; passing into submicron and heading towards the nanometer regime. Small size brings many advantages, namely high packing density, high circuit speed and low power dissipation. However miniaturization of microelectronics is reaching a fundamental limit where the gate of the tranisistors is already only a few atoms thick [3]. This means that at some point it will be tough or even impossible to bring microprocessors closer to each other to avoid the high intrinsic losses of high frequency electrical signals propagating through metallic wires [4].

Optical interconnects in contrast can provide much larger bandwidth without significant loss of signals. The optical links have very broad transparency windows; bandwidth over tens of tera-hertz (THz) is readily available for data transmission. Moreover the loss of the optical links is low even at high frequency; therefore less power is being wasted during the operation and transmission. The bandwidth of a single optical signal is limited to a few tens of giga-hertz (GHz) by the signal conversions between the electrical and optical domains as determined by the speed of modulators and detectors [5,6].

With the limitations set by the modulators and detectors, multiplexing can be employed to further increase the aggregate bandwidth of the optical interconnects. Multiplexing is a method by which multiple data streams are combined into one signal over a shared medium (Figure 1.2). The multiplexed signal is transmitted over a communication medium. The multiplexing increases the aggregate bandwidth by dividing the capacity of the multiplexed channel into many slower channels, one for each individual signal stream ot be transferred. The mutliplexer is a device that does the multiplexing operation while the demutltiplexer is a device that extracts each original channels.

There are several types of mutliplexing technologies being employed by optical communications: space-division multiplexing (SDM), wavelength-division multiplexing (WDM), time-division multiplexing (TDM), and code-divison multiplexing. WDM is traditionally and widely used in optical communications to fully utilize the entire available optical spectrum. More recently, significant effort in optical-fiber research has been directed towards creation of mode-division multiplexing (MDM) fiber platforms to further scale the communication bandwidth transmitted per fiber. At the world's leading global con-

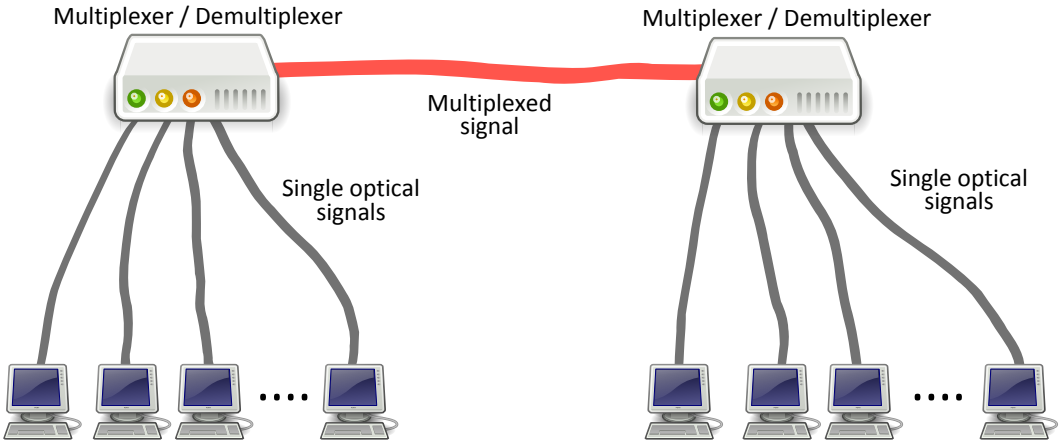

Figure 1.2: General multiplex scheme: the input optical signals are multiplexed into a single optical medium. The demultiplexer receives the multiplexed data stream and extracts the original channels to be transferred. Figure is modified from a image taken from Wikipedia.

ference for optical communications (i.e. Optical Fiber Communication Conference), MDM has been one of the hottest topic in the recent years depicted by the large amount of contributed and invited talks in this field. David Richardson et al. wrote a review letter to discuss the importance of mode-division multiplexing in optical fibers to meet the increasing transmission capacity demand [7].

In contrast, current integrated photonics operate almost exclusively in the single-mode regime and typically utilize wavelength-division multiplexing (WDM) alone. The implementation of simultaneous mode- and wavelength-division multiplexing in integrated photonics would potentially increase the aggregate data rate for on-chip and chip-to-chip ultra-high bandwidth communications.

1.2 Silicon photonics for on-chip interconnects

High speed optical interconnects are seen as a promising way forward to meet the increasing bandwidth demand and silicon photonics is seen as a good platform to integrate both electronic and optical componenets on the same silicon chip [8]. Different on-chip components are needed for the full integration of optical interconnects on-chip. Figure 1.3 shows the roadmap of silicon photonics integration laid out by Intel [2]. It had already been proven that silicon is a good optical material at high frequency of 40 Gbps. Firstly, an on-chip laser source is required; one possible device is the hybrid silicon laser where the silicon is bonded to a different lasing medium semiconductor (such as AlGaInAs) [9]. Another possible approach is to use all-silicon Raman laser in which the silicon itself acts as the lasing medium [10]. Modulators are needed to modulate the light to carry the data in the form of optical pulses. 40 Gbps modulators on silicon based on carrier depletion of a pn diode embedded inside a silicon-on-insulator waveguide had been demonstrated [10]. Next the many optical signals are (de)multiplexed and routed to a specific receiving end on the chip (or on a different chip) and detected by a photodetector. The photodetector converts the signals from optical domain to electrical domain and is mainly demonstrated on the silicon-germanium platform [6].

The next step on the roadmap is to integrate the different silicon devices into hybrid modules on the same chip with the multiplexing scheme being employed for ultra-high bandwidth applications. Current integrated photonics operate almost exclusively in the single-mode regime and utilize wavelength-division multiplexing (WDM) alone which supports a limited scalability in bandwidth density.

The work in this thesis proposes a hybrid multiplexing scheme which allows simultaneous mode- and wavelength-division multiplexing on-chip. This thesis demonstrates different multiplexing designs to improve on the existing WDM platform and further scale the bandwidth for high bandwidth on-chip and chip-to-chip applications.

1.3 Focus and organization of this dissertation

In this introductory chapter we present the exponential increasing data bandwidth demand as predicted by Moore's Law. We also discuss why electrical interconnects are facing a challenge to meet this demand. This is why silicon optical interconnects are introduced about a decade ago to resolve this electrical bottleneck.

In chapter two we discuss why silicon is an excellent material to be implemented for optical interconnect devices. Many groups have been trying to bring down the optical losses of silicon but there seem to be a lower bound limit. We introduce a new fabrication method of making silicon waveguides without any actual etching of the silicon layer. We define the waveguides by selective oxidation of the silicon layer which is a common fabrication technique used in CMOS industries (known as Local Oxidation of Silicon, LOCOS). Using this technique, we show how we can further reduce the optical losses (mainly scattering and absorption losses).

In chapter three we explain the theoretical background of microring resonators. The microrings are compact, tunable, and consumes low power. Due to these properties, microring-based devices will reduce power, footprint and cost.

We also formulate the fundamental electric fields in microrings and illustrate the few basic properties of microrings that we use in the rest of this dissertation. We make use of this etchless silicon method to fabricate microring resonators. Due to the low optical loss achieved by this fabrication technique, we demonstrate high quality factor silicon microring resonators. We show the full design steps of this etchless silicon microring resonators.

In chapter four we investigate about the nonlinear effects in microring resonators. We discuss about the counteracting interplay between two main nonlinear process (i.e. free carrier dispersion blue shift and thermo-optic red shift). In the high-Q etchless silicon microring resonators, we observe atypical blue resonance shift even at very low powers. We also measure the free carrier lifetime in these etchless silicon waveguides using the phenomenon of carrier generation by two-photon absorption. Due to the counteracting interplay of free carrier dispersion and thermo-optic effect, we show how we can engineer these two processes to fabricate a device which is either dominated by free carrier dispersion blue shift, or thermo-optic red shift or reduced-senstivity to resonance shift with power.

In chapter five we propose a wavelength-division multiplexing scheme that makes use of an efficient interleaver to split a comb of WDM channels into two paths and a simpler microring-based demultiplexers to route each WDM channel to a specific receiving end. In particularly, we design a 4-channels mircoring-based demultiplexer with low crosstalk, low power consumption. As for the interleaver, we design a highly-efficient triple-microring Mach-Zehnder interferometer with full reconfiguration capability. It has a flat passband and a rapid roll-off slope which in turn enables low crosstalk.

In chapter six we show the first demonstration of simultaneous mode- and wavelength-division multiplexing in integrated photonics. We explain why integrated photonics has traditionally used single-mode in the operation and avoided the use of higher order modes. In this work, we demonstrate how we can achieve mode multiplexing in a straightforward and simple way. We fabricate the on-chip mode multiplexers on silicon platform which allow highly-confined devices. Due to the large index contrast of silicon and silicon dioxide, it allows a more efficient phase matching between specific modes and in turn reduces intermode crosstalk. We demonstrate a mode- and wavelength-division multiplexing link by passing the data in different modes and wavelength channels. In this work we increase the aggregate data bandwidth by two times but we can definitely further increase the bandwidth by using more higher order modes.

In chapter seven we discuss about a possible future work that is to integrate all different components on the same chip, namely microring modulators, mode multiplexers, and germanium photodetectors. This way we can truly demonstrate an on-chip mode- and wavelength-division multiplexing.

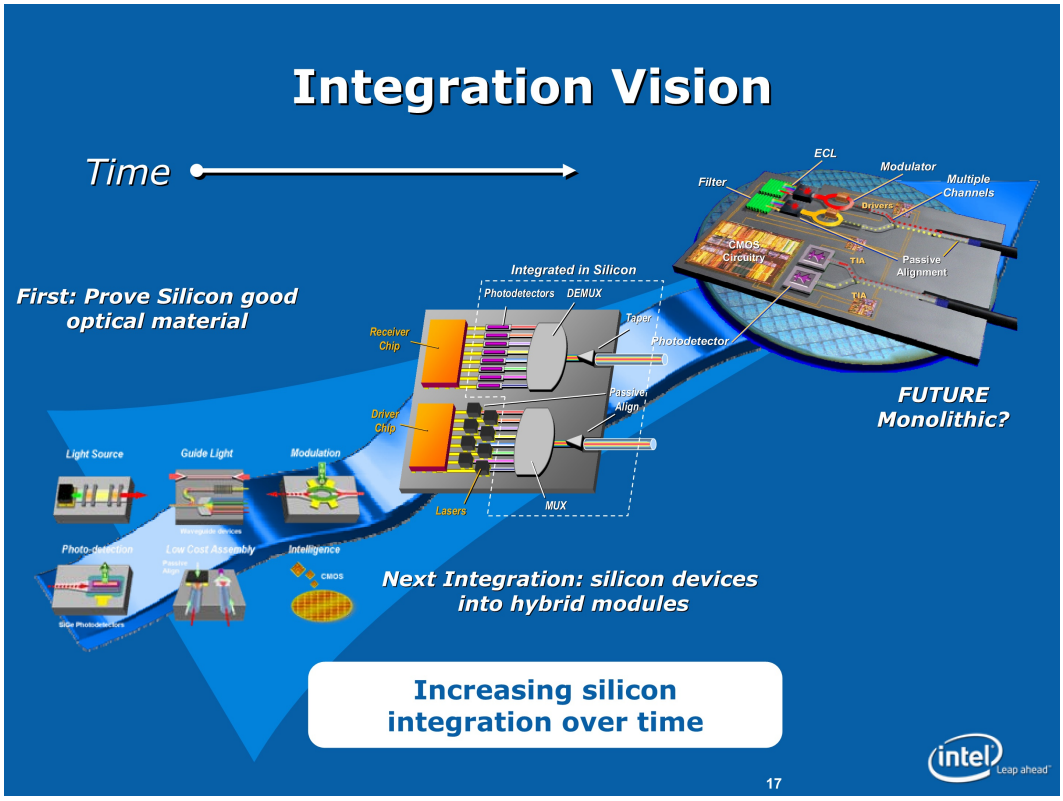

Figure 1.3: Intel's roadmap on silicon optical interconnects integration. Taken from the presentation by Intel [2].

CHAPTER 2

LOW-LOSS ETCHLESS SILICON WAVEGUIDES

2.1 Silicon is an excellent material for waveguiding

Since silicon is the main material used in the complementary metal-oxide-semiconductor (CMOS), it is logical to look into using silicon as the guiding material in optical interconnects. Silicon, having a band gap energy of 1.12 eV at 300 K, is transparent to infrared light with wavelengths above about 1.1 μm. Moreover, silicon has a high refractive index of about 3.5. If silicon dioxide, refractive index of about 1.5, is used as the cladding, the index contrast between the guiding core and cladding is large. This allows the light to be tightly confined in the silicon optical waveguides which can have dimensions as small as a few hundred nanometers. This is substantially less than the wavelength of the light itself (λ = 1.55 μm). This also means that we can pack thousands of silicon optical devices in a single wafer. One other important property of silicon is that it has a large thermo-optical coefficient (1.8×10^{-4}/K). The refractive index of the silicon can be tuned by changing the temperature of the silicon (i.e. heat up the silicon). This is important for tuning a silicon optical device. Due to these many suitable properties of silicon, it is essentially the one material for on-chip optical interconnects.

2.2 Background of traditional fabricated silicon waveguides

Silicon photonics has been studied extensively for on-chip optical interconnects during the past decade as optical interconnects offer a larger bandwidth and lower power consumption in microelectronic chips [11–14]. To realize the goal of optical interconnects in silicon chips, storing or slowing down of optical signals is essential during the routing of the signals. Several on-chip optical buffers based on silicon ring resonators have been demonstrated [15–17]. However, the major challenge faced by these silicon-based optical buffers is the need for low-loss silicon waveguides so that the light can be delayed for a long period of time without signal attenuation.

There are two types of silicon waveguides commonly used by the silicon photonic community, namely rib waveguides and strip waveguides. The silicon waveguides are usually fabricated on a 250 nm silicon-on-insulator wafer with 3 µm of buried oxide using CMOS fabrication processes. The fabrication process flow details are illustrated in Figure 2.1. First the waveguides are patterned using e-beam lithography and etched using chlorine-based etching. After stripping the resist, the etched photonic structures are clad with at least 1 µm of plasma enhanced chemical vapor deposition silicon oxide to confine the optical mode. Rib waveguides with widths of 1–8 µm have exhibited losses down to 0.1 dB/cm but their minimum bending radius is limited to hundreds of micrometers [10,18–25]. To obtain more compact silicon ring resonators, strip waveguides with dimensions approximately 500 nm wide by 250 nm thick are employed [15–17,26–30]. These strip waveguides have demonstrated intrinsic quality factors up to 400,000 in 10 µm-radius ring resonators with a ring loss not lower than 1.8 dB/cm at λ = 1.53 µm.

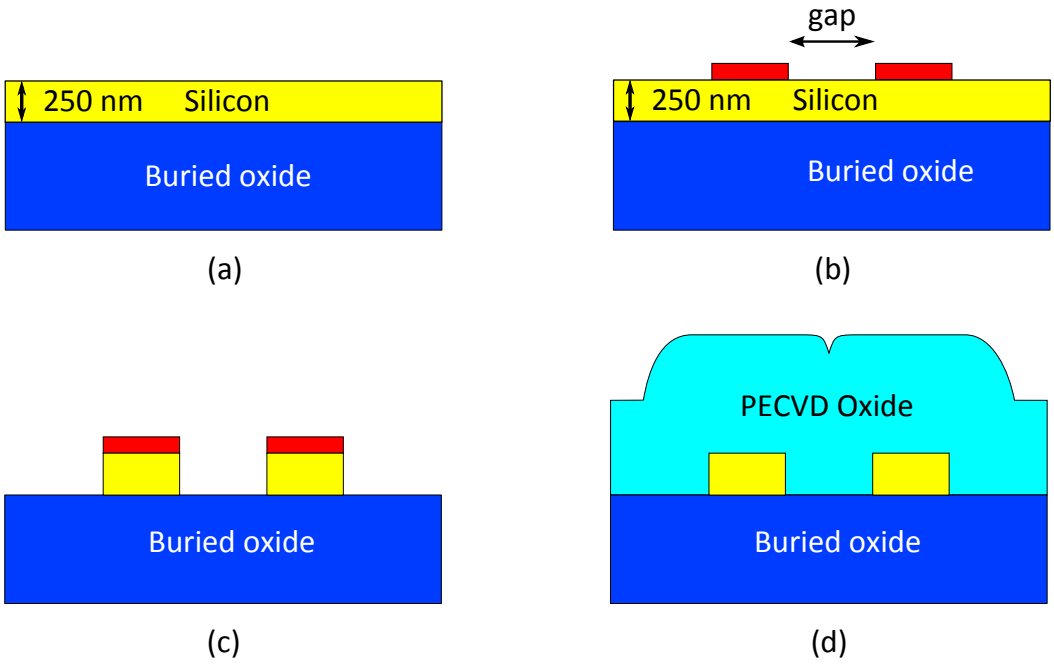

Figure 2.1: Etched silicon waveguide fabrication process flow. (a) Use 250 nm silicon-on-insulator (SOI) as the device layer. (b) Patterning of the waveguides using ma-N 2403 resist, leaving a coupling gap between the ring resonator and bus waveguide. (c) Etching of the silicon layer. (d) Deposition of at least 1.0 µm PECVD silicon dioxide to confine the optical mode.

Losses in silicon waveguides originate largely from the damage of the silicon surfaces by the dry etching processes [31]. The reactive ion etching (RIE) induces surface modifications and results in both the increased scattering losses at the sidewalls due to silicon waveguide roughness (see Figure 2.2) and the increased absorption sites at Si/SiO2 interface due to surface residues and lattice damage [32–34]. The question is whether there is a way where we can reduce these losses of silicon waveguides.

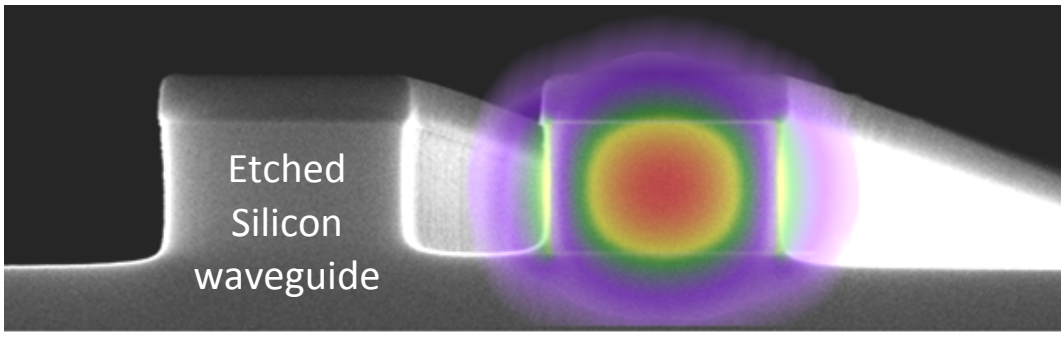

Figure 2.2: Scanning electron microscope picture of etched silicon waveguides with simulation of the interaction between the optical waveguide mode and the sidewall of the waveguide.

2.3 Proposed etchless silicon waveguide fabrication to reduce the scattering and absorption loss

In order to minimize the scattering and absorption loss in etched silicon waveguides, we proposed an etchless silicon waveguide fabrication process based on selective thermal oxidation of silicon [35]. This etchless silicon waveguide fabrication minimizes the waveguide losses resulting from the dry etching by not exposing the silicon surface to any plasma etching throughout the fabrication process. The etchless silicon waveguides possess the advantages of both the low loss of rib waveguides and the small bending radius of strip waveguides.

The etchless silicon waveguides are fabricated from a silicon-on-insulator (SOI) wafer with an initial silicon layer of 500 nm and a buried oxide layer (BOX) of 3 µm. First we grow a thermal oxide layer of 785 nm on the 500 nm SOI which consumes approximately 360 nm of silicon (see Figure 2.3(a)). We then pattern the silicon waveguides with electron beam (e-beam) lithography using ma-N 2405 resist (see Figure 2.3(b)). Next we etch the patterned thermally grown oxide layer with a RIE tool using fluorine chemistry, leaving be-

hind a thin 50 nm oxide slab throughout the whole wafer (see Figure 2.3(c)). This thin oxide slab protects the silicon surface underneath from the ion bombardment and chemical reactions that occur during the plasma etching. After stripping the e-beam resist, we use wet thermal oxidation to selectively oxidize the silicon (see Figure 2.3(d)) and define the silicon waveguides with a thin silicon slab (see Figure 2.3(e)). Lastly, the waveguides are clad with 300 nm of high temperature oxide (HTO) to give a highly conformal deposition and 1.8 µm of plasma enhanced chemical vapor deposition (PECVD) silicon dioxide to confine the optical mode completely (see Figure 2.3(f)).

Using this etchless silicon fabrication method, we demonstrate low loss silicon waveguides fabricated without any silicon etching. We define the waveguides by selective oxidation which produces ultra-smooth sidewalls with roughness of 0.3 nm. The waveguides have a propagation loss of 0.3 dB/cm at 1.55 µm. The waveguide geometry enables low bending loss of approximately 0.007 dB/bend for a 90 degree bend with a 50 µm bending radius [35]. These results are promising for devices where ultra-low loss property is crucial.

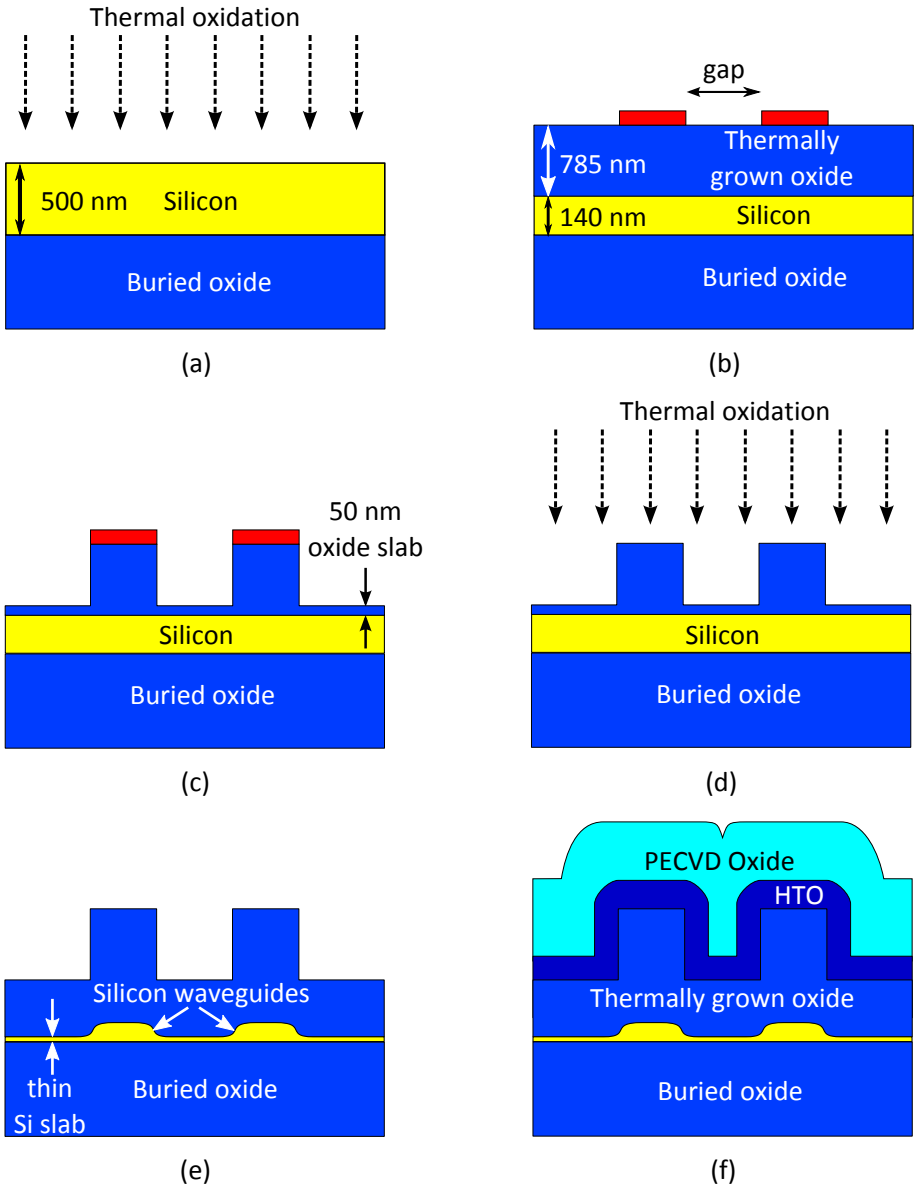

Figure 2.3: Etchless silicon photonic ring resonator fabrication process flow. (a) Thermal oxidation of a 500 nm silicon-on-insulator (SOI) to leave behind 140 nm thick silicon layer with 785 nm thick thermally grown oxide on top. (b) Patterning of the waveguides using ma-N 2405 resist, leaving a coupling gap between the ring resonator and bus waveguide. (c) Etching of the thermally grown oxide, leaving behind a thin 50 nm oxide slab. (d) Selective wet thermal oxidation of the silicon. (e) Structural profile of the oxidized silicon waveguides. (f) Deposition of 300 nm HTO and 1.8 µm PECVD silicon dioxide.

CHAPTER 3

HIGH-QUALITY FACTOR ETCHLESS SILICON MICRORING RESONATORS

3.1 Microring resonators

The main building block of silicon photonics is silicon waveguides. The second basic optical structure used in this dissertation is the microring resonator. The resonator is a circular waveguide which is accessed via a bus waveguide (see Figure 3.1). The resonator is a traveling wave cavity where the optical field circulates in the resonator. When the light in the microring is on-resonance, the field trapped inside the cavity is enhanced due to the numerous round trips made inside the microring.

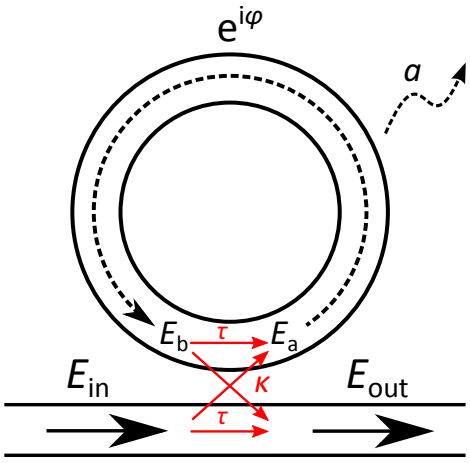

Figure 3.1: An illustration of a waveguide coupled microring resonator. The diagram shows the coupling, κ, and transmission, τ, coefficients for the input and output fields of the device as well as the round-trip loss factor, a.

We can formulate the field inside the microring as follows:

$$E_{out} = \tau E_{in} + i\kappa E_b \tag{3.1}$$

$$E_a = i\kappa E_{in} + \tau E_b \tag{3.2}$$

$$E_b = ae^{i\varphi} E_a \tag{3.3}$$

where κ, and τ are the coupling and transmission coefficients for the input and output fields of the device. For a lossless coupling,

$$\kappa^2 + \tau^2 = 1 \tag{3.4}$$

φ is the total optical phase accumulated by a field propagated inside the microring resonator,

$$\varphi(\lambda) = \beta(\lambda) L_{ring} = \frac{2\pi}{\lambda} n_{eff}(\lambda) L_{ring} \tag{3.5}$$

a is the round-trip loss factor which can be expressed as

$$a = e^{-\frac{\alpha}{2} L_{ring}} \tag{3.6}$$

where α is the field propagation loss in m^{-1}.

Substitute Equation 3.3 into Equation 3.2 gives

$$E_a = \frac{i\kappa E_{in}}{1 - a\tau e^{i\varphi}} \tag{3.7}$$

By substituting Equation 3.3 and Equation 3.7 into Equation 3.1, we can get the output field normalized to the input field.

$$\frac{E_{out}}{E_{in}} = \left(\frac{\tau - ae^{i\varphi}}{1 - a\tau e^{i\varphi}} \right) \tag{3.8}$$

The output amplitude of the microring can be normalized to the input amplitude as follows:

$$\frac{P_{out}}{P_{in}}(\lambda) = \left| \frac{E_{out}}{E_{in}} \right|^2 = \left(\frac{\tau^2 + a^2 - 2a\tau \cos\varphi}{1 + a^2\tau^2 - 2a\tau \cos\varphi} \right) \tag{3.9}$$

We can also define the circulating power inside the microring cavity as

$$\frac{P_{ring}}{P_{in}}(\lambda) = \left|\frac{E_b}{E_{in}}\right|^2 = \frac{a^2\kappa^2}{1 + a^2\tau^2 - 2a\tau\cos\varphi} \tag{3.10}$$

From Equation 3.5 and 3.9, the resonance condition is met when φ is an integer multiple of 2π:

$$m(\lambda_0)\lambda_0 = n_{\text{eff}}(\lambda_0)L_{\text{ring}} \tag{3.11}$$

where m is an integer resonanct mode number and λ_0 is the resonance wavelength.

The on-resonance transmitted power can be simplified as:

$$\frac{P_{\text{out}}}{P_{\text{in}}}(\lambda_0) = \frac{(a-\tau)^2}{(1-a\tau)^2} \tag{3.12}$$

with the transmission coefficient, τ, equivalent to the round-trip loss, a, we can have complete extinction of the input field, also known as critical coupling. At critical coupling, the microring has the maximum circulating power:

$$\max\left|\frac{P_{\text{ring}}}{P_{\text{in}}}(\lambda_0)\right| = \frac{a^2}{1-a^2} \tag{3.13}$$

The cavity energy in the microring is maximized when the resonator losses, a, is negligible. Therefore, when the propagation loss of the waveguides is reduced significantly as discussed in the previous Chapter 2, the cavitiy energy can be maximized.

Figure 3.2 illustrates a simulated transmission spectrum of a critically-coupled silicon microring resonator with a waveguide dimentsion of 450 nm wide x 250 nm tall and a radius of 20 µm. The transmission coefficient is set at 0.88 and the round-trip loss is also set at the same value.

There is one important parameter of resonator, that is, the quality factor (Q-factor). The Q-factor of a resonator is a measure of the strength of the damping

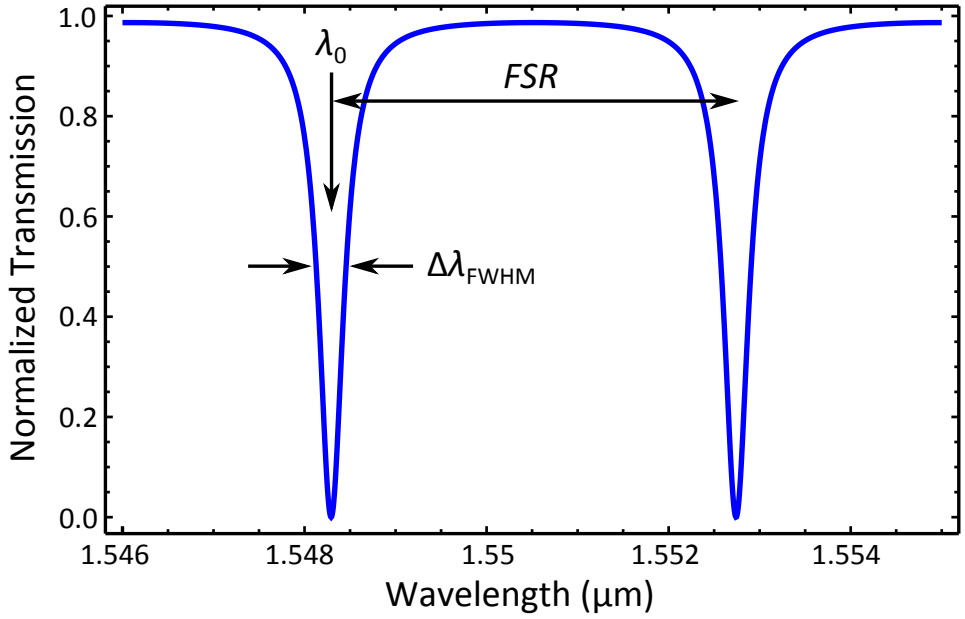

Figure 3.2: A simulated transmission spectrum of a critically-coupled silicon microring resonator with a waveguide dimension of 450 nm wide × 250 nm tall and a radius of 20 μm.

of its oscillations. It can be defined as the ratio of the resonance frequency ω_0 (or resonance wavelength λ_0) and the full width at half-maximum (FWHM) band-width $\Delta\omega_{\mathrm{FWHM}}$ (or $\Delta\lambda_{\mathrm{FWHM}}$).

$$Q = \frac{\omega_0}{\Delta\omega_{\mathrm{FWHM}}} = \frac{\lambda_0}{\Delta\lambda_{\mathrm{FWHM}}} \tag{3.14}$$

In this dissertation, we utilize a property of the microring resonator for the wavelength-division multiplexing, that is free spectral range (*FSR*) which is the frequency spacing of its axial resonator modes.

$$\beta_{\mathrm{m}} L = 2m\pi \tag{3.15}$$

$$\beta_{\mathrm{m+1}} - \beta_{\mathrm{m}} = \frac{2\pi}{L_{\mathrm{ring}}} = \frac{\delta\beta}{\delta\lambda}\Delta\lambda \tag{3.16}$$

$$\Delta\lambda = \frac{2\pi}{L_{\mathrm{ring}}}\left(\frac{\delta\beta}{\delta\lambda}\right)^{-1} \tag{3.17}$$

$$FSR = \left| \frac{2\pi}{L_{\text{ring}}} \left(-\frac{\lambda^2}{2\pi n_{\text{g}}} \right) \right| = \frac{\lambda^2}{n_{\text{g}} L_{\text{ring}}} \tag{3.18}$$

where the group index $n_{\text{g}} = n_{\text{eff}} - \lambda \frac{dn_{\text{eff}}}{d\lambda}$.

We summarize the above-described theoretical discussions of microring resonator. The microring possesses a transmission spectrum where there is an extinction of the input field when the resonance condition is met. This resonance linewidth depends on the Q-factor of the resonator. We can design the *FSR* of the microring to align with the WDM channels for (de)multiplexing purpose in the latter Chapter 5.

3.2 Etchless silicon photonic microring resonators

Here we demonstrate a special type of silicon ring resonators which exhibit lower propagation loss than the strip waveguides and possess smaller bending radius than the rib waveguides. Based on the etchless silicon fabrication discussed in Section 2.3, we design and fabricate high-Q etchless silicon photonic ring resonators [36]. We achieve a high intrinsic quality factor of 510,000 in 50 μm-radius ring resonators, corresponding to a ring loss of 0.8 dB/cm. We also design etchless silicon inverse nanotapers to enable efficient coupling from the lensed fiber into the chip. The device shows a low coupling loss of approximately 1.5 dB per facet, corresponding to 71% fiber-waveguide coupling efficiency.

3.2.1 Designing etchless silicon photonic microring resonators

The final structural geometry of an etchless silicon photonic device is dependent on the thickness of the thermally grown oxide layer above the silicon, i.e. the thermal oxidation rate of the silicon at the regions with thin oxide slab is faster than that at the regions with thicker oxide layer. The final structural profile of an etchless silicon waveguide has a slowly varying sidewall which is different from the vertical sidewall of an etched silicon waveguide. In designing 50 μm-radius etchless silicon photonic ring resonators (see Figure 3.3(a)), we use a commercial software Silvaco Athena [37] to simulate the structural profile of the etchless silicon waveguides defined by the selective thermal oxidation process (see Figure 3.3(b)). Next we import the simulated profile into Comsol (a finite element modeling software) [38] to compute the modal properties of the etchless silicon waveguides (see Figure 3.3(c)). To enable critical coupling at λ = 1.55 μm, the dimensions of the etchless silicon waveguides following the selective thermal oxidation process are designed to be 800 nm wide by 60 nm tall with a coupling gap of 930 nm [39].

3.2.2 Fabricating etchless silicon photonic microring resonators

The waveguides are fabricated using 800 nm wide by 785 nm thick etched oxide mask and a coupling gap of 930 nm with a wet thermal oxidation time of 20 minutes (see Figure 3.3(d)). The scanning electron microscope (SEM) picture in (see Figure 3.3(d)) shows the cross-sectional profile of the coupling region and the structural profile of the fabricated device matches with the simulations accurately. This fabrication technique, which avoids any etching of the silicon layer,

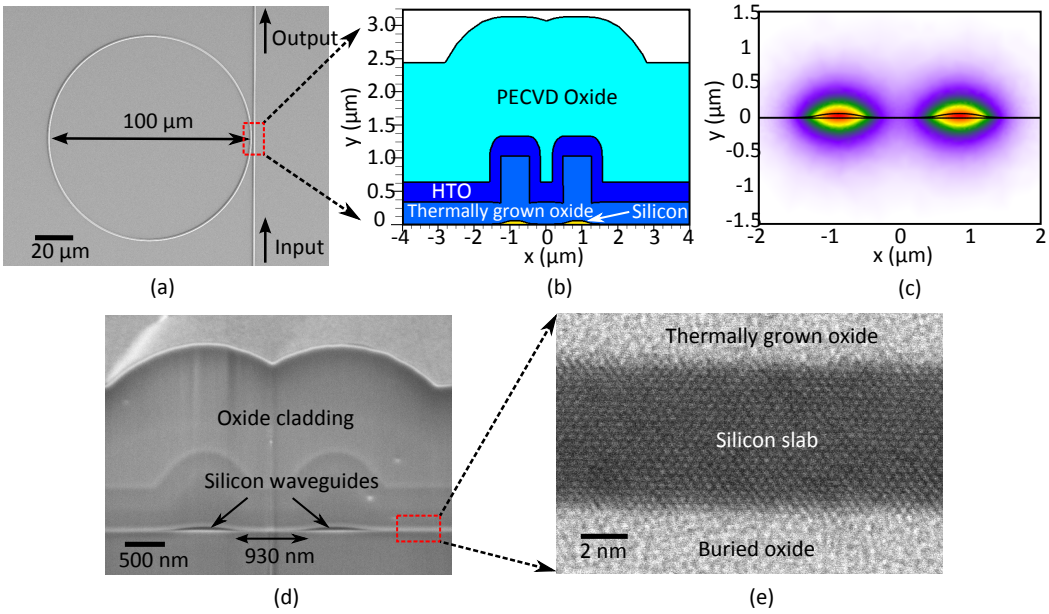

Figure 3.3: (a) SEM picture of the fabricated 50 µm-radius etchless silicon photonic ring resonator. (b) Simulated structural profiles of the etchless silicon ring resonator with coupling gap = 930 nm. (c) Symmetric mode of the bus waveguide and the ring resonator. (d) Cross-sectional SEM picture of the coupling region. (e) Transmission electron microscope (TEM) picture of the thin oxidized silicon slab.

results in an ultra-smooth top Si/SiO2 interface comparable to the interface between the silicon and the buried oxide, as shown in the transmission electron microscope (TEM) picture of the thin oxidized silicon slab (see Figure 3.3(e)).

The 800 nm wide etchless silicon waveguide forming the ring resonator supports only one mode, i.e. the fundamental TE mode (see Figure 3.4(a)). The advantage of supporting only the fundamental TE mode is that the polarization mode conversion is minimized, thus reducing the crosstalk in polarization. The 800 nm waveguide has an effective index of 1.6 at λ = 1.55 µm and a mode size of 1 µm wide by 0.52 µm high. On the other hand, a lensed fiber has an effective index of 1.468 and a mode field diameter of 2.5 µm. The coupling of

light directly from the lensed fiber into the 800 nm waveguide results in a measured coupling loss of more than 10 dB. This coupling loss is high due to both the refractive index mismatch and mode mismatch between the lensed fiber and the etchless silicon waveguide. To minimize the coupling loss, a 220 nm wide etchless silicon inverse nanotaper with a taper length of 100 µm is integrated at both the input waveguide and output waveguide [40]. The designed inverse nanotaper has an effective index of 1.453 and a mode size of 5 µm wide by 2 µm high (see Figure 3.4(b)). Due to this improved match in refractive index and mode size, the coupling loss from the lensed fiber into the inverse nanotaper is reduced to approximately 1.5 dB. This measured coupling loss is one of the lowest demonstrated in silicon photonic devices.

3.2.3 Results and discussions

We demonstrate a high-Q 50 µm-radius etchless silicon ring resonator with an ultra-low total chip insertion loss. We couple a tunable laser light source from a lensed fiber into the etchless silicon inverse nanotaper at the input of the chip through a polarization controller. The light from the output of the chip is then collimated through a lens and collected at a photodetector to measure the total chip insertion loss of TE-polarized light. We observe a clean transmission spectrum, i.e. the Fabry-Perot modulation between the two end facets of the chip is negligible due to the well-designed etchless silicon inverse nanotaper (see Figure 3.5(a)). We measure an ultra-low total chip insertion loss of 2.5 dB from the input lensed fiber to the photodetector at the output. This total chip insertion loss includes the propagation loss of the 1 cm long etchless silicon waveguide and the coupling loss at the chip facets. With a Lorentz fit to the resonance at

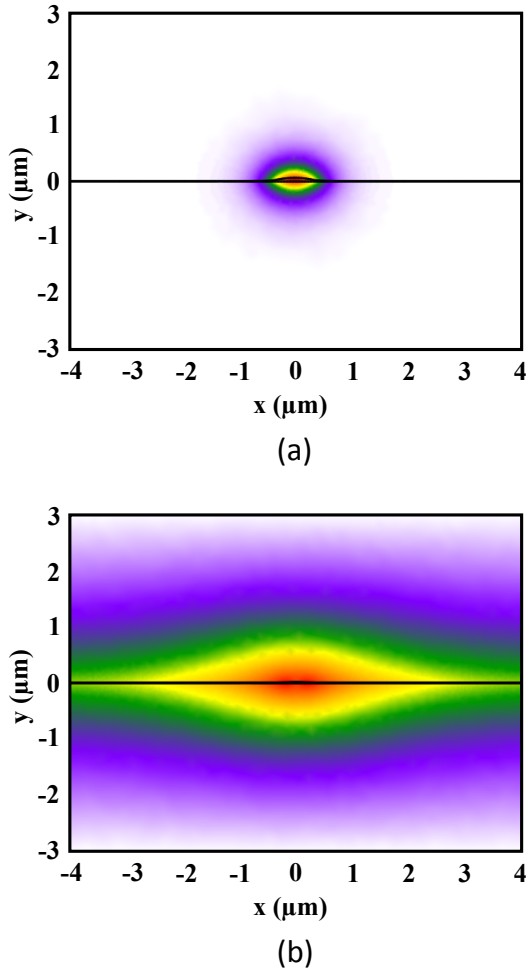

Figure 3.4: Transverse electric (TE) mode profile (Ex-component) of (a) Etchless silicon waveguide. (b) Etchless silicon inverse nanotaper.

λ_0 = 1531.416 nm, we measure the linewidth of the spectrum to be 5.5 pm, giving a loaded quality factor of $Q_{loaded} \approx 280,000$ (see Figure 3.5(b)). The ring is slightly under-coupled at this resonant wavelength. The intrinsic quality factor Q_{int} of the ring can be written as [41]:

$$Q_{\text{int}} = \frac{2Q_{\text{loaded}}}{1 + \sqrt{T_0}}, \tag{3.19}$$

where T_0 is the fraction of transmitted optical power measured by the photodetector at the resonant wavelength λ_0. Using Equation 3.19, with the measured

$T_0 = 0.007$, we calculate the intrinsic quality factor $Q_{\text{int}} = 510{,}000$.

The total propagation loss per unit length in the ring α_{ring} can be written as [42]:

$$\alpha_{\text{ring}} = \frac{2\pi n_g}{Q_{\text{int}} \lambda_0} = \frac{\lambda_0}{Q_{\text{int}} \times FSR \times R_{\text{ring}}}, \tag{3.20}$$

where n_g is the group index, FSR is the free spectral range, and R_{ring} is the radius of the ring resonator. Using Equation 3.20, with the measured $FSR = 3.25$ nm and $R_{\text{ring}} = 50$ µm, we calculate the ring loss $\alpha_{\text{ring}} = 0.8$ dB/cm. We estimate the coupling loss between the lensed fiber and the etchless silicon inverse nanotaper to be approximately 1.5 dB, corresponding to 71% fiber-waveguide coupling efficiency.

3.2.4 Conclusion

We designed and fabricated high-Q etchless silicon photonic ring resonators using selective thermal oxidation of silicon without the silicon layer being exposed to any plasma etching throughout the fabrication process. We achieved a high intrinsic quality factor of 510,000 in 50 µm-radius ring resonators, corresponding to a ring loss of 0.8 dB/cm. We also realized an ultra-low total chip insertion loss of 2.5 dB with a fiber-waveguide coupling loss of approximately 1.5 dB by employing etchless silicon inverse nanotapers at both the input and output of the device chip. The low loss etchless silicon photonic ring resonators have promising applications in silicon ring resonators-based optical buffers.

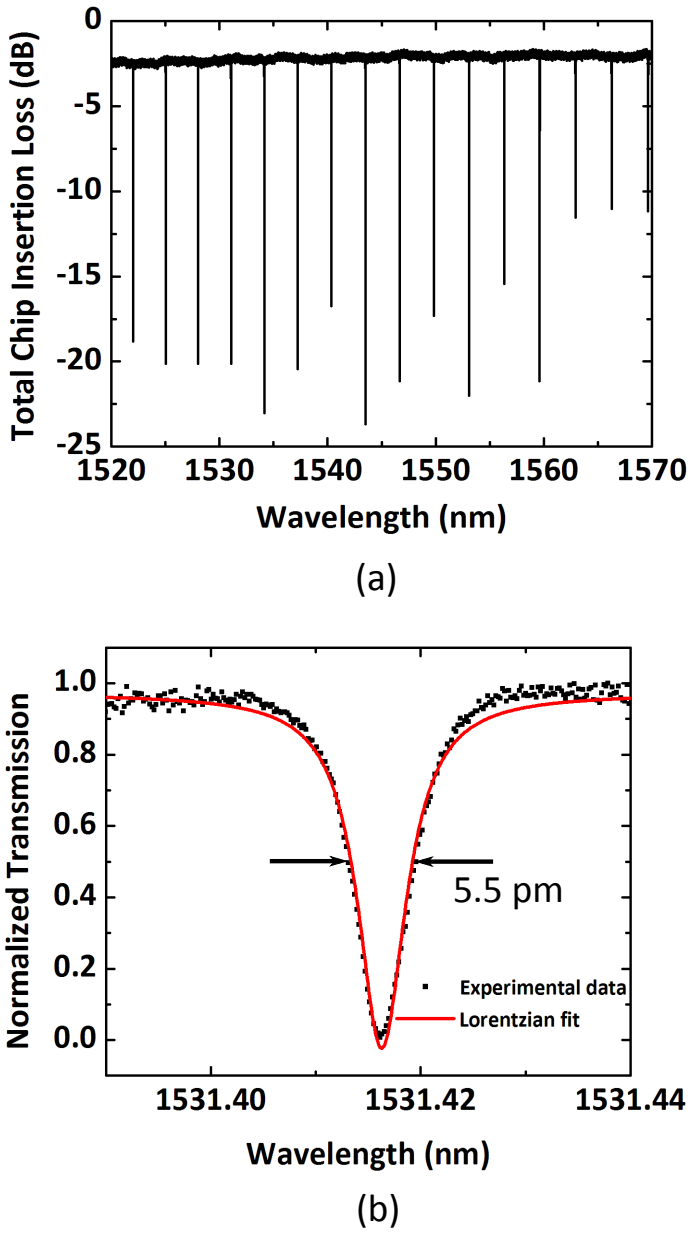

Figure 3.5: (a) Through-port transmission spectrum of the ring resonator in transverse electric (TE) polarization. (b) Normalized transmission spectrum at λ_0 = 1531.416 nm.

CHAPTER 4

NONLINEAR EFFECTS IN MICRORING RESONATORS

4.1 Introduction

Silicon microring resonators have revolutionized the field of silicon photonics for on-chip optical interconnects over the past decade. Optical interconnect networks utilizing silicon microring-based devices present a solution to the electrical interconnect bottleneck by offering a larger bandwidth, lower power consumption and smaller device footprint in microelectronic chips [11, 13, 14]. However, silicon microresonators have one main drawback, that is, the resonant wavelength shifts with input optical power. At high powers, the stored light in a silicon microresonator is absorbed via two photon absorption (TPA) and generates free carriers (see Figure 4.1). This results in a blue shift of the resonance due to free carrier dispersion (FCD). In addition, the generated carriers lead to free carrier absorption (FCA). The TPA and FCA nonlinear processes, together with the linear surface absorption at the Si/SiO_2 interface, result in the heating of the resonator and cause a red shift in the resonance. In particular, reactive ion etching of the silicon induces surface and sidewall damage, resulting in the increased absorption sites at Si/SiO_2 interface [31, 34]. Etching also results in increased recombination sites and shorter free carrier lifetime. Due to the dominant thermo-optic (TO) red shift over the FCD blue shift, an effective red shift of the resonance is observable in many etched silicon microresonators, such as microdisk, microring (see Figure 4.2), and photonic crystal resonators [34,41,43,44].

The ability to tailor the microresonator spectral dependence on input power is critical. Several previous works to achieve microresonators with a power-

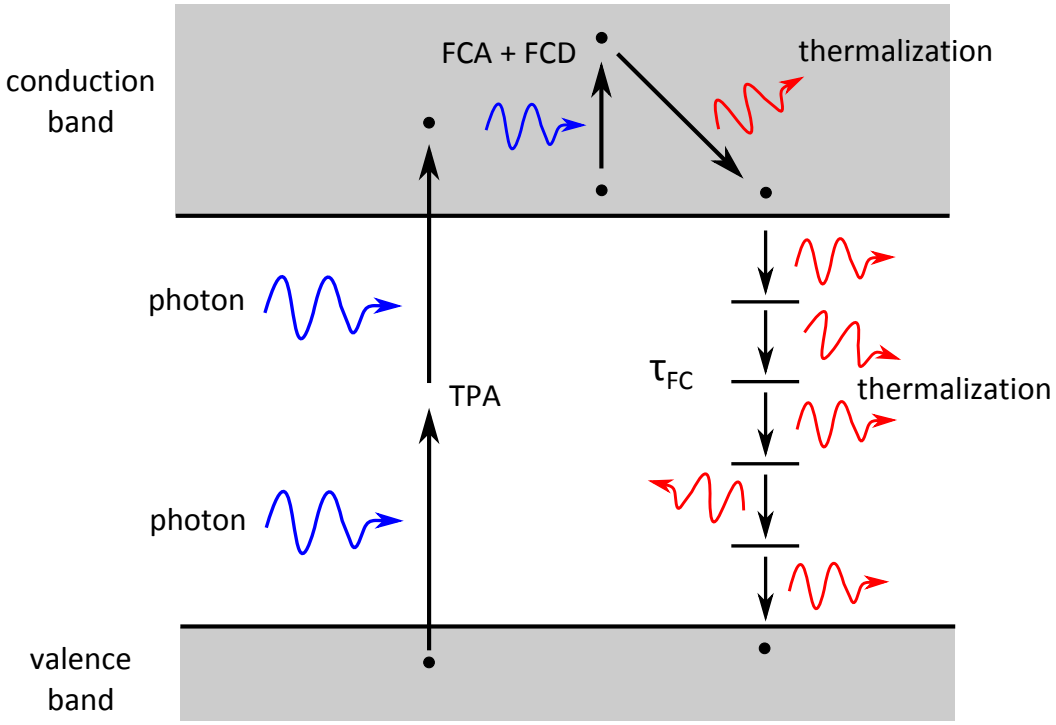

Figure 4.1: Electronic band gap diagram of silicon showing all the absorption and generation mechanisms of photons, phonons, and electrons. The two-photon absorption (TPA) process absorbs photons (which results in TPA loss and degrades the Q) and excites the electrons from the valence band to the conduction band. The phonons takes part in sending the electrons in the conduction band from one state to another state through relaxation process. The generated electrons decrease the refractive index through free carrier dispersion (FCD), and results in a resonance blue shift. The generated carriers also adds free-carrier absorption (FCA) (which degrades the Q). The TPA and FCA nonlinear processes, together with the linear surface absorption at the Si/SiO_2 interface heats the resonator (which results in a resonance red shift).

independent transmission spectra have been pursued. In one approach, polymer with a negative TO coefficient has been used as a cladding material to compensate for the positive TO microcavity [45, 46]. But the use of polymers is not compatible with CMOS processes. Another work has utilized an additional stabilizing laser to compensate the TO effect, ensuring a Lorentzian line-shape

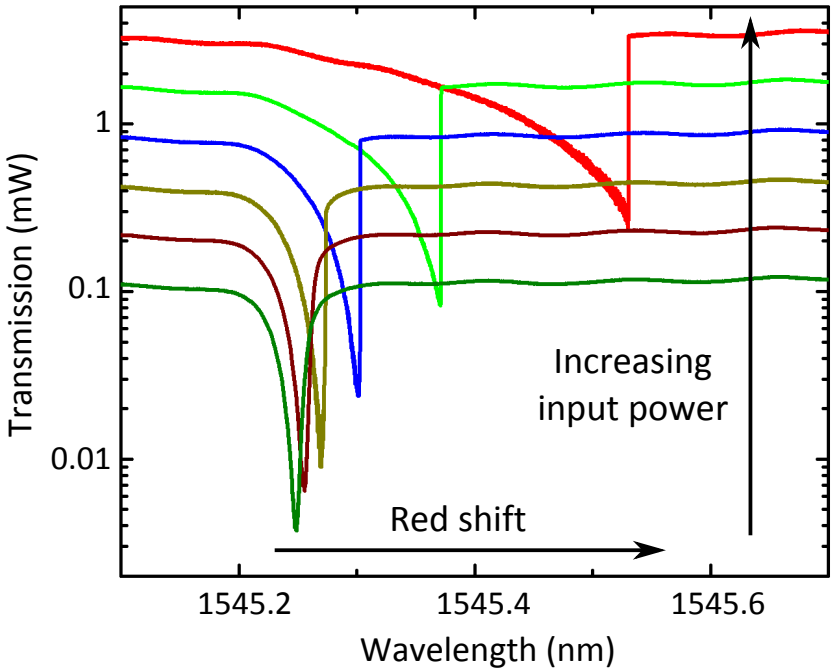

Figure 4.2: Measured transmitted power spectrum of a typical microring resonator showing the net red shift of the resonance with increasing laser input power. The laser is swept from shorter wavelength to longer wavelength.

transmission [47]; this approach is relatively power hungry. Here we demonstrate power insensitive silicon microring resonators using a passive technique by utilizing two counteracting processes, FCD blue shift and TO red shift. It should be noted that this technique reduces the sensitivity dependence of the resonance on laser input power but not on ambient temperature.

4.2 Relationship between the FCD blue shift and the TO red shift of the resonance

In order to control the degree of spectral shift with optical power, we analyze the effective resonance shift $\Delta\lambda$ due to the counteracting effects of FCD and TO processes in the silicon microresonator (neglecting the minor contribution of TO in the cladding SiO_2) [41,48]:

$$\Delta\lambda \approx \frac{\lambda_0}{n_g}(\Delta n_{FC} + \Delta n_T), \tag{4.1}$$

where λ_0 is the resonant wavelength, n_g is the group index of the microresonator, and Δn_{FC} and Δn_T are the refractive index change of Si due to FCD and TO effect respectively. The index change due to FCD is expressed as $\Delta n_{FC} = -8.8 \times 10^{-22}\Delta N - 8.5 \times 10^{-18}(\Delta P)^{0.8}$, where ΔN and ΔP are the density of generated electrons and holes per cubic centimeter and $\Delta N = \Delta P = \left(\frac{\Gamma_{FCD}c^2\beta}{2\hbar\omega_0 n_g^2 V_{FCD}^2}\right)\tau_{FC}U^2$. Γ_{FCD} is the effective confinement factor corresponding to FCD, c is the speed of light in free-space, $\beta = 8.4\times10^{-12}$ m·W^{-1} is the TPA coefficient in silicon, $\hbar$ is the reduced Planck constant, ω_0 is the resonant frequency of the resonator, n_g is the group index of the resonator, V_{FCD} is the effective nonlinear mode volume, τ_{FC} is the free carrier lifetime and U is the intra-cavity stored energy. The index shift due to TO can be expressed as $\Delta n_T = \Gamma_{th}\left(\frac{dn_{Si}}{dT}\right)R_{th}\gamma_{abs}U$, where Γ_{th} is the effective confinement factor corresponding to the TO effect, $\frac{dn_{Si}}{dT} = 1.86 \times10^{-4}$ K^{-1} is the TO coefficient of silicon, R_{th} is the cavity thermal resistance, and γ_{abs} is the total cavity optical absorption rate (sum of linear absorption, TPA and FCA).

4.3 Nonlinear measurements of the fabricated etchless silicon microring resonator

Equation 4.1 sets the guideline in designing the physical and geometrical properties of the resonator to balance the FCD blue shift and the TO red shift of the resonance. We can increase the FCD blue shift by designing a photonic structure with long free carrier lifetime (τ_{FC}) to compensate the dominant TO red shift.

We fabricate a 50 µm-radius silicon microring resonator through selective oxidation using the etchless silicon fabrication technique [36]. The dimensions of the microring are 800 nm wide by 60 nm high with a 6 nm thin slab and 1 µm coupling gap [49]. The silicon waveguide is not exposed to any etching plasma throughout the fabrication process, preventing damage from the ion bombardment and chemical reactions. This etchless technique results in an ultra-smooth Si/SiO_2 interface and reduces absorption and recombination sites. We expect that the ultra-smooth interface reduces the electron-hole recombination rate and thereby increases the free carrier lifetime which is needed to compensate the dominant TO red shift.

We measure the free carrier lifetime of the fabricated etchless silicon microring resonator using a pump-probe optical setup (see Figure 4.3(a)). We couple into the microring an Er-fiber pulsed laser with 500 fs pulses, 25 MHz repetition rate and a spectral width of 6 nm at its center wavelength, λ_{pump} = 1543 nm. The pump pulses, with a peak power of 52 W, are absorbed by the silicon microring via TPA and free carriers are generated. This results in a blue shift of the resonance due to FCD. Concurrently, a quasi-TE polarized continuous-wave (CW) weak probe laser is coupled into the microring resonator and tuned to a near-

linear portion of the resonance, $P_{\text{probe}} \approx 3$ μW and $\lambda_{\text{probe}} = 1489.484$ nm (see Figure 4.3(b)). The microring has a loaded quality factor $Q = 350,000$. The exponential growth in Figure 4.3(c) is linearly related to the recombination of free carriers and the experimental carrier lifetime is calculated to be 10 ns by fitting a simple exponential to the data. By avoiding reactive ion etching of the silicon, the effective τ_{FC} of the etchless silicon structure is more than one order of magnitude longer than that of an etched silicon microring [50].

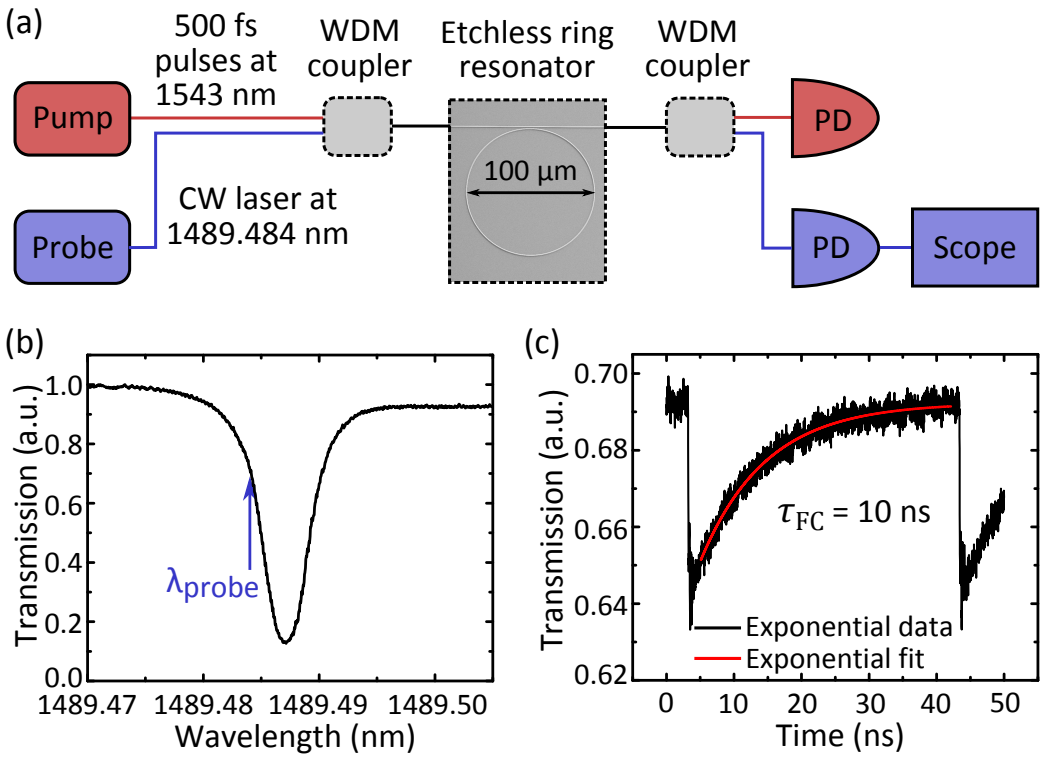

Figure 4.3: (a) Schematic diagram of the pump-probe setup for the measurement of free carrier lifetime. (b) Transmission spectrum of the etchless microring in quasi-TE polarization with $\lambda_{\text{probe}} = 1489.484$ nm. (c) Measurement of carrier lifetime.

Next we measure the microring power-dependent transmission using a CW tunable laser. In Figure 4.4 we show the measured transmission (TE polarization) for several different CW laser power levels. At laser power of 10 μW, the

microring is slightly undercoupled at 1542.162 nm. We observe that the resonance blue shifts with increasing input power, in contrast to the typical red shift in etched silicon microresonators. The effective blue shift is a result of the long free carrier lifetime of 10 ns. The net blue shift is large enough to induce optical bistability for power levels above 42 µW. Also, a reduction in the resonance extinction ratio and the optical quality factor is observed due to the increased nonlinear TPA and FCA losses. In this etchless microring, the FCD overcompensates the TO effect and becomes the dominant process, giving an effective blue shift of the resonance.

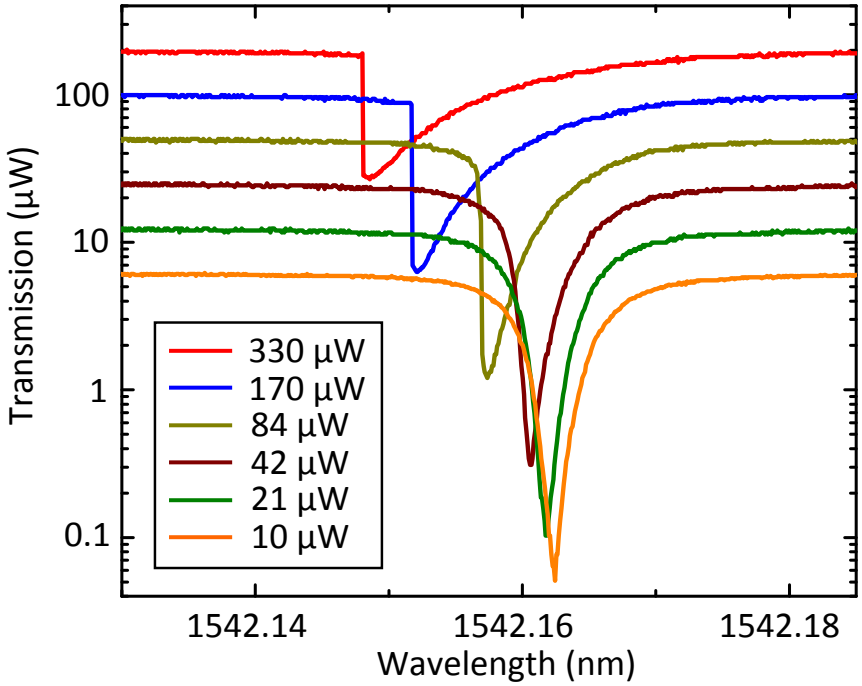

Figure 4.4: Measured transmitted power spectrum of the etchless silicon microring resonator showing the net blue shift of the resonance with increasing laser input power (indicated in the inset). The laser is swept from longer wavelength to shorter wavelength.

4.4 Engineering the nonlinear resonance shift of the etchless silicon microring

To control the resonance shift with input power, we can engineer the thermal properties of the etchless silicon microring. In Figure 4.5(a) we show the calculated resonant wavelength shift map of the etchless microring for a fixed τ_{FC} of 10 ns. To realize a power insensitive device, we etch trenches around the microring, as illustrated in Figure 4.5(b), to increase the thermal resistance of the device ($R_{\mathrm{th}} \approx 3000$ W/K). According to Figure 4.5(a), such a value of R_{th} should result in a device with a very small power sensitivity. The thermal resistance can be controlled by varying the depth of the etched trenches, as shown in Figure 4.5(c) [51]. The trenches are located 5 µm away from the guiding core, which prevents optical losses and degradation of carrier lifetime.

To analyze the effective resonance shift, we show in Figure 4.6 the measured power-dependent wavelength shift of three etchless silicon microrings; each device with a different depth of the etched trenches. Each curve in Figure 4.6 is obtained by extracting the minimum transmission wavelength ($\lambda_0 \approx 1542$ nm) for different power levels of the scanning CW laser, as in Figure 4.4. In the resonator without trenches (R_{th} = 1300 K/W, blue curve in Figure 4.6) there is a net blue shift, which becomes larger than one resonance linewidth at a dropped power around 30 µW. By etching 300 µm deep trenches into the silicon substrate (R_{th} = 3800 K/W, see red curve in Figure 4.6), there is a net red shift for dropped powers larger than 85 µW. This shows that the trenches significantly increase the thermal resistance of the device and the TO effect becomes the dominant process. By etching away only the thin silicon slab (R_{th} = 3000 K/W, see green

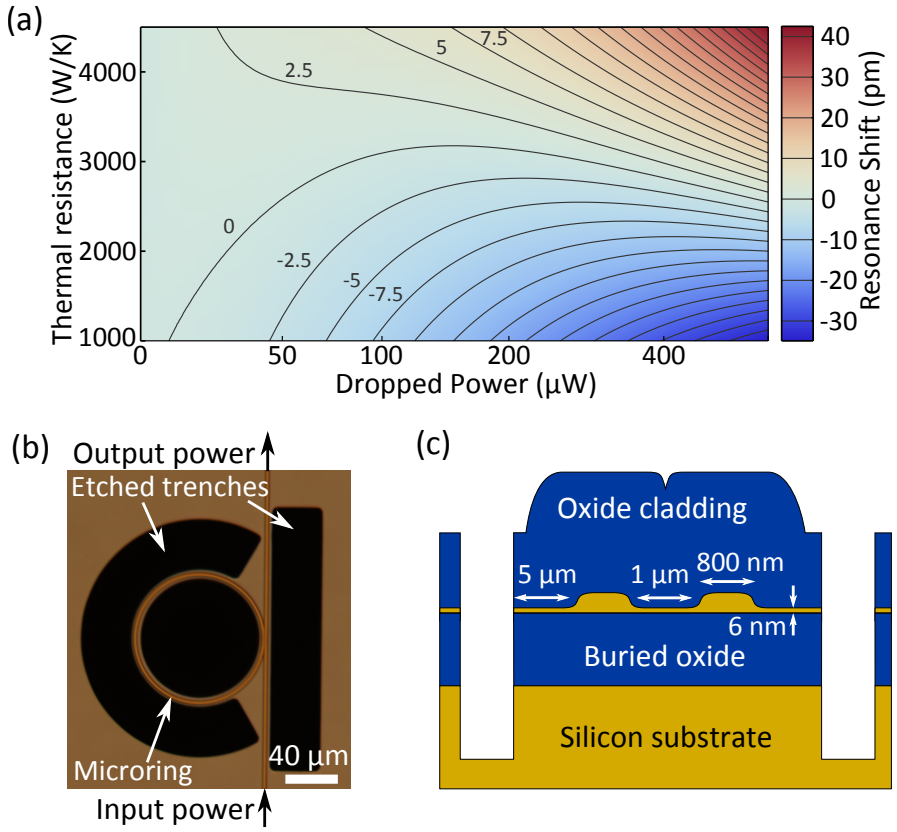

Figure 4.5: (a) Density plot calculating the resonance shift as a function of thermal resistance and dropped power. (b) Optical microscope picture of the fabricated etchless silicon microring resonator with etched trenches. (c) Schematic diagram of the cross section to illustrate the depth of the trenches (not drawn to scale).

curve in Figure 4.6), we obtain a power insensitive etchless silicon microring resonator for dropped power levels up to 335 µW.

4.5 Conclusion

In conclusion, we demonstrate power insensitive silicon microring resonators by utilizing two counteracting processes, free carrier dispersion blue shift and thermo-optic red shift [52]. We use the etchless fabrication process for this

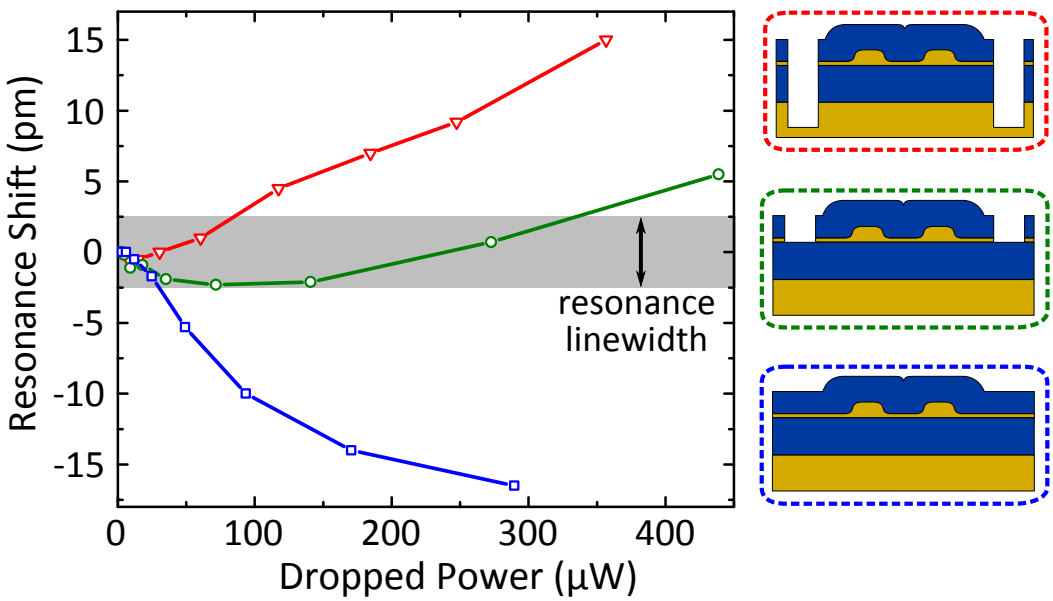

Figure 4.6: Measured resonance shift power dependence (at $\lambda_0 \approx 1542$ nm) of three different etchless silicon microring resonator devices: one without etched trenches (blue curve), one with just the silicon slab etched (green curve), and one with 300 μm deep trenches (red curve). The schematic insets on the right indicates the corresponding device cross-section, the straight lines connecting the experimental data are guides for the eyes.

demonstration however it is not strictly limited to only this fabricaiton technique. The usual etched fabrication method can also demonstrate this phenomenon. In our fabricated etchless silicon microring resonators, the resonant wavelength shifts less than one resonance linewidth for dropped power up to 335 μW, this represents a fivefold improvement in cavity energy handling capability, as compared to a regular etched microring [44]. This compensation technique can also be employed in other resonator-based devices with long carrier lifetime [53].

CHAPTER 5

ON-CHIP WAVELENGTH-DIVISION MULTIPLEXING

5.1 Introduction

Optical interconnect networks utilizing wavelength-division multiplexing (WDM) technology present a solution to the electrical interconnect bottleneck by offering a larger bandwidth and lower power consumption in high-performance microelectronic chips [14, 54]. To realize this goal, several high speed and low power silicon-based devices such as modulators and photodetectors have been reported [5, 6, 55–59].

We propose a multiplexing scheme that can demultiplex densely located WDM channels with low crosstalk in the initial stage and use a less efficient demultiplexing device at the later stage. (see Figure 5.1). In order to interleave densely located WDM channels into less densely channels with high efficiency and low crosstalk, we need to have an interleaver that has a flat passband over the entire C band. This interleaver acts as the demultiplexing stage (DeMux Stage) in Figure 5.1 to split the incoming data signals into two paths: odd signals to the bar port and even signals to the cross port. After the signals are split into two paths, the signals at each port are more sparsely located and the switching mechanism has less stringent requirements which can possess slower roll-off slope without incurring significant crosstalk. We propose to use the simple first-order add-drop microring resonators to switch the desired wavelength channel to a port (see the Switching Stage in Figure 5.1). Only the interleaver in the first demultiplexing step is required to possess rapid roll-off slope to interleave the closely packed channels with minimal channel crosstalk.

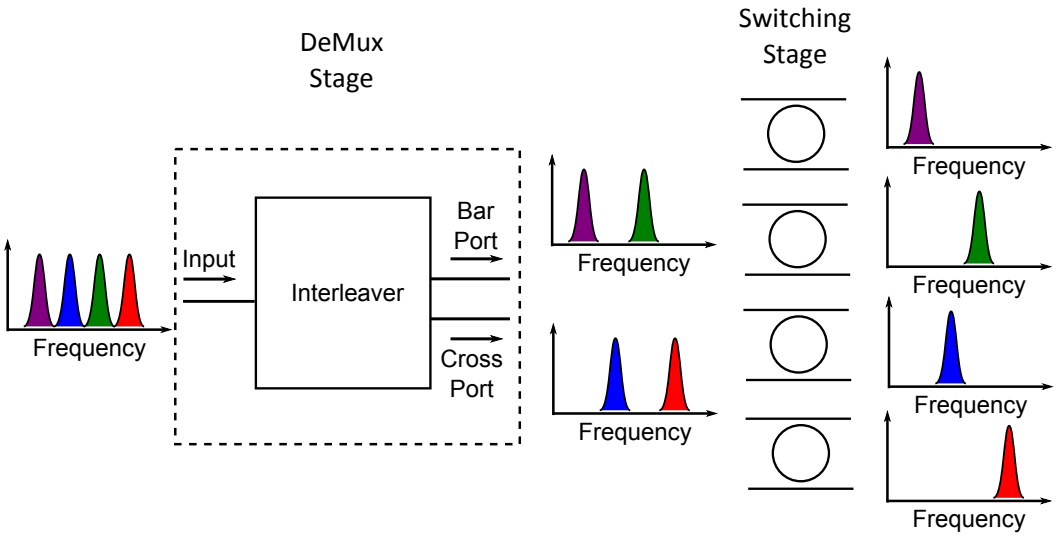

Figure 5.1: WDM demuplexing system proposal using two stages. Interleaver at the DeMux stage to split the densely WDM channels and add-drop microring filters to switch one channel to a desired port.

5.2 WDM microring-based add-drop Demultiplexers

5.2.1 Microring-based add-drop filter

Several different approaches for enabling wavelength channel multiplexing and demultiplexing on silicon have been reported. The approaches include array waveguide grating (AWG) [60], echelle grating [61], MZI-based interleaver [62] and cascaded add-drop microrings [63, 64]. One important requirement of demultiplexers is to have a small footprint to reduce the cost per wafer as well as reduce the power consumption of the demultiplexers. However the multiplexers based on AWG, echelle grating and MZI have a large footprint, therefore they are not ideal for on-chip demultiplexers. In contrast microring resonators-based add-drop filters are compact since silicon waveguides have high index

contrast, enabling small bending radius with low radiation loss. Moreover, silicon has a large thermo-optic coefficient (1.8×10^{-4}/K). This allows the ring resonance to be tuned thermally in the order of 0.1 nm/K with low power consumption.

We implement WDM demultiplexers based on microring add-drop demultiplexers. The microring here is similar to Chapter 3.1; the only difference is that the microring is now coupled to two bus waveguides (see Figure 5.2).

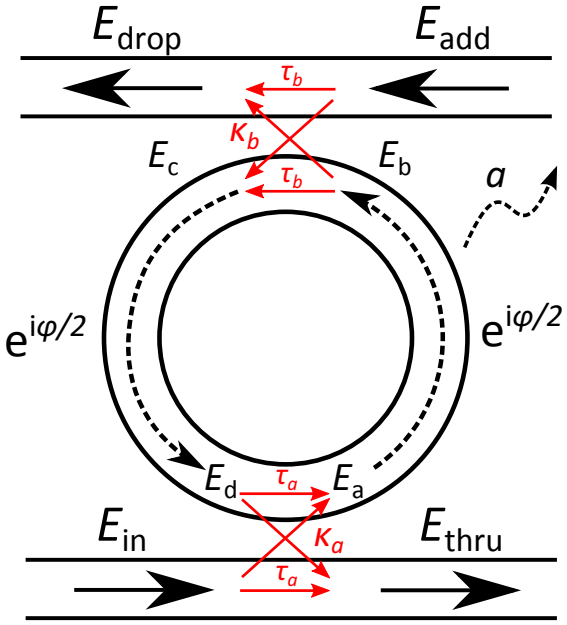

Figure 5.2: An illustration of an add-drop microring filter. The diagram shows the coupling, κ, and transmission, τ, coefficients at both coupling regions as well as the round-trip loss factor, a.

We can formulate the add-drop filter similar to the fundamental equations in Equation 3.1–3.3. We will assume $E_{\text{add}} = 0$.

$$E_{\text{thru}} = \tau_{\text{a}} E_{\text{in}} + i\kappa_{\text{a}} E_{\text{d}} \tag{5.1}$$

$$E_{\text{a}} = \tau_{\text{a}} E_{\text{d}} + i\kappa_{\text{a}} E_{\text{in}} \tag{5.2}$$

$$E_{\text{d}} = \tau_{\text{b}} E_{\text{a}} a e^{i\varphi} \tag{5.3}$$

$$E_{\text{drop}} = i\kappa_{\text{b}} E_{\text{a}} a^{1/2} e^{i\varphi/2} \tag{5.4}$$

From Equation 5.1-5.4, we can derive the functions for throughput power and dropped power.

$$\frac{P_{\text{thru}}}{P_{\text{in}}} = \left|\frac{E_{\text{thru}}}{E_{\text{in}}}\right|^2 = \frac{{\kappa_{\text{a}}}^2 {\kappa_{\text{b}}}^2 a}{1 + {\tau_{\text{a}}}^2 {\tau_{\text{b}}}^2 a^2 - 2\tau_{\text{a}}\tau_{\text{b}} a \cos\varphi} \tag{5.5}$$

$$\frac{P_{\text{drop}}}{P_{\text{in}}} = \left|\frac{E_{\text{drop}}}{E_{\text{in}}}\right|^2 = \frac{{\tau_{\text{a}}}^2 + {\tau_{\text{b}}}^2 a^2 - 2\tau_{\text{a}}\tau_{\text{b}} a \cos\varphi}{1 + {\tau_{\text{a}}}^2 {\tau_{\text{b}}}^2 a^2 - 2\tau_{\text{a}}\tau_{\text{b}} a \cos\varphi} \tag{5.6}$$

Figure 5.3 illustrates a simulated transmission spectrum of a silicon add-drop microring resonator with a waveguide dimentsion of 450 nm wide x 250 nm tall and a radius of 20 μm. The transmission coefficient is set at 0.9 for both bus-ring coupling regions while the microring loss is set at 3 dB/cm. Given that the microring loss is low ($a \approx 1$), the microring can be critically-coupled as long as the bus waveguides are strongly coupled to the microring, $\tau_a \approx \tau_b < a$. At this critically-coupled condition, the drop port can be used to demultiplex different wavelength channel. By changing the microring size, we can change the FSR such that the next neighboring resonance of one microring does not overlap with the resonance of another microring.

5.2.2 WDM demultiplexer design

Here we design a 4-channels microring-based add-drop filters with the following specifications:

1. 5 nm channel spacing
2. 4 nm tuning range for each channel

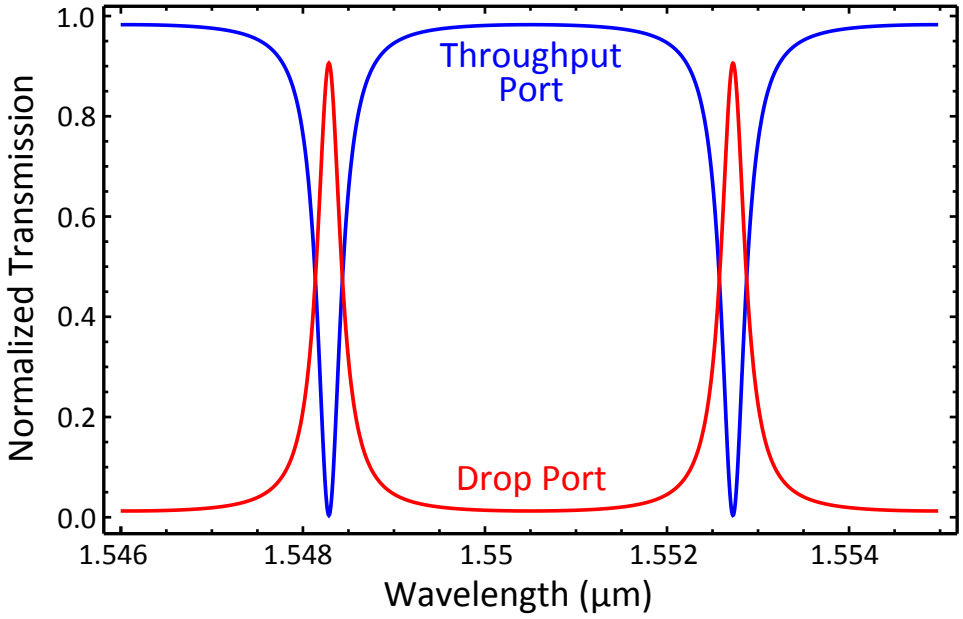

Figure 5.3: A simulated transmission spectrum of a silicon add-drop microring filter with a waveguide dimension of 450 nm wide x 250 nm tall and a radius of 20 μm.

3. 32 mW total power consumption for tuning

To satisfy the requirement of 4 channels with 5 nm spacing, the free spectral range (FSR) of each microring has to be greater than 20 nm. The FSR can be calculated as belows:

$$FSR = \frac{\lambda^2}{n_g L_{ring}}, \tag{5.7}$$

where λ is the free space wavelength, n_g is the group index of the device, and L_{ring} is the circumference of the ring.

To operate the filter centered at $\lambda = 1550\ nm$, since $n_g = 4.4$, according to Equation 5.7 the circumference of the ring L_{ring} has to be approximately 27.3 μm. The microring size is extremely small but it can be made possible with low radiation loss due to high index contrast of silicon and silicon dioxide.

5.2.3 WDM demultiplexer fabrication

Here we demonstrate a 4-channels microring-based add-drop demultiplexer using the traditional etched silicon strip waveguides fabrication method. We fabricate the filter on a 250 nm silicon-on-insulator wafer with 3 µm of buried oxide using CMOS fabrication processes (see Figure 5.4(a)). First the 450 nm x 250 nm channel waveguides are patterned using e-beam lithography (see Figure 5.4(b)) and chlorine-based etching (see Figure 5.4(c)). After stripping the resist, the etched photonic structures are clad with 1 µm of plasma enhanced chemical vapor deposition silicon oxide to confine the optical mode (see Figure 5.4(d)). Finally, 250 nm of nichrome (NiCr) microheaters are evaporated on top of the cladding (see Figure 5.4(e)) and 400 nm of gold (Au) contact wires passes current through the NiCr heaters to heat up the microring below (see Figure 5.4(f)).

The fabricated device is shown in Figure 5.5. The microring is of a racetrack shape, has a bending radius of 3.5 µm and a coupling length of 2.5 µm with a coupling gap of 200 nm.

5.2.4 WDM demultiplexer measurements and discussions

We achieve a passband width of 50 GHz in this single ring filter. We couple a quasi-TE light source into the device through a polarization controller. The light output at the through port and each of the drop ports are collected at the detector to measure the transmission spectrum (see Figure 5.6(a)). The channel spacing is 5 nm and the channel crosstalk is less than -20 dB. With the NiCr heaters, we can reconfigure the spectrum with a tuning efficiency of 1.2 mW/nm (see Figure 5.6(b)). However, due to the slow roll-off slope, one can anticipate

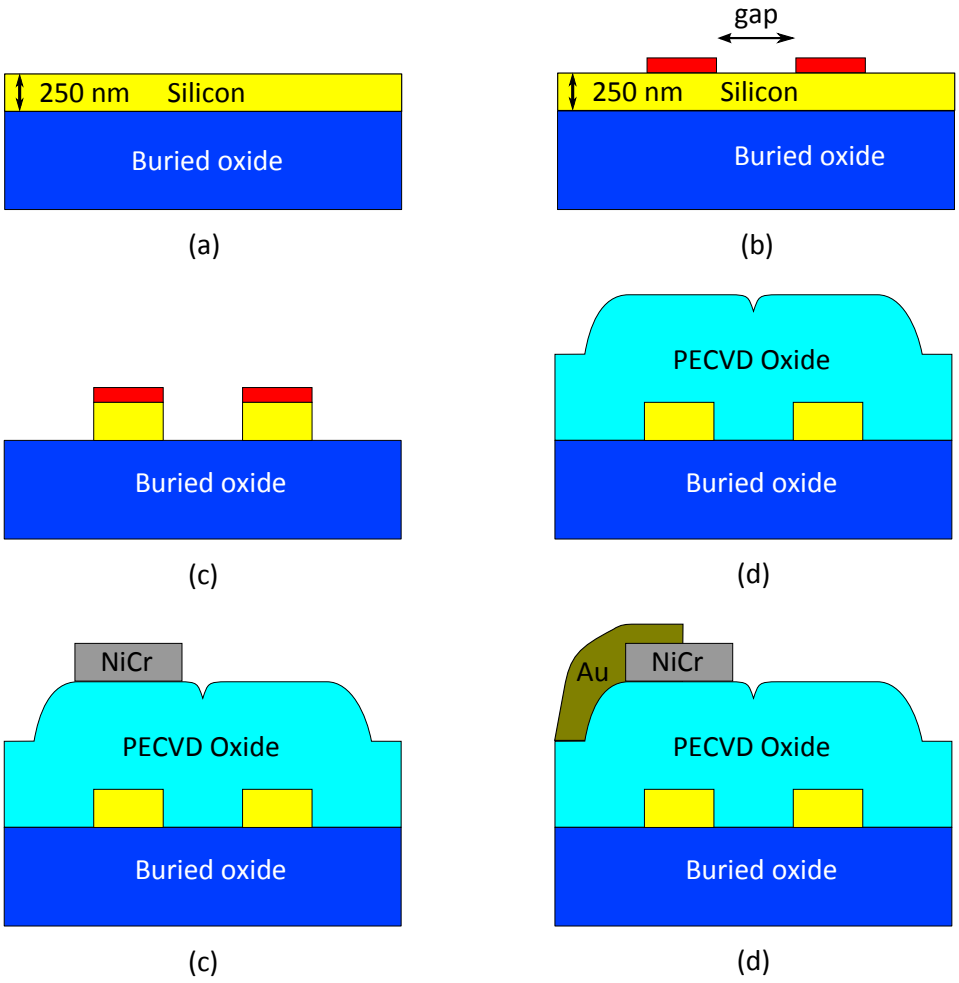

Figure 5.4: Silicon waveguide with integrated NiCr microheater fabrication process flow. (a) Use 250 nm silicon-on-insulator (SOI) as the device layer. (b) Patterning of the waveguides using ma-N 2403 resist, leaving a coupling gap between the ring resonator and bus waveguide. (c) Etching of the silicon layer. (d) Deposition of 1.0 µm PECVD silicon dioxide to confine the optical mode. (e) Evaporation of 250 nm NiCr on top of the cladding for the integrated microheater. (f) Evaporation of 400 nm Au for the contact wires.

that this type of single ring-based filters is subjected to higher channel crosstalk as the channel spacing becomes closer. This type of demultiplexers is therefore not suitable for demultiplexing closely packed WDM channels.

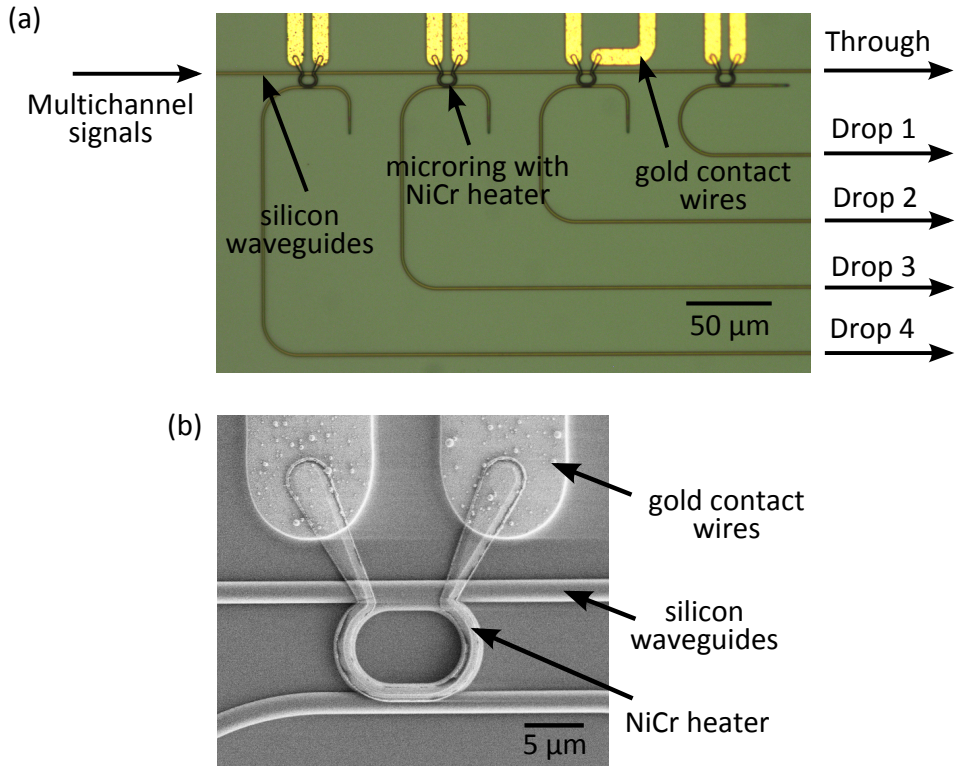

Figure 5.5: (a) Microscopic image of the 4-channels silicon WDM demultiplexers. (b) SEM image of each individual microring with integrated microheater on top.

5.3 On-chip Silicon Interleaver

5.3.1 Interleaver design

High bandwidth interleavers are essential for routing a large number of closely located WDM channels with high data-rate signals from one location to another location in a network [65]. A waveguide-based interleaver has been demonstrated using cascaded Mach-Zehnder interferometers (MZI), however this type of interleaver has a relatively large device footprint [66–68]. The number of cascaded MZI stages can be reduced and simplified by coupling ring resonators to

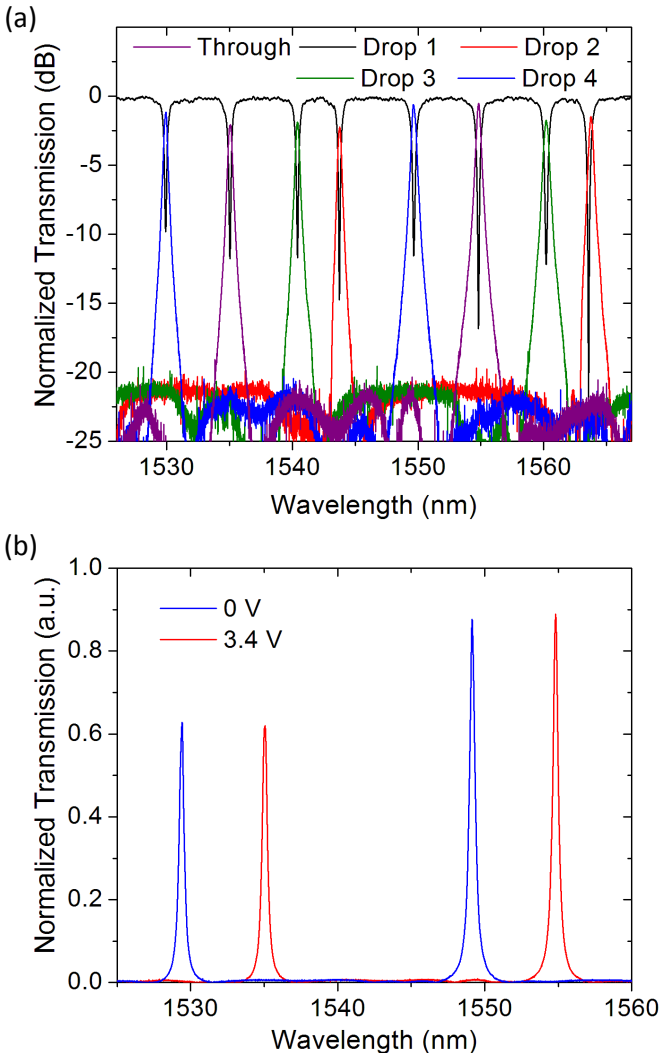

Figure 5.6: (a) Transmission spectrum of the through and drop ports of the demultiplexer. (b) Tuning of the drop port by thermal tuning of the microheater.

the MZI. In references [62, 69–71] silicon-based ring-assisted MZI interleavers have been designed and demonstrated, however their performance was limited in channel crosstalk and spectral range of operation due to the sensitivity of the device to fabrication imperfections.

To demultiplex the more densely packed channels in a WDM system, we design an interleaver that has the capability of separating and combining a comb

of WDM signals with low channel crosstalk and low signal distortion. The filtering function of such an interleaver is illustrated in Figure 5.7(a). When a comb of WDM signals is coupled into the input of the interleaver, the device operates as a demultiplexer by channeling signals "1" to the bar port and signals "2" to the cross port. This device also operates as a multiplexer when signals (1′ and 2′) are coupled into the add port. Signal 1′ is added to the signals at the cross port while signal 2′ is added to the signals at the bar port. The transmission spectra of both the bar and cross ports in such an interleaver have a flat passband, a fast roll-off on the band edges, and a low channel crosstalk (i.e. high extinction ratio between the passband of one channel and the stopband of an adjacent channel) [65]. Figure 5.7(b) shows the transmission spectra of this interleaver and illustrates the terminologies that are used in this paper. The free spectral range (*FSR*) in Figure 5.7(b) refers to one period of the transmission spectrum. Within this *FSR*, the signals denoted as "1" and "2" in Figure 5.7(a) are channeled to the bar port and to the cross port respectively. The channel crosstalk is an important figure of merit of an interleaver as it determines the effectiveness of the filter to suppress adjacent channels [72]. In this paper, we are optimizing the bandwidth for which the channel crosstalk is -20dB — the crosstalk of commercial telecom bandsplitter.

Figure 5.8(a) shows a design of an interleaver based on an asymmetric MZI and a ring resonator first proposed by Oda et al [73]. The MZI consists of two 3-dB couplers and a path difference between the two arms. The length of the ring resonator (L_{ring}) is twice the length of the path difference and the *FSR* of the interleaver is determined by L_{ring}. The ring resonator is coupled to the shorter arm of the MZI with a coupling coefficient of κ_1. The transfer function of this

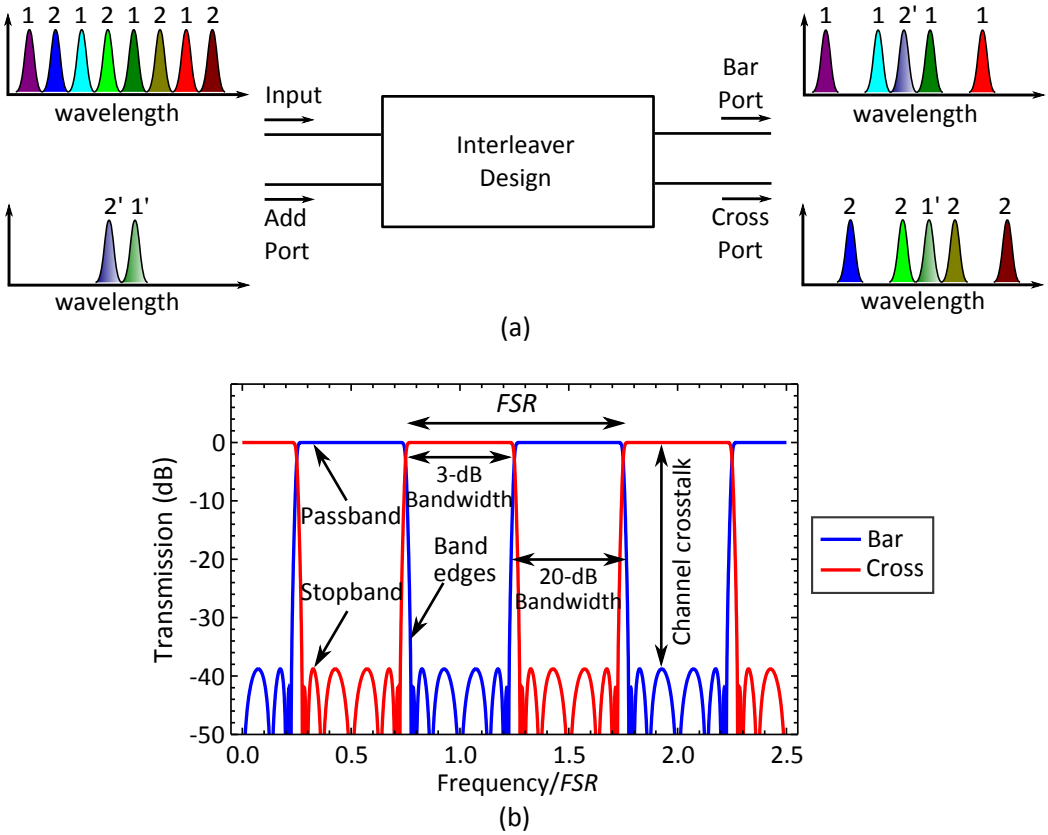

Figure 5.7: Filtering function of an interleaver. (a) Multiplexing and demultiplexing of a comb of WDM signals. (b) Transmission spectra of the interleaver, illustrating the terminologies used in this paper.

single ring-assisted MZI interleaveris given by [74]:

$$H_{\text{bar}}(z) = \frac{1}{c} 2 \left[\left(\frac{\rho_1 + z^{-2}}{1 + \rho_1 z^{-2}} \right) - z^{-1} \right], \tag{5.8}$$

$$H_{\text{cross}}(z) = \frac{-j}{2} \left[\left(\frac{\rho_1 + z^{-2}}{1 + \rho_1 z^{-2}} \right) + z^{-1} \right], \tag{5.9}$$

where $\rho_1 = (1 - \kappa_1)^{0.5}$, $FSR = \frac{2c}{n_g L_{\text{ring}}}$, $z = \gamma e^{j2\pi\nu}$, $\gamma = 10^{\alpha/20}$, α is the effective loss of the path difference or half the effective ring loss (in dB), $\nu = \frac{f}{FSR} = \frac{n_g L_{\text{ring}}}{2\lambda}$ is the frequency normalized to the FSR, c is the speed of light at vacuum, n_g is the group index of the device, and λ is the free space wavelength.

Considering a lossless device ($\alpha = 0$), we show the performance of such

a device for a coupling coefficient κ_1 of 0.89 (see Figure 5.8(d) – blue dotted line). This value was obtained from Equation 5.8 and 5.9 by optimizing the flatness of the passband response [21]. This device has a 20-dB bandwidth of 0.72 *FSR*. The slope of the band edges has a relatively slow roll-off and therefore the operating bandwidth of the device is low. It is essential to reduce the 20-dB bandwidth to as close as 0.5 *FSR* to fully utilize the entire operating spectrum. To further reduce the 20-dB bandwidth, we design higher order interleavers that have more ring resonators coupled to the arms of the MZI. When a second ring resonator is coupled to the longer arm of the MZI (see Figure 5.8(b)), the device is shown to have a faster roll-off on the band edges [22]. Figure 5.8(d) (green dashed line) shows that the 20-dB bandwidth of this double ring-assisted MZI interleaver is reduced to 0.61 *FSR*. Another third ring resonator can be coupled to the shorter arm of the MZI to form the triple ring assisted MZI interleaver (see Figure 5.8(c)). This design further reduces the 20-dB bandwidth to 0.55 *FSR* (see Figure 5.8(d) – red solid line). The transfer function of this triple ring assisted MZI interleaver is given by:

$$H_{\text{bar}}(z) = \frac{1}{2}\left[\left(\frac{\rho_1 + z^{-2}}{1 + \rho_1 z^{-2}}\right)\left(\frac{\rho_3 + z^{-2}}{1 + \rho_3 z^{-2}}\right) - \left(\frac{\rho_2 + z^{-2}}{1 + \rho_2 z^{-2}}\right)z^{-1}\right], \tag{5.10}$$

$$H_{\text{cross}}(z) = \frac{-j}{2}\left[\left(\frac{\rho_1 + z^{-2}}{1 + \rho_1 z^{-2}}\right)\left(\frac{\rho_3 + z^{-2}}{1 + \rho_3 z^{-2}}\right) + \left(\frac{\rho_2 + z^{-2}}{1 + \rho_2 z^{-2}}\right)z^{-1}\right], \tag{5.11}$$

where $\rho_1 = (1 - \kappa_1)^{0.5}$, i = 1, 2, or 3, $FSR = \frac{2c}{n_g L_{\text{ring}}}$, $z = \gamma e^{j2\pi\nu}$, $\gamma = 10^{\alpha/20}$, α is the effective loss of the path difference or half the effective ring loss (in dB), $\nu = \frac{f}{FSR} = \frac{n_g L_{\text{ring}}}{2\lambda}$ is the frequency normalized to the *FSR*, c is the speed of light at vacuum, n_g is the group index of the device, and λ is the free space wavelength.

The addition of even more ring resonators to the MZI arms helps to reduce the 20-dB bandwidth and therefore increase the operational bandwidth of the device. However, it also increases the attenuation of the transmitted signals due

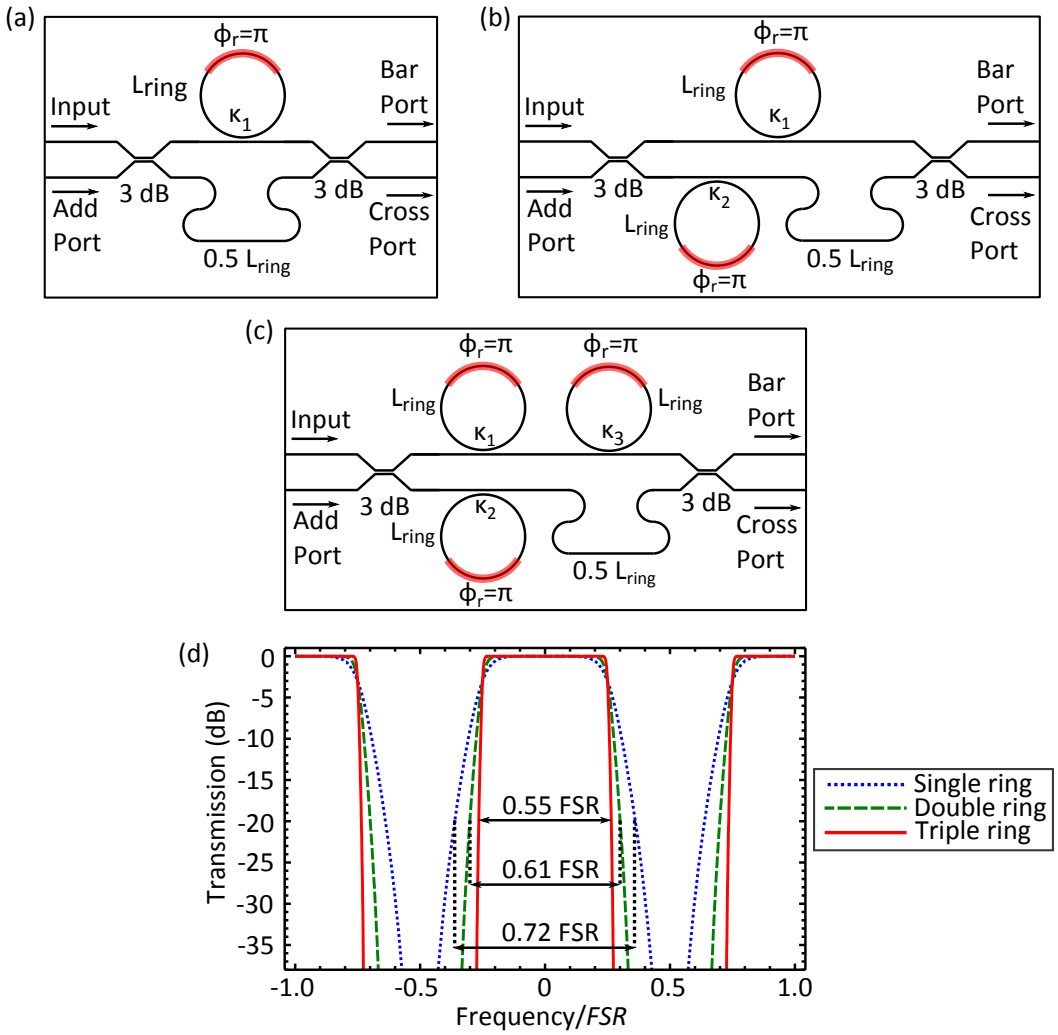

Figure 5.8: Schematic of ring assisted MZI interleavers. (a) Single ring assisted MZI interleaver. (b) Double ring assisted MZI interleaver. (c) Triple ring assisted MZI interleaver. (d) Calculated cross port transmission spectra of an optimal single ring (κ_1 = 0.89), optimal double ring (κ_1 = 0.97, and κ_2 = 0.62), and optimal triple ring (κ_1 = 0.96, κ_2 = 0.68, and κ_3 = 0.25) assisted MZI interleaver.

to the ring losses, as depicted by Equation 5.10 and 5.11. Figure 5.9 illustrates the impact of ring loss on the cross port transmission spectra of an optimal triple ring-assisted MZI interleaver. In a lossless case (α = 0), the spectral response of the interleaver has a flat passband and fast roll-off on the band edges (see Fig-

ure 5.9 – red solid line). The green dashed line and blue dotted line in Figure 5.9 show that as the ring loss increases to 2 dB per ring and 4 dB per ring, the insertion loss of the interleaver increases. The passband also becomes not as flat and the roll-off on the band edges becomes less steep.

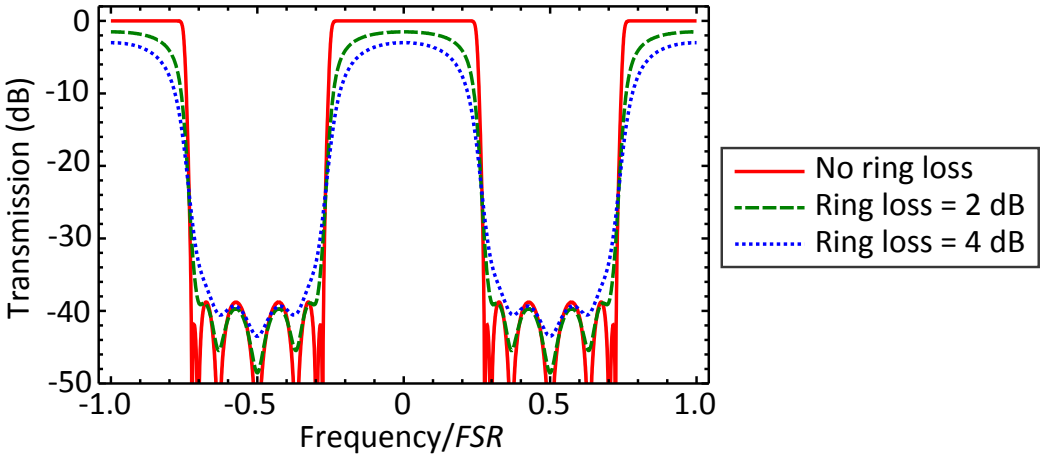

Figure 5.9: Impact of ring loss on the cross port transmission spectra of an optimal triple ring-assisted MZI interleaver.

The channel crosstalk of the triple ring assisted MZI interleaver is highly dependent on the combination of the coupling coefficients κ_1, κ_2, and κ_3. Assuming that the waveguides are lossless in this device, we analyzed the effects of the coupling coefficients according to Equation 5.10 and 5.11. Figure 5.10(a) shows the contour plot of the channel crosstalk of the interleaver as a function of κ_1 and κ_2, with κ_3 optimized to be 0.25 for a passband bandwidth requirement of 0.55 *FSR*. In order to achieve a channel crosstalk of less than -20 dB in the device, we need to operate within the blue region in the contour plot. One can observe from Figure 5.10(a) that the blue region occupies only a small area of the contour plot. This means that the values of κ_1 and κ_2 have to be controlled precisely. Figure 5.10(b) and 5.10(c) illustrate the high sensitivity of the device to small deviation of the coupling coefficient optimized values. Figure 5.10(b) shows

the transmission spectra of the interleaver at the optimum operation (κ_1 = 0.96, κ_2 = 0.68, and κ_1 = 0.25, indicated by the white cross in the contour plot). The channel crosstalk increases from -40dB to -12 dB (see Figure 5.10(c)) when the value of κ_1 changes from 0.96 to 0.8, indicated by the black cross.

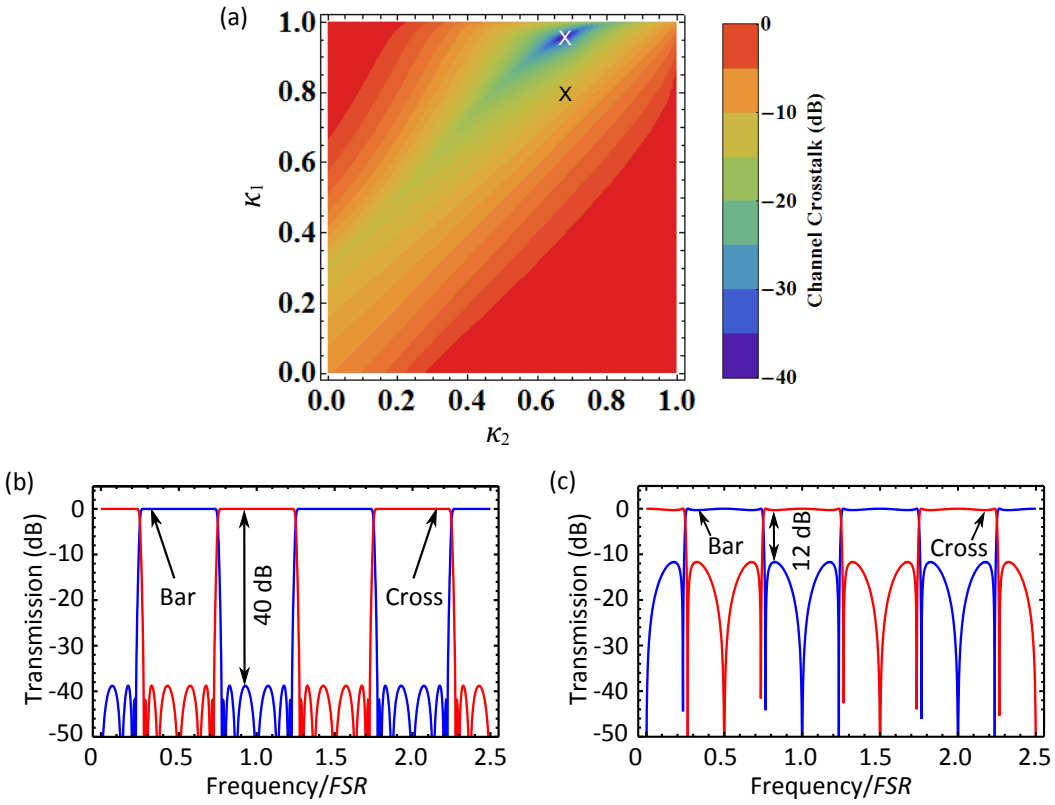

Figure 5.10: Triple ring assisted MZI interleaver. (a) Contour plot of the channel crosstalk as a function of κ_1 and κ_2, with the value of κ_3 optimized to be 0.25 for a passband bandwidth requirement of 0.55 *FSR*. (b) Simulated transmission spectra of the interleaver with κ_1 = 0.96 and κ_2 = 0.68, indicated by the white cross in the contour plot. (c) κ_1 = 0.8 and κ_2 = 0.68, indicated by the black cross.

In order to compensate for any fabrication imperfection, we design the device with full reconfiguration capability. To enable external control of each coupling coefficient independently, the waveguide-ring coupler is replaced with a thermo-optically tunable symmetric MZI coupler and the ring resonator with a

racetrack resonator (see Figure 5.11(a)) [75–78]. We do this modification to all the coupling regions, indicated by the blue regions in Figure 5.11(b). The effective coupling of each MZI coupler can be externally controlled by changing the phase difference $\Delta\varphi = \varphi_1 - \varphi_2$ between the two arms of the MZI. The effective coupling is given by $\kappa_{\text{eff}} = 4\kappa(1-\kappa)\cos^2(\Delta\varphi/2)$ where κ is the power coupling coefficient at each directional coupler of the MZI. The phase difference is controlled using the thermo-optic effect of silicon by placing a Nichrome (NiCr) heater on each arm of the MZI. To enable a full reconfiguration of κ_{eff} from 0 to 1, the value of κ is set to be 0.5 (3 dB). A NiCr heater is also placed on each racetrack resonator and the asymmetric MZI path difference to tune the effective phase of the device. The interleaver spectra can be shifted by one *FSR* by applying a π phase shift to the path difference between the asymmetric MZI arms for add-drop functionality. The merit of using thermal-optic tuning over carrier-induced tuning in this device is that it allows tuning over a larger range and the holding time is unlimited, whereas carrier-induced tuning is limited by thermal effects in the device. Additionally, in carrier-induced tuning, large amount of carrier injection into the silicon waveguides will result in a higher insertion loss of the device due to free carrier absorption [79].

5.3.2 Interleaver fabrication processes

In this work, the device is designed to have a *FSR* of 250 GHz by setting the length of the racetrack resonators (L_{ring}) to be 558 µm and the path difference between the MZI arms to be 279 µm. These values are calculated using the equation $FSR = \frac{2c}{n_g L_{\text{ring}}}$ by considering 450 nm x 250 nm channel waveguides with a group index of 4.3. We use a coupling gap of 200 nm and coupling length

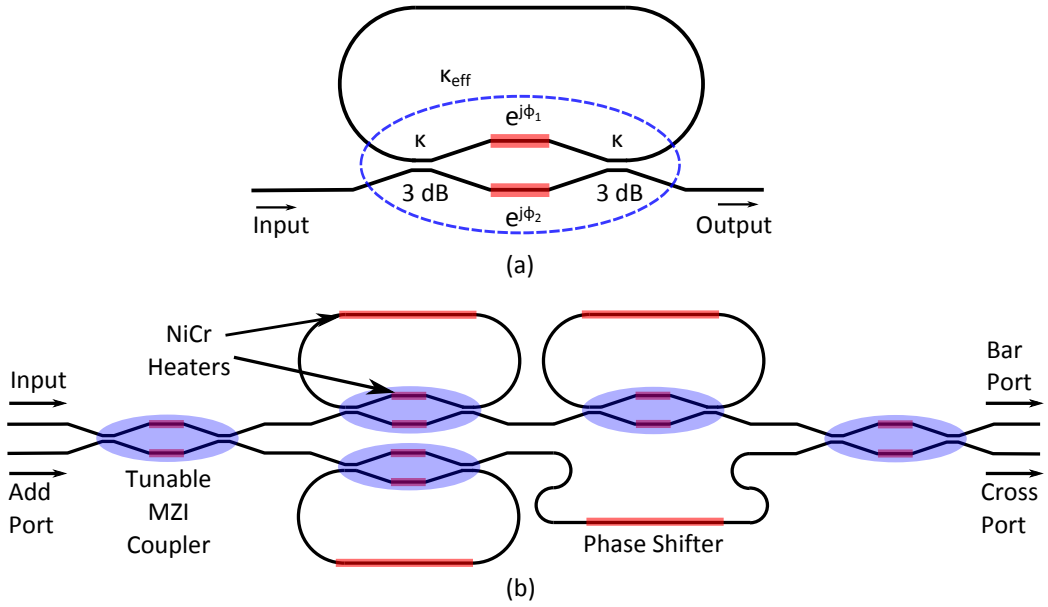

Figure 5.11: Triple ring assisted MZI interleaver. (a) Contour plot of the channel crosstalk as a function of κ_1 and κ_2, with the value of κ_3 optimized to be 0.25 for a passband bandwidth requirement of 0.55 *FSR*. (b) Simulated transmission spectra of the interleaver with $\kappa_1 = 0.96$ and $\kappa_2 = 0.68$, indicated by the white cross in the contour plot. (c) $\kappa_1 = 0.8$ and $\kappa_2 = 0.68$, indicated by the black cross.

of 10 µm to realize the 3 dB directional couplers. We employ NiCr heaters at the MZI arms and racetrack resonators above the cladding to change the phase of each region independently. The NiCr heaters are 2 µm wide and 260 nm thick.

We fabricate the fully reconfigurable interleaver on a 250 nm SOI wafer with 3 µm of buried oxide using standard CMOS fabrication processes [80]. First the 450 nm x 250 nm channel waveguides are patterned using e-beam lithography. The silicon waveguides are then etched using chlorine-based etcher. The e-beam resist is then stripped, and the etched structures are clad with 1 µm thick silicon oxide layer using plasma enhanced chemical vapor deposition to confine the optical mode. This 1 µm thick oxide cladding is sufficient to minimize the optical loss due to metal absorption [81]. 260 nm of NiCr are then evaporated

on the MZI arms and racetrack resonators above the cladding to create the 2 µm wide heaters. Finally, 300 nm of gold (Au) are evaporated to define the electrode contacts using a lift-off process. The final fabricated device is illustrated in Figure 5.12(a) and 5.12(b). The footprint of this triple ring-assisted MZI interleaver is 0.36 mm^2 without including the electrode contacts.

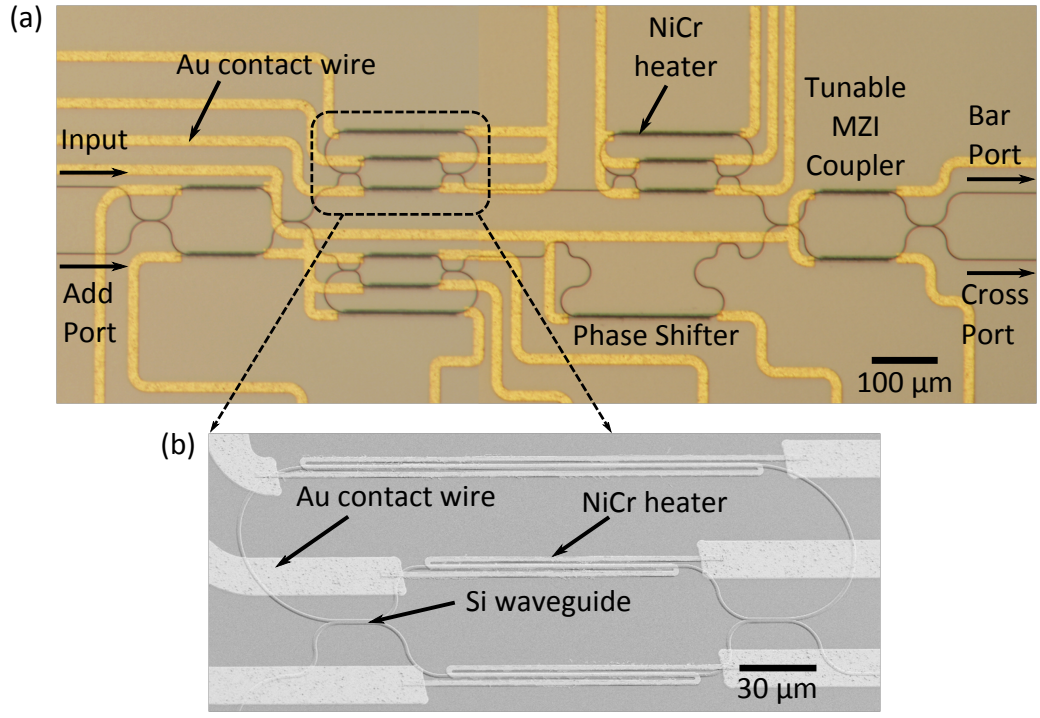

Figure 5.12: Final fabricated device. (a) Optical microscope picture. (b) Scanning electron microscope (SEM) picture of the racetrack resonator coupled to the arm of the MZI.

5.3.3 Results and discussions

Here we demonstrate a 120 GHz 3-dB bandwidth on-chip silicon photonic ring-assisted MZI interleaver that has a flat passband over a broad spectral range of 70 nm. This device is optimized to operate in the entire C-band with a channel

crosstalk as low as -20 dB. The device also has full reconfiguration capability to compensate for fabrication imperfections.

In order to characterize the device, we couple a tunable laser light source into the input port of the device through a polarization controller. The light output at the bar port and cross port are each collimated through a lens and collected at a photodetector to measure the transmission of TE polarized light (set by the polarization controller).

We thermally reconfigure the device to operate in the ideal coupling regime since the device performance is slightly suboptimal due to minor fabrication imperfections. Fine thermal-optic tuning is made to compensate for the fabrication imperfections. The total power consumption of this thermal reconfiguration is 5 mW. Figure 5.13(a) shows the transmission spectra of the device operating in the ideal coupling regime after thermal reconfiguration of the device. The total measured insertion loss from the fiber input to the output collected at the detector is 8 dB. It can be observed from the zoom-in spectra in Figure 5.13(b) that the device is optimized to operate in the C-band. The transmission spectra of the bar and cross ports from 1548 nm to 1558 nm are clean and complementary. The device has a 3-dB bandwidth of 120 GHz and a flat passband over a 70 nm spectral range (from 1530 nm to 1600 nm). The transmission spectra also show a fast roll-off on the band edges with a 20-dB bandwidth of 142 GHz (equivalent to 0.57 *FSR*). The lowest channel crosstalk within this spectral range is measured to be -20 dB. This measured crosstalk of -20 dB is higher than the previously calculated crosstalk of -40 dB in Figure 5.10(b) as it is assumed during the calculation that the waveguides are lossless and the power coupling coefficients of all the couplers are in the optimized values. The crosstalk, as observed in Fig-

ure 5.13(a), is not -20 dB over the entire 70 nm spectral range. The crosstalk is as low as -20 dB at 1550 nm but increases to -10 dB at the lower bound of 1530 nm and -6 dB at the higher bound of 1600 nm. This varying performance of the device over the 70 nm spectral range is attributed to the wavelength sensitivity of the coupling coefficients. The performance of the device can be improved significantly by implementing a wavelength-insensitive 3 dB MZI coupler [82, 83].

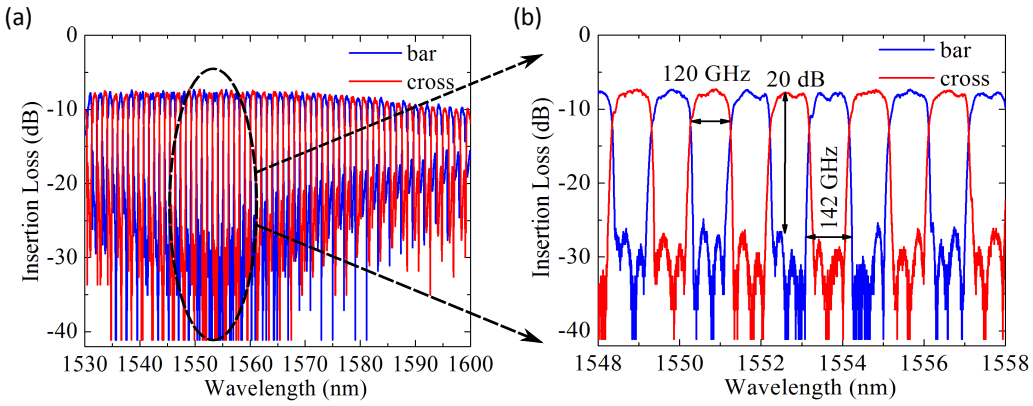

Figure 5.13: Operation of the fabricated device in the ideal coupling regime. (a) Transmission spectra of the bar and cross port. (b) Zoom-in of the section in (a).

We also operate the device in the non-ideal coupling regime before any thermal reconfiguration so as to verify the dependence of the channel crosstalk on the coupling coefficients (κ_1, κ_2, and κ_3). Figure 5.14(a) shows that the transmission spectrum of the bar port does not complement the cross port. One can see from the zoom-in spectra in Figure 5.14(b) that the channel crosstalk of the bar port is -5 dB and the crosstalk of the cross port is -10 dB.

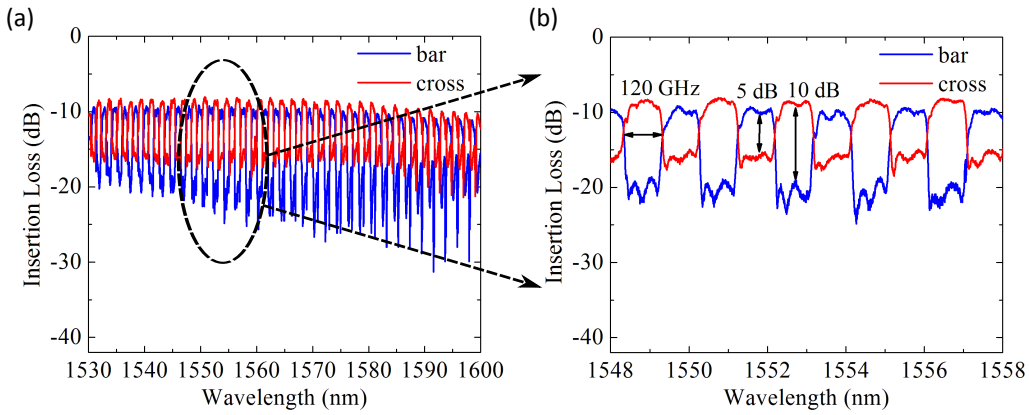

Figure 5.14: Operation of the fabricated device in the non-ideal coupling regime. (a) Transmission spectra of the bar and cross port. (b) Zoom-in of the section in (a).

5.3.4 Conclusion

We have demonstrated a 120 GHz 3-dB bandwidth on-chip silicon photonic interleaver based on 3 ring resonators coupled to the arms of an asymmetric MZI. The fabricated device exhibits a flat passband over a broad spectral range of 70 nm (1530 - 1600 nm). The spectra show a rapid roll-off on the band edges with a 20-dB bandwidth of 142 GHz (equivalent to 0.57 *FSR*). The device is optimized for operation in the C-band with a channel crosstalk as low as -20 dB. This device also has full reconfiguration capability to compensate for fabrication imperfections. Integration of this interleaver with high-speed on-chip modulators and photodetectors in a WDM system is promising.

CHAPTER 6

SIMULTANEOUS MODE- AND WAVELENGTH-DIVISION MULTIPLEXING ON-CHIP

6.1 Introduction

Current integrated photonics operate almost exclusively in the single-mode regime and utilize wavelength-division multiplexing (WDM) [84,85] which supports a limited scalability in bandwidth density. In contrast fiber communications is increasingly targeting multimode operation in conjunction with WDM to further scale the communication bandwidth transmitted per fiber [7]. Multimode communications in fibers have been demonstrated with space-division multiplexing (SDM) in multi-core fibers [86–90] or mode-division multiplexing (MDM) in few-mode fibers (FMF) [91–99] and have exploited each spatial mode as an independent channel.

Prior to this chapter, we have always utilized single-mode waveguides in quasi-TE polarization for WDM. Here in this chapter, we show a platform enabling MDM in conjunction with WDM in integrated photonics for on-chip and chip-to-chip ultra-high bandwidth applications [100]. This platform could increase the bandwidth density of on-chip interconnects, reduce the number of waveguide crossings for an on-chip interconnect, and add an additional design degree of freedom in future photonic networks.

Some of the key challenges of realizing on-chip MDM-enabled interconnects lie in creating mode (de)multiplexers with low modal crosstalk and loss which also support WDM (a key feature of many integrated-optics in-

terconnect designs). Previous implementations of on-chip mode multiplexing based on Mach-Zehnder interferometers [101, 102], Multi-Mode Interference (MMI) couplers [103–105], asymmetric directional couplers [106–108], and y-junctions [109–111] typically had large footprints, complex and strict design limitations, or only supported a limited number of optical modes. A compact and reconfigurable mode (de)multiplexer which can be straight-forwardly scaled to support numerous modes is essential for realizing MDM-WDM in integrated photonics.

6.2 Selective mode coupling by phase matching

We demonstrate on-chip MDM-WDM by engineering the propagation constants of high-confinement photonic structures in order to enable selective coupling to different spatial modes at different wavelengths. The silicon photonic platform is attractive for implementing this approach as the propagation constants of the different spatial modes can be engineered to differ significantly thanks to the high core-cladding (Si/SiO_2) index contrast. We choose a waveguide height for which the confinement is high and therefore widely different propagation constants can be achieved by varying the waveguide width. Figure 6.1(a) shows that for a given 250-nm tall silicon waveguide a large range of effective indices from 2.0 to 2.9 can be achieved corresponding to the propagation constants of the TE_0 through TE_4 spatial modes at λ = 1550 nm. Based on propagation constant matching, an optical mode in a single-mode waveguide can be evanescently coupled to a single spatial mode in an adjacent multimode waveguide, where the coupling strength to the mode will depend on the width of the multimode waveguide.

In order to realize a compact MDM device, we employ single-mode microring resonators to selectively couple to the different spatial modes in a multimode waveguide. In order to realize WDM capabilities, we design the free-spectral range (*FSR*) of the microrings to match the wavelength channel spacing. The device, which is designed to operate in TE mode, comprises of three identical microrings coupled to a multimode waveguide (see Figure 6.1(b)). Each microring, made up of a 450-nm wide waveguide, is designed to support only the fundamental TE mode with an effective index of 2.46. The multimode bus waveguide comprises of several sections with tapering widths ranging from 450 nm to 1.41 μm. When the bus waveguide width corresponds to 450 nm, 930 nm, or 1.41 μm, the effective indices of TE_0, TE_1, or TE_2 modes respectively match the effective index of the TE_0 mode of the microrings (n_{eff} = 2.46) and therefore couple efficiently to the resonators. The three insets in Figure 6.1(b) show such coupling of the TE_0 mode of the microring to the TE_0, TE_1, or TE_2 modes in the bus waveguide. Since the propagation loss in silicon ring is low, a low coupling strength (achievable with a short coupling length) at the two ring-waveguide coupling regions is sufficient to transfer all the power from the single-mode input waveguide to the multimode bus waveguide [39]. We design the ring resonance linewidth to be at least 15-GHz in order to enable 10-Gb/s data transmission with negligible signal degradation. We also include an integrated heater on top of each microring to tune the ring resonances to align to the WDM channels and thereby optimize the performance of the device [81]. This design can be easily modified to handle additional phase-matched modes by widening the multimode waveguide (Figure 6.1(a)).

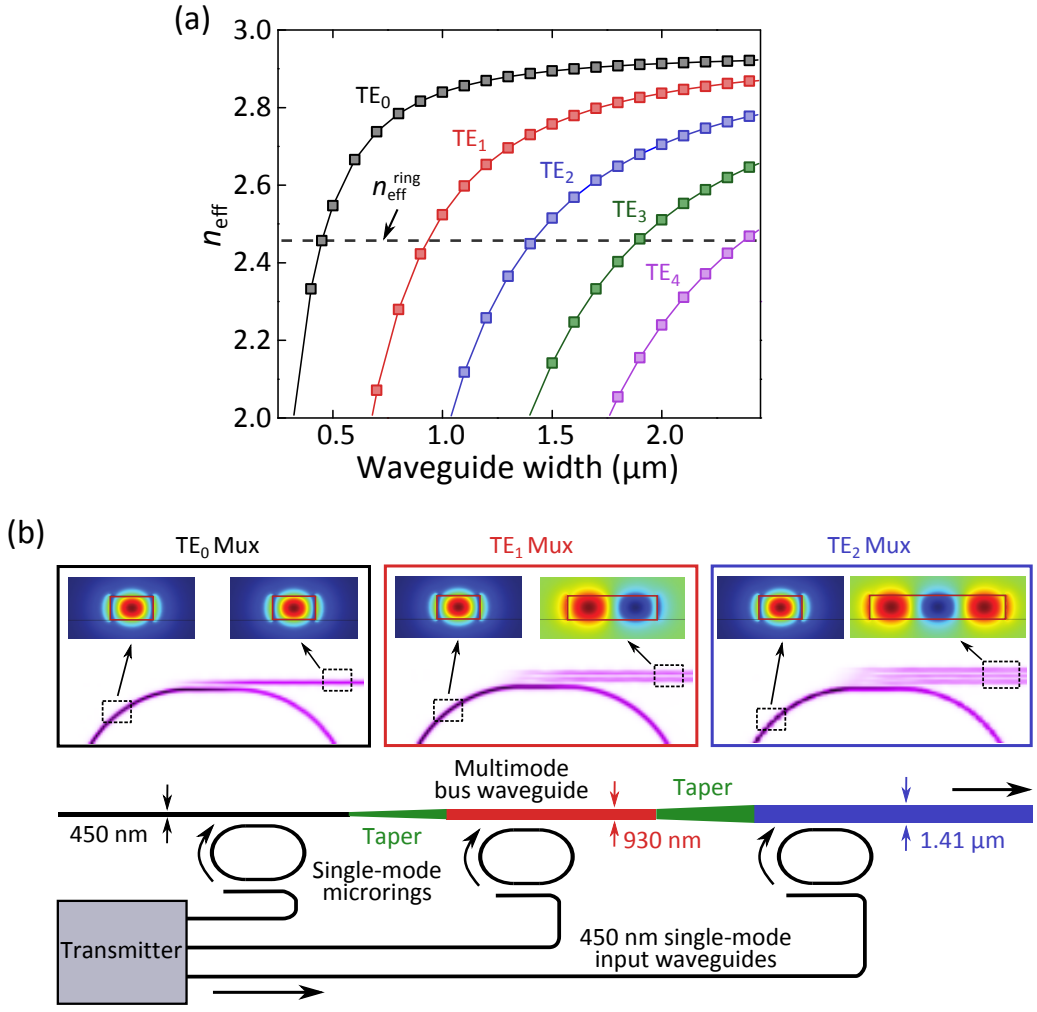

Figure 6.1: Phase matching condition for 250 nm tall silicon waveguides. (a) Simulated effective index of the optical modes in waveguide of different widths at $\lambda = 1550$ nm. (b) Selective coupling of the single-mode microrings to a specific spatial mode in the multimode bus waveguide with each section of the multimode waveguide linked by adiabatic tapered waveguides. The insets show the selective coupling of each multiplexer (TE$_0$, TE$_1$, and TE$_2$).

6.3 Device design and fabrication

We fabricate the reconfigurable MDM-WDM silicon microring resonators on a 250 nm SOI wafer with 3 μm of buried oxide using standard CMOS fabrication

processes. We patterned the waveguides using e-beam lithography with the dimensions as followed: the input/output ports and the microring are 450 nm wide; the TE_0, TE_1, and TE_2 (de)multiplexers have a width of 450 nm, 930 nm, and 1.41 µm wide; and each (de)multiplexer is linked by an adiabatic taper of 80 µm long. All the microrings have a radius of 10 µm and a coupling length of 5 µm. The separation gap between the microrings and all the input waveguides is 240 nm while the separation gap between the microrings and TE_0, TE_1, and TE_2 (de)multiplexers are 240 nm, 200 nm and 200 nm respectively. The silicon waveguides are then etched, followed by the e-beam resist being stripped and the etched structures are clad with 1 µm thick silicon oxide layer using plasma enhanced chemical vapor deposition to confine the optical mode. 300 nm of NiCr are next evaporated on the microrings resonators above the cladding to create the 1 µm wide heaters. Finally, 500 nm of gold (Au) are evaporated to define the electrical wires and contact pads using a lift-off process. The final fabricated device is illustrated in Figure 6.2. The footprint of this device is 0.11 mm^2 excluding the electrical wires.

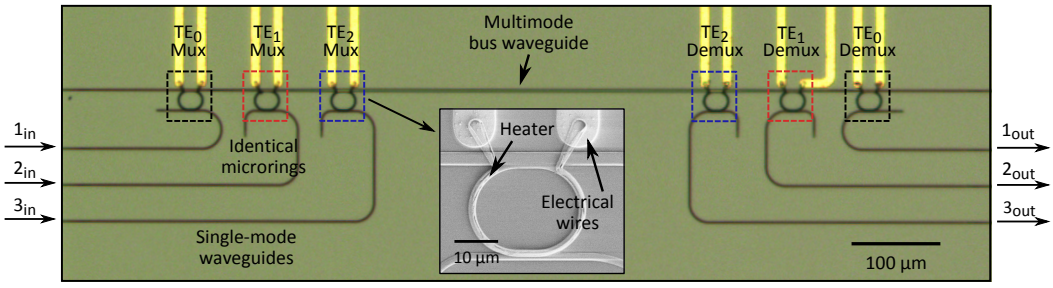

Figure 6.2: Microscope image of the fabricated device. Inset: SEM showing the heater to tune each individual ring resonator.

6.4 Optical modes imaging

We image the optical modes at the output of the multimode waveguide to verify the excitation of the different spatial modes. We fabricate a test device that only has the mode multiplexer section (TE_0, TE_1, and TE_2) and is terminated with the 1.41-µm wide multimode bus waveguide. We couple a 1547 nm laser (on-resonance of each microring) into one of the input ports at one time. The output spatial modes of the multimode waveguide are then magnified with a 40× aspheric lens and imaged on an IR camera as shown in Figure 6.2. We observe well-defined TE_0, TE_1, and TE_2 modes as predicted by simulation (Figure 6.3).

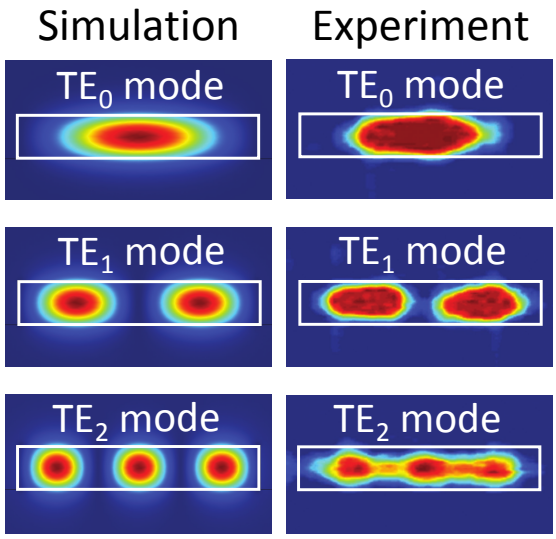

Figure 6.3: Simulated and experimental images of the optical modes at the cross-section of the multimode waveguide.

6.5 Optical crosstalk

6.5.1 Crosstalk measurements

We show that the fabricated mode multiplexers introduce crosstalk as low as -30 dB between the modes. From the spectral transmission scans for each combination of input and output ports, we can quantify the amount of crosstalk resulting from the spatial mode multiplexing and demultiplexing. Figure 6.4(a) shows the transmission spectrum at output port 1 (see port definitions in Figure 6.2) from each input. The insertion loss of this port is 13 dB and the optical crosstalk (defined as the ratio of desired signal power to the sum of the interfering channels' power) is as low as -30 dB. The insertion loss of port 2 is 16 dB and the optical crosstalk is -18 dB (Figure 6.4(b)). The insertion loss of port 3 is 26 dB and crosstalk is -13 dB (Figure 6.4(c)). The main contribution to the insertion loss is the aggregate 10-dB fiber-to-chip coupling loss. The rest of the insertion loss is attributed to the waveguide propagation loss and ring intrinsic loss. By ensuring critical coupling between the waveguides and rings, achievable on-chip losses of this device are expected to total around 1.5 dB. The higher insertion loss in port 3 compared to the other 2 ports is due to a suboptimal ring coupling gap.

6.5.2 Minimizing the crosstalk

The crosstalk from the unwanted input signals can be minimized by optimizing the coupling length between the ring and the multimode waveguide to reduce coupling of undesired modes. Coupled-mode theory for two weakly coupled

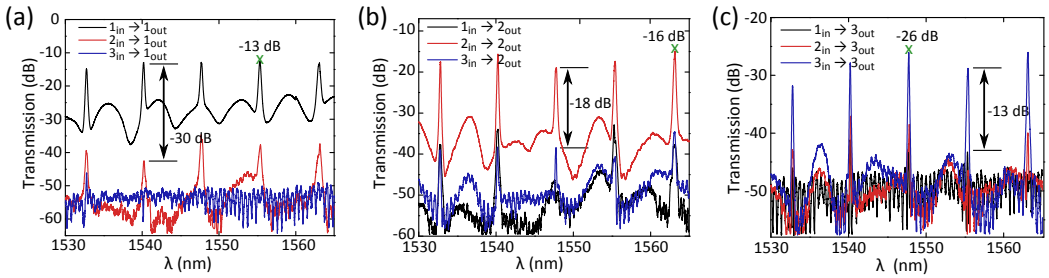

Figure 6.4: Optical transmission and crosstalk at the three output ports for signal injection on each of the three input ports. (a) Output port 1. (b) Output port 2. (c) Output port 3.

optical modes relates the complex amplitudes of the modes, a_1 and a_2 through a set of differential equations [112]:

$$\frac{da_1}{dz} = -j\beta_1 a_1 + \kappa_{12} a_2, \tag{6.1}$$

$$\frac{da_2}{dz} = -j\beta_2 a_2 + \kappa_{21} a_1, \tag{6.2}$$

The solutions to this equation set, assuming the waves $a_1(0)$ and $a_2(0)$ are launched at z = 0, are given by:

$$a_1(z) = \left[a_1(0)\left(\cos\beta_0 z + j\frac{\beta_2 - \beta_1}{2\beta_0}\sin\beta_0 z\right) + \frac{\kappa_{12}}{\beta_0} a_2(0)\sin\beta_0 z \right] e^{-j[(\beta_1+\beta_2)/2]z}, \tag{6.3}$$

$$a_2(z) = \left[\frac{\kappa_{21}}{\beta_0} a_1(0)\sin\beta_0 z + a_2(0)\left(\cos\beta_0 z + j\frac{\beta_1 - \beta_2}{2\beta_0}\sin\beta_0 z\right) \right] e^{-j[(\beta_1+\beta_2)/2]z}, \tag{6.4}$$

where

$$\beta_0 = \sqrt{\left(\frac{\beta_1 - \beta_2}{2}\right)^2 + \kappa_{12}\kappa_{21}}. \tag{6.5}$$

If the initial waves $a_1(0) = 1$ and $a_2(0) = 0$ are assumed, then the coupling from a_1 to a_2 is given by $\left|\frac{\kappa_{21}}{\beta_0}\sin\beta_0 z\right|$. Below we take a look at the example of the 1.41-μm wide multimode waveguide and investigate the coupling strength between the phase-matched TE_2 spatial mode and the TE_0 mode of 450-nm wide waveguide at $\lambda = 1.55$ μm (see Figure 6.5(a)). The coupling gap between the two different waveguides is fixed at 200 nm. To achieve 100% power transfer from the 450-nm

waveguide (TE_0) to the 1.41- μm waveguide (TE_2) using a directional coupler and vice versa, the coupling length ($L_{coupling}$) is required to be 42 μm (see Figure 6.5(c)). To realize a compact device, we use microring resonators instead of a directional coupler. Weak coupling (achievable with a short coupling length) is sufficient to transfer nearly all the power from the input waveguide of the microring to the multimode waveguide (typically termed critical coupling) [39] (see Figure 6.5(b)). We also calculate the coupling strength of the unwanted modes (TE_1, TE_0) which determines the crosstalk of the device. We observe that there is coupling to the undesired modes (TE_1, TE_0), however the coupling is weak due to the phase mismatch between these modes. The maximum coupling strength of TE_1 mode is 0.057. The optimum operating regime for low crosstalk is at $L_{coupling} \approx 6$ μm where the coupling to the undesired modes (TE_1, TE_0) is minimized.

We expect the crosstalk at output port 3 of the current device to be less than -16 dB for an optimized coupling length of 6 μm (larger than the fabricated one with only 5 μm) (see Figure 6.6(a)). The crosstalk can be further reduced by introducing weaker coupling at the microring-multimode waveguide coupling region (by having a larger coupling gap) to lower the maximum coupling of the undesired modes at the expense of longer coupling length to maintain the critical coupling condition. Figure 6.6(b) shows the coupling strength of the same microring-waveguide except that the coupling gap is changed to 280 nm. This weaker coupling at the coupling region lowers the maximum coupling strength of the TE_2 mode from the initial value of 0.057 to 0.037. This in turn results in a longer coupling length to maintain the critical coupling condition.

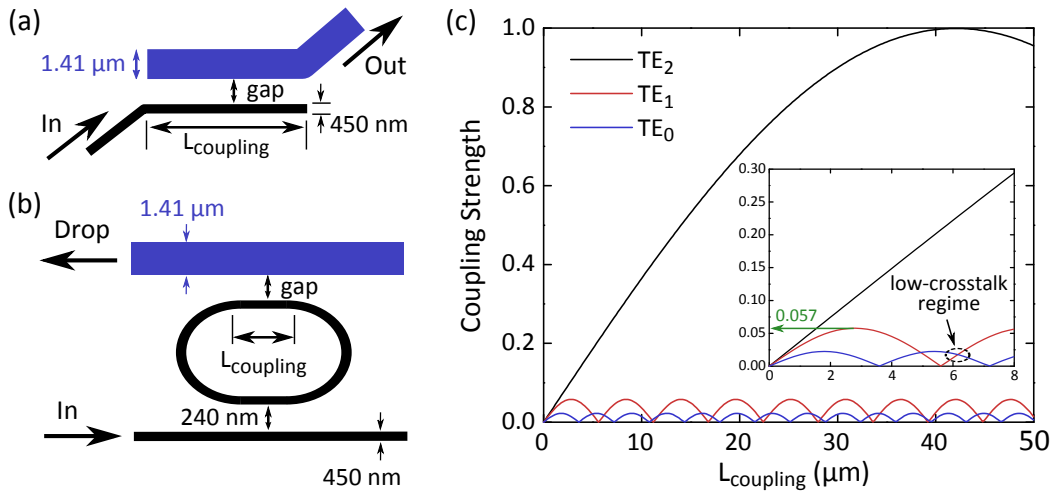

Figure 6.5: Coupling strength of different spatial modes (TE_2, TE_1, TE_0) of a 1.41-μm wide waveguide to the TE_0 mode of a 450-nm wide silicon waveguide with a coupling gap of 200 nm. (a) Schematic of the coupling between a 1.41-μm wide waveguide and a 450-nm wide silicon waveguide. (b) Schematic of an add-drop microring with asymmetric input and drop waveguides. (c) The maximum coupling strength of TE1 mode is 0.057. The optimum operating regime for low-crosstalk regime is at $L_{coupling} \approx 6$ μm.

6.6 Mode- and wavelength-division multiplexing link

6.6.1 3-Mode × 10-Gb/s multiplexing link

We simultaneously launch a single 10-Gb/s data channel into all the 3 input ports of the mode multiplexer and measure a small power penalty (less than 1.9 dB for BER of 10^{-9}) on each output port of the mode demultiplexer.

The experimental setup for performance evaluation is illustrated in Figure 6.7(a). In order to measure these power penalties the laser channel at 1563 nm is modulated with PRBS $2^{31} - 1$ on-off-keyed (OOK) data by an amplitude modulator and then further phase-imprinted with a swept-frequency sinusoid

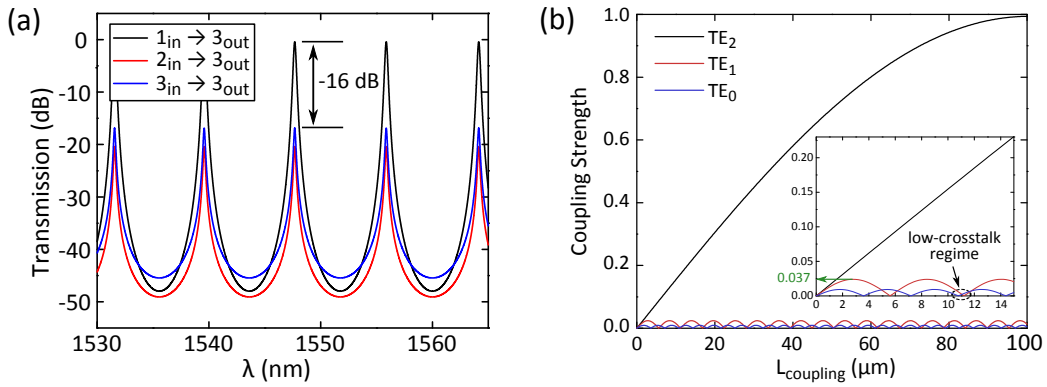

Figure 6.6: (a) Simulated transmission and crosstalk levels at output port 3 with optimized coupling length of 6 μm. Similar transmission curves for outputs 1 and 2 are expected for optimized coupling lengths of 4 μm and 4.5 μm, with simulated crosstalks <-30 dB and <-25 dB respectively. (b) Coupling strength of different spatial modes (TE_2, TE_1, TE_0) of a 1.41-μm wide waveguide to the TE_0 mode of a 450-nm wide silicon waveguide with a coupling gap of 280 nm. The maximum coupling strength of TE_1 mode is 0.037. The optimum operating regime for low-crosstalk regime is at $L_{coupling} \approx 11$ μm.

in order to enable bit-error-rate (BER) measurements on channels which experience coherent crosstalk. Intra-channel crosstalk [113] results in coherent interference of the laser with itself. In a test setup not employing any phase decoherence mechanisms, this results in a slow change of the output signal power as the phases leading to the device under test change as a result of thermal fluctuations in the fibers. If this remains untreated, these power fluctuations (on the temporal order of multiple seconds) prevent accurate BER measurements over short time spans. In order to enable finite-time BER measurements, two mechanisms are employed simultaneously to average out the slow phase fluctuations: 1. The arms leading to the multiplexer input ports are decorrelated by at least 0.5 km SSMF. This is close to the 1-km coherence length of the 200-kHz linewidth lasers we used in the experiments therefore ensuring some phase decoherence of the

signals. 2. In order to guarantee full phase orthogonality regardless of the intrinsic laser linewidth, we incorporate phase modulation of a repeating linearly chirped signal consisting of a frequency sweep from 20-MHz to 10-MHz over a 5-ms period. With a 0.5-km path difference (roughly 2.5 μs relative delay), the phase difference between adjacent ports oscillates over 2π at 5-kHz, guaranteeing averaging of the phase difference in power measurements averaged over 100 ms.

The data signal is then amplified, split evenly between the 3 input ports of the on-chip mode multiplexer, and simultaneously injected in quasi-TE polarization to the multiplexer ports. The varying fiber spans leading to the device ensure that the data is decorrelated between the ports. The data channels coupled to the device's ports are decorrelated by 0.5-km and 1-km long fiber delays which ensure the patterns are relatively shifted between ports by at least 24 kb out of the pattern length of 2 Gb ($2^{31} - 1$ PRBS). We employ a method similar to one previously reported [114]; we couple to three input ports simultaneously using a Pitch Reducing Optical Fiber Array (PROFA) mounted on a fully angle adjustable stage. The PROFA alignment was optimized to be within 2-dB of the optimal coupling values for all the ports simultaneously. Output coupling is done with a tapered lensed fiber aligned to one output port at a time.

The demultiplexed signals are recovered one at a time for inspection on a DCA and BER evaluation. Error free transmission (BER $< 10^{-12}$) and open eye diagrams (Figure 6.7(a),(b)) are observed for all output ports. To account for fabrication imperfections, we improve the performance of port 3 at the expense of increased crosstalk and spectral filtering penalties on port 2 by wavelength detuning the TE_1 multiplexer ring. This enables device operation with an over-

all balanced power penalty (measured at a BER of 10^{-9}) of 1.9 dB on ports 2 and 3 and 0.5 dB on port 1. In order to verify that intra-channel crosstalk is indeed the main mechanism of signal degradation [113], we also inspect the channel performance with only one input port injected at a time. We observe that transmission penalties result in 0.1 dB penalties on ports 1 and 2 and 0.8 dB on port 3 (with the higher penalty on port 3 resulting from the higher insertion loss through this port which leads to a larger OSNR degradation at the post-chip EDFA). Therefore we conclude that crosstalk is the main contributing factor to signal degradation in this device. Intra-channel crosstalk penalties result in a power penalty predicted analytically as $\mathrm{PP} = -10\log_{10}(1 - 2\sqrt{\varepsilon})$ where ε is the ratio of the desired-signal's power to interfering signals' powers. The penalties are measured relative to a back-to-back (B2B) reference case which is defined and measured by replacing the chip with a tunable attenuator set to replicate the fiber-to-fiber loss of the lowest insertion-loss port.

6.6.2 2-Mode × 3-Wavelength × 10-Gb/s MDM-WDM link

We measure a low (< 1.4 dB) power penalty for joint MDM-WDM operation by launching three different 10-Gb/s wavelength channels spanning the full C-band into two input ports of the multiplexer (ports 1 and 2). A modified setup (depicted in Figure 6.8(a)) is used to correctly decorrelate the wavelength channels. The wavelength channels are first decorrelated using the dispersion of a 0.5-km fiber to achieve at least 90-bit relative delay between adjacent wavelength channels. The inputs to the two ports used in this experiment are also decorrelated by a fixed 1-km fiber delay which guarantees decorrelation between the ports used. More polarizers are included in the experiment to ensure

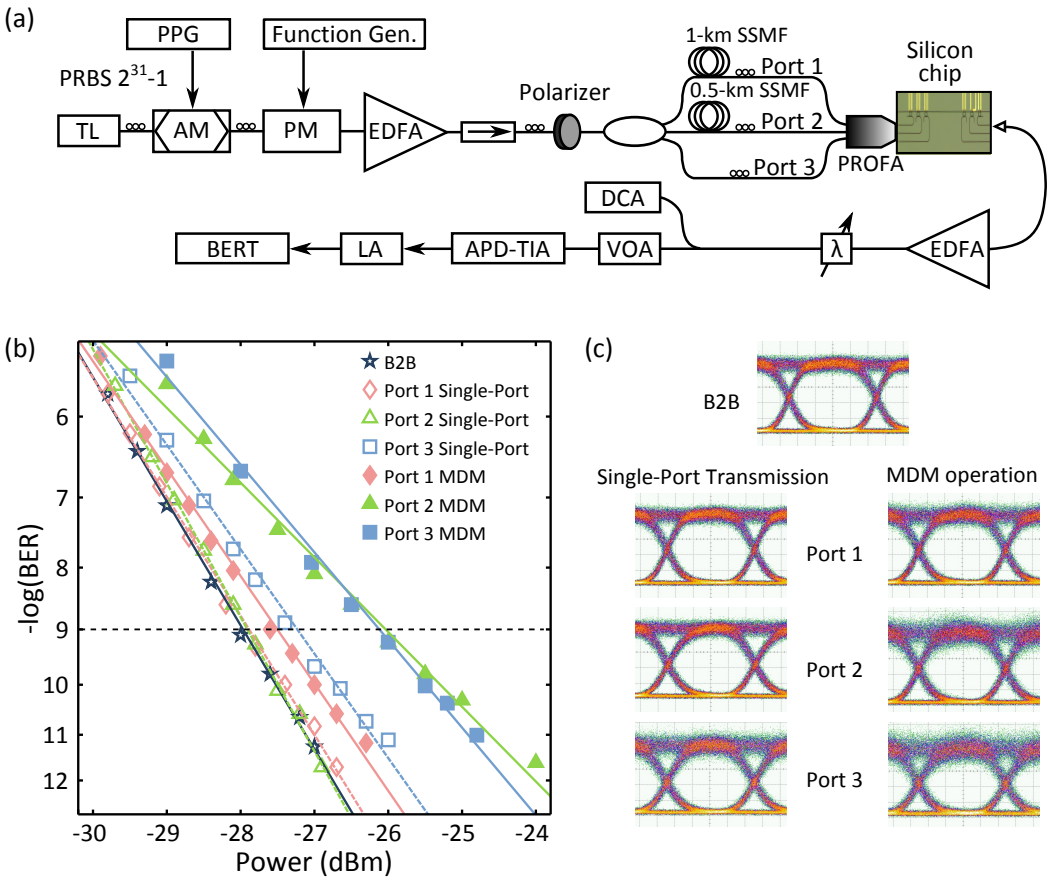

Figure 6.7: 3-Mode × 10-Gb/s Multiplexing Link. (a) Experimental setup for performance evaluation including Pulsed Pattern Generator (PPG), Tunable Laser (TL), Amplitude Modulator (AM), Phase Modulator (PM), Erbium-Doped Fiber Amplifier (EDFA), Isolator (→), Standard Single Mode Fiber (SSMF), Tunable Filter (λ), Digital-Communications Analyzer (DCA), Variable Optical Attenuator (VOA), Avalanche-Photodiode (APD-TIA), Limiting Amplifier (LA), and Bit-Error-Rate Tester (BERT). (b) BER measurements for back-to-back (B2B) test case, single port transmission, and MDM operation for all 3 ports. (c) Corresponding eye-diagrams for the inspected signals.

that all the wavelength channels are launched on chip at the quasi-TE polarization with equal power. We set the wavelength channels to span the full C-band (limited by the EDFA gain band) and the microrings are tuned on-resonance to maximize power transmission at 1547 nm. The power penalties for both ports

vary between 0.6 and 1.4 dB for all three wavelength channels (Figure 6.8(b)) with performance variation attributed to slightly varying levels of crosstalk for the different wavelength channels. Error free transmission (BER $< 10^{-12}$) and open eye diagrams (Figure 6.8(c)) are observed for all the three channels at the two output ports. These results show that only a minimal penalty is added by extending the device operation to support WDM concurrently with the MDM.

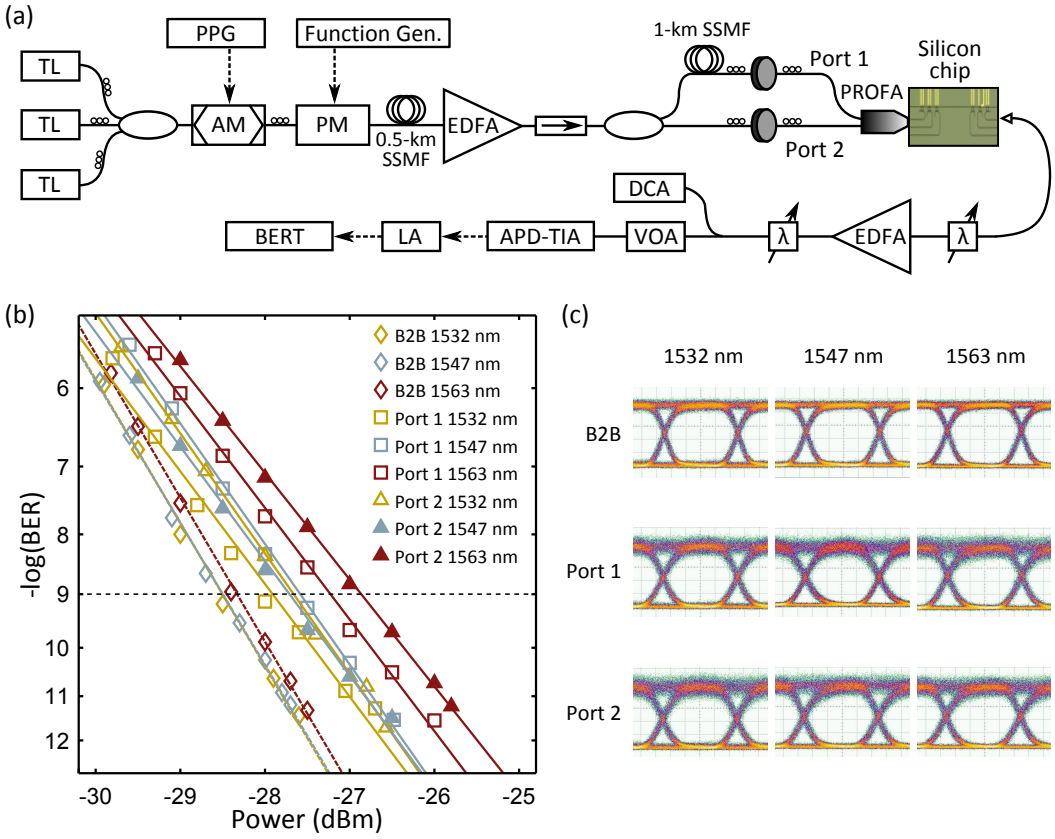

Figure 6.8: 2-Mode × 3-Wavelength × 10-Gb/s MDM-WDM link. (a) Experimental setup for demonstrating combined MDM and WDM operation. (b) BER measurements for back-to-back (B2B) test cases and full MDM-WDM operation for both ports. (c) Corresponding eye-diagrams for the inspected signals.

6.7 Conclusion

In conclusion, we have shown a platform that enables on-chip MDM-WDM optical interconnection for ultra-high bandwidth communications. Our simulation in Figure 6.1(a) showed that when the multimode bus waveguide width tapers up to 2.37 μm, 5 spatial modes can be supported by this platform. In principle using a wider waveguide one could support an even larger number of modes. Each microring resonator in practice is able to support 87 WDM channels over the entire C-band (1530 – 1565 nm) by increasing the microring size such that the channel spacing is 50 GHz. Therefore, the on-chip MDM-WDM platform with the above-mentioned dimensions can potentially support an aggregate data rate up to 4.35 Tb/s with 5 spatial modes and 87 WDM channels.

CHAPTER 7

SUMMARY AND FUTURE WORK

Due to the fact that the demand for faster data rate traffic increases exponentially with the prediction of Moore's Law, it is critical that we can solve this bandwidth bottleneck with a new technology. We had discussed about the emergence of silicon photonics for on-chip optical interconnects for high bandwidth chip-to-chip and intra-chip applications. Specifically, the use of multiplexing (such as wavelength-division multiplexing and mode-division multiplexing) allows a high aggregate data rate.

It is important for on-chip silicon waveguides to be low-loss in order to allow low device insertion loss and omit the need for high input optical power. We introduced an etchless silicon waveguide fabrication method which makes use of selective silicon oxidation to define the waveguides that are not exposed to any plasma etching. This method reduces the waveguide loss from 3 dB/cm to 0.3 dB/cm.

We fabricated high-Q microring resonators using this etchless silicon method. We obtained an intrinsic quality factor of 510,000 with an ultra-low coupling loss of approximately 1.5 dB per facet. We observed an atypical resonance blue shift with optical power in this kind of etchless silicon microrings whereas typically resonance red shift is observied in etched silicon microrings. This is due to the fact that the etchless silicon microring has very smooth sidewall and less recombination sites at the interface. As a result, the free carrier lifetime is one order of magnitude higher than the etched silicon waveguides, therefore free carrier dispersion dominates over the thermo-optic effect caused by the two-photon absorption and free carrier absorption. We makes use of

the interplay between the free carrier dispersion and the thermo-optic effect to induce either resonance red shift, blue shift or resonance-insensitive to optical power.

We proposed a scheme of wavelength-divison multiplexing using an efficient interleaver to demultiplex the closely located WDM channels and a simple add-drop microring filter to demultiplex the more sparsely located WDM channels. The interleaver has a rapid roll-off slope with a 20-dB bandwidth of 142 GHz and a channel crosstalk as low as -20 dB. Additionally, it can operate over a broad spectral range of 70 nm. We also demonstrated a 4-channels microring-based demultiplexer with a passband width of 50 GHz, channel spacing of 5 nm and a crosstalk of less than -20 dB. With the combination of the interleaver and microring demultiplexers, we can (de)multiplex the channels over the entire C-band with potential terabits per second aggregate data rate with low crosstalk.

The highlight of this dissertation is that we demonstrated simultaneous mode- and wavelength-division multiplexing in integrated photonics. To the best of our knowledge, this work is the first demonstration of its kind at the moment. We utilized single-mode microrings to selectively couple to specific modes on a bus waveguide achieved by phase matching. Each microring has an integrated microheater to tune the ring resonance for optimization purpose. We verified from the optical mode imaging with IR camera that this type of microring-based mode multiplexers indeed excites higher order modes. We observe open-eye diagrams and error-free transmission (BER $< 10^{-12}$) in a 2-mode $\times$ 3-wavelength channels $\times$ 10 GB/s link. This type of on-chip mode- and wavelength-divison multiplexing can potentially support an aggregate data rate

of tens of terabits per second for ultra-high bandwidth chip-to-chip and intra-chip applications.

A work that we can pursue in the future is that we can integrate the mode multiplexing components and wavelength multiplexing components on the same chip without needing to use external components. For instance, in Figure 7.1, we can integrate on-chip microring modulators together with mode multiplexers at the transmitting end. This way, we do not have to use external lithium niobate modulators. On the receiver end, we can also integrate on-chip germanium photodetectors instead of external photodetectors to convert each received optical data (on a particular mode-wavelength channel) to electrical signals. The integrated MDM-WDM will increase the aggregate bandwidth by order of magnitude for ultra-high bandwidth applications.

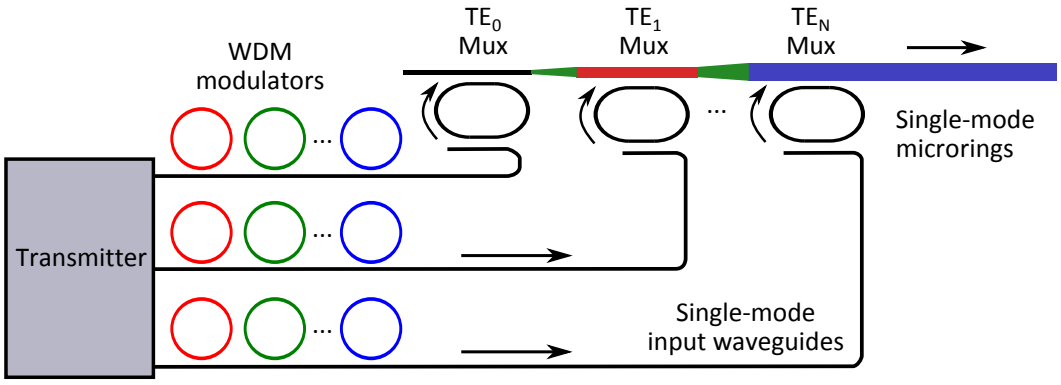

Figure 7.1: To integrate WDM microring modulators and MDM multiplexers on the same chip.

BIBLIOGRAPHY

[1] Sandvine Network Demographics. Global internet phenomena report: 1h 2013, 2013.

[2] Mario Paniccia, M Morse, and M Salib. Silicon photonics. *Springer, Berlin*, 2004.

[3] ITRS Roadmap. International technology roadmap for semiconductors, 2009 edn. *Executive Summary. Semiconductor Industry Association*, 2009.

[4] David A. B. Miller and Haldun M. Ozaktas. Limit to the bit-rate capacity of electrical interconnects from the aspect ratio of the system architecture. *Journal of parallel and distributed computing*, 41(1):42–52, 1997.

[5] Sasikanth Manipatruni, Qianfan Xu, Bradley Schmidt, Jagat Shakya, and Michal Lipson. High speed carrier injection 18 gb/s silicon micro-ring electro-optic modulator. In *Lasers and Electro-Optics Society, 2007. LEOS 2007. The 20th Annual Meeting of the IEEE*, pages 537–538. IEEE, 2007.

[6] Long Chen and Michal Lipson. Ultra-low capacitance and high speed germanium photodetectors on silicon. *Opt. Express*, 17(10):7901–7906, 2009.

[7] DJ Richardson, JM Fini, and LE Nelson. Space-division multiplexing in optical fibres. *Nature Photonics*, 7(5):354–362, 2013.

[8] Michal Lipson. Guiding, modulating, and emitting light on silicon-challenges and opportunities. *Journal of Lightwave Technology*, 23(12):4222, 2005.

[9] Alexander W Fang, Hyundai Park, Oded Cohen, Richard Jones, Mario J Paniccia, and John E Bowers. Electrically pumped hybrid algainas-silicon evanescent laser. *Opt. Express*, 14(20):9203–9210, 2006.

[10] Haisheng Rong, Ansheng Liu, Richard Jones, Oded Cohen, Dani Hak, Remus Nicolaescu, Alexander Fang, and Mario Paniccia. An all-silicon raman laser. *Nature*, 433(7023):292–294, 2005.

[11] David AB Miller. Optical interconnects to silicon. *Selected Topics in Quantum Electronics, IEEE Journal of*, 6(6):1312–1317, 2000.

[12] Lorenzo Pavesi and David J Lockwood. *Silicon photonics*, volume 1. Berlin: Springer, 2004.

[13] Richard Soref. The past, present, and future of silicon photonics. *Selected Topics in Quantum Electronics, IEEE Journal of*, 12(6):1678–1687, 2006.

[14] Mikhail Haurylau, Guoqing Chen, Hui Chen, Jidong Zhang, Nicholas A Nelson, David H Albonesi, Eby G Friedman, and Philippe M Fauchet. On-chip optical interconnect roadmap: challenges and critical directions. *Selected Topics in Quantum Electronics, IEEE Journal of*, 12(6):1699–1705, 2006.

[15] Fengnian Xia, Lidija Sekaric, and Yurii Vlasov. Ultracompact optical buffers on a silicon chip. *Nature Photonics*, 1(1):65–71, 2006.

[16] Qianfan Xu, Po Dong, and Michal Lipson. Breaking the delay-bandwidth limit in a photonic structure. *Nature Physics*, 3(6):406–410, 2007.

[17] Jaime Cardenas, Mark A Foster, Nicolás Sherwood-Droz, Carl B Poitras, Hugo LR Lira, Beibei Zhang, Alexander L Gaeta, Jacob B Khurgin, Paul Morton, Michal Lipson, et al. Wide-bandwidth continuously tunable optical delay line using silicon microring resonators. *Opt. Express*, 18(25):26525–26534, 2010.

[18] U Fischer, T Zinke, J-R Kropp, F Arndt, and K Petermann. 0.1 db/cm waveguide losses in single-mode soi rib waveguides. *Photonics Technology Letters, IEEE*, 8(5):647–648, 1996.

[19] S Lardenois, D Pascal, L Vivien, E Cassan, S Laval, R Orobtchouk, M Heitzmann, N Bouzaida, and L Mollard. Low-loss submicrometer silicon-on-insulator rib waveguides and corner mirrors. *Optics letters*, 28(13):1150–1152, 2003.

[20] MA Webster, RM Pafchek, G Sukumaran, and TL Koch. Low-loss quasi-planar ridge waveguides formed on thin silicon-on-insulator. *Applied Physics Letters*, 87(23):231108–231108, 2005.

[21] Po Dong, Wei Qian, Shirong Liao, Hong Liang, Cheng-Chih Kung, Ning-Ning Feng, Roshanak Shafiiha, Joan Fong, Dazeng Feng, Ashok V Krishnamoorthy, et al. Low loss shallow-ridge silicon waveguides. *Opt. Express*, 18(14):14474–14479, 2010.

[22] Isa Kiyat, Atilla Aydinli, and Nadir Dagli. High-q silicon-on-insulator

optical rib waveguide racetrack resonators. *Optics Express*, 13(6):1900–1905, 2005.

[23] LK Rowe, M Elsey, NG Tarr, AP Knights, and E Post. Cmos-compatible optical rib waveguides defined by local oxidation of silicon. *Electronics Letters*, 43(7):392–393, 2007.

[24] FY Gardes, GT Reed, AP Knights, G Mashanovich, PE Jessop, L Rowe, S McFaul, D Bruce, and NG Tarr. Sub-micron optical waveguides for silicon photonics formed via the local oxidation of silicon (locos). In *Proc. SPIE*, volume 6898, page 68980R, 2008.

[25] R Pafchek, R Tummidi, J Li, MA Webster, E Chen, and TL Koch. Low-loss silicon-on-insulator shallow-ridge te and tm waveguides formed using thermal oxidation. *Applied optics*, 48(5):958–963, 2009.

[26] Pieter Dumon, Wim Bogaerts, Vincent Wiaux, Johan Wouters, Stephan Beckx, Joris Van Campenhout, Dirk Taillaert, Bert Luyssaert, Peter Bienstman, Dries Van Thourhout, et al. Low-loss soi photonic wires and ring resonators fabricated with deep uv lithography. *Photonics Technology Letters, IEEE*, 16(5):1328–1330, 2004.

[27] Yurii A Vlasov, Sharee J McNab, et al. Losses in single-mode silicon-on-insulator strip waveguides and bends. *Opt. Express*, 12(8):1622–1631, 2004.

[28] Tai Tsuchizawa, Koji Yamada, Hiroshi Fukuda, Toshifumi Watanabe, Junichi Takahashi, Mitsutoshi Takahashi, Tetsufumi Shoji, Emi Tamechika, Sei-ichi Itabashi, and Hirofumi Morita. Microphotonics devices based on silicon microfabrication technology. *Selected Topics in Quantum Electronics, IEEE Journal of*, 11(1):232–240, 2005.

[29] Jan Niehusmann, Andreas Vörckel, Peter Haring Bolivar, Thorsten Wahlbrink, Wolfgang Henschel, and Heinrich Kurz. Ultrahigh-quality-factor silicon-on-insulator microring resonator. *Optics letters*, 29(24):2861–2863, 2004.

[30] Shijun Xiao, Maroof H Khan, Hao Shen, and Minghao Qi. Compact silicon microring resonators with ultra-low propagation loss in the c band. *Birck and NCN Publications*, page 259, 2007.

[31] Gottlieb S Oehrlein. Dry etching damage of silicon: a review. *Materials Science and Engineering: B*, 4(1):441–450, 1989.

[32] FP Payne and JPR Lacey. A theoretical analysis of scattering loss from planar optical waveguides. *Optical and Quantum Electronics*, 26(10):977–986, 1994.

[33] Kevin K Lee, Desmond R Lim, Lionel C Kimerling, Jangho Shin, and Franco Cerrina. Fabrication of ultralow-loss si/sio¡ sub¿ 2¡/sub¿ waveguides by roughness reduction. *Optics letters*, 26(23):1888–1890, 2001.

[34] Matthew Borselli, Thomas J Johnson, and Oskar Painter. Beyond the rayleigh scattering limit in high-q silicon microdisks: theory and experiment. *Optics Express*, 13(5):1515–1530, 2005.

[35] Jaime Cardenas, Carl B Poitras, Jacob T Robinson, Kyle Preston, Long Chen, and Michal Lipson. Low loss etchless silicon photonic waveguides. In *Lasers and Electro-Optics, 2009 and 2009 Conference on Quantum electronics and Laser Science Conference. CLEO/QELS 2009. Conference on*, pages 1–2. IEEE, 2009.

[36] Lian-Wee Luo, Gustavo S Wiederhecker, Jaime Cardenas, Carl Poitras, and Michal Lipson. High quality factor etchless silicon photonic ring resonators. *Optics Express*, 19(7):6284–6289, 2011.

[37] ATLAS User's Manual. Device simulation software. *SILVACO International, Santa Clara, CA*, 95054:20, 2008.

[38] Comsol Multiphysics. Comsol. *Inc., Burlington, MA, www. comsol. com*, 1994.

[39] Amnon Yariv. Universal relations for coupling of optical power between microresonators and dielectric waveguides. *Electronics Letters*, 36(4):321–322, 2000.

[40] Vilson R Almeida, Roberto R Panepucci, and Michal Lipson. Nanotaper for compact mode conversion. *Optics Letters*, 28(15):1302–1304, 2003.

[41] Paul E Barclay, Kartik Srinivasan, and Oskar Painter. Nonlinear response of silicon photonic crystal microresonators excited via an integrated waveguide and fiber taper. *Optics express*, 13(3):801–820, 2005.

[42] Payam Rabiei, William H Steier, Cheng Zhang, and Larry R Dalton. Polymer micro-ring filters and modulators. *Journal of Lightwave Technology*, 20(11):1968, 2002.

[43] Mohammad Soltani, Qing Li, Siva Yegnanarayanan, and Ali Adibi. Improvement of thermal properties of ultra-high q silicon microdisk resonators. In *Quantum Electronics and Laser Science Conference*. Optical Society of America, 2008.

[44] Vilson R Almeida and Michal Lipson. Optical bistability on a silicon chip. *Optics letters*, 29(20):2387–2389, 2004.

[45] L He, Y-F Xiao, C Dong, J Zhu, V Gaddam, and L Yang. Compensation of thermal refraction effect in high-q toroidal microresonator by polydimethylsiloxane coating. *Applied Physics Letters*, 93(20):201102–201102, 2008.

[46] Carsten Schmidt, Arkadi Chipouline, Thomas Käsebier, Ernst-Bernhard Kley, Andreas Tünnermann, and Thomas Pertsch. Thermal nonlinear effects in hybrid silica/polymer microdisks. *Optics letters*, 35(20):3351–3353, 2010.

[47] Ivan Grudinin, Hansuek Lee, Tong Chen, and Kerry Vahala. Compensation of thermal nonlinearity effect in optical resonators. *Optics Express*, 19(8):7365–7372, 2011.

[48] Mohammad Soltani. Novel integrated silicon nanophotonic structures using ultra-high q resonators. *PhD Dissertation*, 2009.

[49] Lian-Wee Luo, SW Gustavo, Jaime Cardenas, and Michal Lipson. High quality factor etchless silicon photonic ring resonators. In *Photonics Global Conference (PGC), 2010*, pages 1–3. IEEE, 2010.

[50] Vilson R Almeida, Carlos A Barrios, Roberto R Panepucci, and Michal Lipson. All-optical control of light on a silicon chip. *Nature*, 431(7012):1081–1084, 2004.

[51] M Soltani, Q Li, S Yegnanarayanan, and A Adibi. Improvement of thermal properties of ultra-high q silicon microdisk resonators. *Optics express*, 15(25):17305, 2007.

[52] Lian-Wee Luo, Gustavo S Wiederhecker, Kyle Preston, and Michal Lipson. Power insensitive silicon microring resonators. *Optics Letters*, 37(4):590–592, 2012.

[53] Joris Van Campenhout, William MJ Green, Xiaoping Liu, Solomon Assefa,

Richard M Osgood, and Yurii A Vlasov. Silicon-nitride surface passivation of submicrometer silicon waveguides for low-power optical switches. *Optics letters*, 34(10):1534–1536, 2009.

[54] Govind P Agrawal. *Fiber-optic communication systems*. Wiley, 2010.

[55] Ansheng Liu, Richard Jones, Ling Liao, Dean Samara-Rubio, Doron Rubin, Oded Cohen, Remus Nicolaescu, and Mario Paniccia. A high-speed silicon optical modulator based on a metal–oxide–semiconductor capacitor. *Nature*, 427(6975):615–618, 2004.

[56] William MJ Green, Michael J Rooks, Lidija Sekaric, Yurii A Vlasov, et al. Ultra-compact, low rf power, 10 gb/s silicon mach-zehnder modulator. *Opt. Express*, 15(25):17106–17113, 2007.

[57] Tao Yin, Rami Cohen, Mike M Morse, Gadi Sarid, Yoel Chetrit, Doron Rubin, and Mario J Paniccia. 31 ghz ge nip waveguide photodetectors on silicon-on-insulator substrate. *Opt. express*, 15(21):13965–13971, 2007.

[58] Yimin Kang, Han-Din Liu, Mike Morse, Mario J Paniccia, Moshe Zadka, Stas Litski, Gadi Sarid, Alexandre Pauchard, Ying-Hao Kuo, Hui-Wen Chen, et al. Monolithic germanium/silicon avalanche photodiodes with 340 ghz gain–bandwidth product. *Nature Photonics*, 3(1):59–63, 2008.

[59] Solomon Assefa, Fengnian Xia, and Yurii A Vlasov. Reinventing germanium avalanche photodetector for nanophotonic on-chip optical interconnects. *Nature*, 464(7285):80–84, 2010.

[60] K Sasaki, F Ohno, A Motegi, and T Baba. Arrayed waveguide grating of 70× 60 μm¡ sup¿ 2¡/sup¿ size based on si photonic wire waveguides. *Electronics Letters*, 41(14):801–802, 2005.

[61] Dazeng Feng, Wei Qian, Hong Liang, Cheng-Chih Kung, Joan Fong, LB Jonathan, and Mehdi Asghari. Novel fabrication tolerant flat-top demultiplexers based on etched diffraction gratings in soi. In *Group IV Photonics, 2008 5th IEEE International Conference on*, pages 386–388. IEEE, 2008.

[62] Junfeng Song, Q Fang, SH Tao, MB Yu, GQ Lo, and DL Kwong. Passive ring-assisted mach-zehnder interleaver on silicon-on-insulator. *Opt. Express*, 16(12):8359–8365, 2008.

[63] Brent E Little, Sai T Chu, Hermann A Haus, J Foresi, and J-P Laine. Mi-

croring resonator channel dropping filters. *Lightwave Technology, Journal of*, 15(6):998–1005, 1997.

[64] Sai T Chu, Brent E Little, Wugen Pan, Taro Kaneko, Shinya Sato, and Yasuo Kokubun. An eight-channel add-drop filter using vertically coupled microring resonators over a cross grid. *Photonics Technology Letters, IEEE*, 11(6):691–693, 1999.

[65] S Cao, J Chen, JN Damask, CR Doerr, L Guiziou, G Harvey, Y Hibino, H Li, S Suzuki, K-Y Wu, et al. Interleaver technology: comparisons and applications requirements. *Journal of Lightwave Technology*, 22(1):281, 2004.

[66] Kaname Jinguji. Synthesis of coherent two-port optical delay-line circuit with ring waveguides. *Lightwave Technology, Journal of*, 14(8):1882–1898, 1996.

[67] Kaname Jinguji and Manabu Oguma. Optical half-band filters. *Journal of lightwave technology*, 18(2):252, 2000.

[68] Manabu Oguma, Tsutomu Kitoh, Yasuyuki Inoue, Takayuki Mizuno, Tomohiro Shibata, Masaki Kohtoku, and Yoshinori Hibino. Compact and low-loss interleave filter employing lattice-form structure and silica-based waveguide. *Journal of lightwave technology*, 22(3):895, 2004.

[69] JF Song, SH Tao, Q Fang, TY Liow, MB Yu, GQ Lo, and DL Kwong. Thermo-optical enhanced silicon wire interleavers. *Photonics Technology Letters, IEEE*, 20(24):2165–2167, 2008.

[70] Junfeng Song, H Zhao, Q Fang, SH Tao, TY Liow, MB Yu, GQ Lo, and DL Kwong. Effective thermo-optical enhanced cross-ring resonator mzi interleavers on soi. *Opt. Express*, 16(26):21476–21482, 2008.

[71] S Darmawan, YM Landobasa, Pieter Dumon, Roel Baets, and MK Chin. Nested-ring mach–zehnder interferometer in silicon-on-insulator. *Photonics Technology Letters, IEEE*, 20(1):9–11, 2008.

[72] René-Jean Essiambre and Peter J Winzer. Transport challenges in optically-routed networks. In *Asia-Pacific Optical Communications*, pages 60212P–60212P. International Society for Optics and Photonics, 2005.

[73] Kazuhiro Oda, Norio Takato, Hiromu Toba, and Kiyoshi Nosu. A wide-band guided-wave periodic multi/demultiplexer with a ring resonator

for optical fdm transmission systems. *Lightwave Technology, Journal of*, 6(6):1016–1023, 1988.

[74] Christi K Madsen and Jian H Zhao. *Optical filter design and analysis: a signal processing approach*. Wiley, 2001.

[75] Amnon Yariv. Critical coupling and its control in optical waveguide-ring resonator systems. *Photonics Technology Letters, IEEE*, 14(4):483–485, 2002.

[76] Hidenori Takahashi, Patrick Carlsson, Kohsuke Nishimura, and Masashi Usami. Analysis of negative group delay response of all-pass ring resonator with mach-zehnder interferometer. *Photonics Technology Letters, IEEE*, 16(9):2063–2065, 2004.

[77] William MJ Green, Reginald K Lee, Guy A DeRose, Axel Scherer, and Amnon Yariv. Hybrid ingaasp-inp mach-zehnder racetrack resonator for thermooptic switching and coupling control. *Optics Express*, 13(5):1651–1659, 2005.

[78] Wesley D Sacher and Joyce KS Poon. Characteristics of microring resonators with waveguide-resonator coupling modulation. *Lightwave Technology, Journal of*, 27(17):3800–3811, 2009.

[79] Hugo LR Lira, Sasikanth Manipatruni, and Michal Lipson. Broadband hitless silicon electro-optic switch for on-chip optical networks. *Optics Express*, 17(25):22271–22280, 2009.

[80] Lian-Wee Luo, Salah Ibrahim, Arthur Nitkowski, Zhi Ding, Carl B Poitras, SJ Ben Yoo, and Michal Lipson. High bandwidth on-chip silicon photonic interleaver. *Opt. Express18 (22)*, pages 23079–23087, 2010.

[81] Nicolás Sherwood-Droz, Howard Wang, Long Chen, Benjamin G Lee, Aleksandr Biberman, Keren Bergman, Michal Lipson, et al. Optical 4x4 hitless slicon router for optical networks-on-chip (noc). *Opt. Express*, 16(20):15915–15922, 2008.

[82] K Jinguji, N Takato, A Sugita, and M Kawachi. Mach-zehnder interferometer type optical waveguide coupler with wavelength-flattened coupling ratio. *Electronics Letters*, 26(17):1326–1327, 1990.

[83] Joris Van Campenhout, William M Green, Solomon Assefa, and Yurii A Vlasov. Low-power, 2î2 silicon electro-optic switch with 110-nm band-

width for broadband reconfigurable optical networks. *Optics express*, 17(26):24020–24029, 2009.

[84] Radhakrishnan Nagarajan, Charles H Joyner, Richard P Schneider Jr, Jeffrey S Bostak, Timothy Butrie, Andrew G Dentai, Vincent G Dominic, Peter W Evans, Masaki Kato, Mike Kauffman, et al. Large-scale photonic integrated circuits. *Selected Topics in Quantum Electronics, IEEE Journal of*, 11(1):50–65, 2005.

[85] Bahram Jalali and Sasan Fathpour. Silicon photonics. *Lightwave Technology, Journal of*, 24(12):4600–4615, 2006.

[86] Jun Sakaguchi, Yoshinari Awaji, Naoya Wada, Atsushi Kanno, Tetsuya Kawanishi, Tetsuya Hayashi, Toshiki Taru, Tetsuya Kobayashi, and Masayuki Watanabe. 109-tb/s (7× 97× 172-gb/s sdm/wdm/pdm) qpsk transmission through 16.8-km homogeneous multi-core fiber. In *Optical Fiber Communication Conference and Exposition (OFC/NFOEC), 2011 and the National Fiber Optic Engineers Conference*, pages 1–3. IEEE, 2011.

[87] Mark D Feuer, Lynn E Nelson, Kazi S Abedin, Xiang Zhou, Thierry F Taunay, John F Fini, Benyuan Zhu, Rejoy Isaac, Roey Harel, Gil Cohen, et al. Roadm system for space division multiplexing with spatial superchannels. In *Optical Fiber Communication Conference*. Optical Society of America, 2013.

[88] Jun Sakaguchi, Benjamin J Puttnam, Werner Klaus, Yoshinari Awaji, Naoya Wada, Atsushi Kanno, Tetsuya Kawanishi, Katsunori Imamura, Harumi Inaba, Kazunori Mukasa, et al. 19-core fiber transmission of 19x100x172-gb/s sdm-wdm-pdm-qpsk signals at 305tb/s. In *National Fiber Optic Engineers Conference*. Optical Society of America, 2012.

[89] Hidehiko Takara, Akihide Sano, Takayuki Kobayashi, Hirokazu Kubota, Hiroto Kawakami, Akihiko Matsuura, Yutaka Miyamoto, Yoshiteru Abe, Hirotaka Ono, Kota Shikama, et al. 1.01-pb/s (12 sdm/222 wdm/456 gb/s) crosstalk-managed transmission with 91.4-b/s/hz aggregate spectral efficiency. In *European Conference and Exhibition on Optical Communication*. Optical Society of America, 2012.

[90] Dayou Qian, Ezra Ip, Ming-Fang Huang, Ming-jun Li, Arthur Dogariu, Shaoliang Zhang, Yin Shao, Yue-Kai Huang, Yequn Zhang, Xilin Cheng, et al. 1.05 pb/s transmission with 109b/s/hz spectral efficiency using hybrid single-and few-mode cores. In *Frontiers in Optics*. Optical Society of America, 2012.

[91] Sebastian Randel, Roland Ryf, Alberto Sierra, Peter J Winzer, Alan H Gnauck, Cristian A Bolle, René-Jean Essiambre, David W Peckham, Alan McCurdy, Robert Lingle, et al. 6× 56-gb/s mode-division multiplexed transmission over 33-km few-mode fiber enabled by 6× 6 mimo equalization. *Optics Express*, 19(17):16697–16707, 2011.

[92] Nobutomo Hanzawa, Kunimasa Saitoh, Taiji Sakamoto, Takashi Matsui, Shigeru Tomita, and Masanori Koshiba. Demonstration of mode-division multiplexing transmission over 10 km two-mode fiber with mode coupler. In *Optical Fiber Communication Conference and Exposition (OFC/NFOEC), 2011 and the National Fiber Optic Engineers Conference*, pages 1–3. IEEE, 2011.

[93] Roland Ryf, Sebastian Randel, Alan H Gnauck, Cristian Bolle, Alberto Sierra, Sami Mumtaz, Mina Esmaeelpour, Ellsworth C Burrows, René-Jean Essiambre, Peter J Winzer, et al. Mode-division multiplexing over 96 km of few-mode fiber using coherent 6× 6 mimo processing. *Journal of Lightwave Technology*, 30(4):521–531, 2012.

[94] Massimiliano Salsi, Clemens Koebele, Donato Sperti, Patrice Tran, Haik Mardoyan, Patrick Brindel, Sébastien Bigo, Aurélien Boutin, Frédéric Verluise, Pierre Sillard, et al. Mode-division multiplexing of 2× 100 gb/s channels using an lcos-based spatial modulator. *Journal of Lightwave Technology*, 30(4):618–623, 2012.

[95] Abdullah Al Amin, An Li, Simin Chen, Xi Chen, Guanjun Gao, William Shieh, Zhenhua Wang, Yonggang Wu, Zihuan Xia, Renchen Liu, et al. Dual-lp11 mode 4x4 mimo-ofdm transmission over a two-mode fiber. *Optics Express*, 19(17):16672–16679, 2011.

[96] Neng Bai, Ezra Ip, Yue-Kai Huang, Eduardo Mateo, Fatih Yaman, Ming-Jun Li, Scott Bickham, Sergey Ten, Jesús Liñares, Carlos Montero, et al. Mode-division multiplexed transmission with inline few-mode fiber amplifier. *Opt. Express*, 20(3):2668–2680, 2012.

[97] Roland Ryf, Sebastian Randel, Nicolas K Fontaine, Marc Montoliu, Ellsworth Burrows, Sethumadhavan Chandrasekhar, Alan H Gnauck, Chongjin Xie, Rene-Jean Essiambre, Peter Winzer, et al. 32-bit/s/hz spectral efficiency wdm transmission over 177-km few-mode fiber. In *Optical Fiber Communication Conference*. Optical Society of America, 2013.

[98] Ezra Ip, Ming-Jun Li, Yue-Kai Huang, Akihiro Tanaka, Eduardo Mateo, William Wood, Junqiang Hu, Yutaka Yano, and Konstantin Koreshkov.

146λx6x19-gbaud wavelength-and mode-division multiplexed transmission over 10x50-km spans of few-mode fiber with a gain-equalized few-mode edfa. In *National Fiber Optic Engineers Conference*. Optical Society of America, 2013.

[99] An Li, Abdullah Al Amin, Xi Chen, and William Shieh. Transmission of 107-gb/s mode and polarization multiplexed co-ofdm signal over a two-mode fiber. *Optics Express*, 19(9):8808–8814, 2011.

[100] Lian-Wee Luo, Noam Ophir, Christine Chen, Lucas H Gabrielli, Carl B Poitras, Keren Bergman, and Michal Lipson. Simultaneous mode and wavelength division multiplexing on-chip. *arXiv preprint arXiv:1306.2378*, 2013.

[101] Saeed Bagheri and W Green. Silicon-on-insulator mode-selective add-drop unit for on-chip mode-division multiplexing. In *Group IV Photonics, 2009. GFP'09. 6th IEEE International Conference on*, pages 166–168. IEEE, 2009.

[102] Yingyan Huang, Guoyang Xu, and Seng-Tiong Ho. An ultracompact optical mode order converter. *Photonics Technology Letters, IEEE*, 18(21):2281–2283, 2006.

[103] Y Kawaguchi and K Tsutsumi. Mode multiplexing and demultiplexing devices using multimode interference couplers. *Electronics Letters*, 38(25):1701–1702, 2002.

[104] Takui Uematsu, Yuhei Ishizaka, Yuki Kawaguchi, Kunimasa Saitoh, and Masanori Koshiba. Design of a compact two-mode multi/demultiplexer consisting of multimode interference waveguides and a wavelength-insensitive phase shifter for mode-division multiplexing transmission. *Journal of Lightwave Technology*, 30(15):2421–2426, 2012.

[105] Juerg Leuthold, R Hess, J Eckner, PA Besse, and H Melchior. Spatial mode filters realized with multimode interference couplers. *Optics letters*, 21(11):836–838, 1996.

[106] Maxim Greenberg and Meir Orenstein. Multimode add-drop multiplexing by adiabatic linearly tapered coupling. *Optics Express*, 13(23):9381–9387, 2005.

[107] Yunhong Ding, Jing Xu, Francesco Da Ros, Bo Huang, Haiyan Ou, and Christophe Peucheret. On-chip two-mode division multiplexing using

tapered directional coupler-based mode multiplexer and demultiplexer. *Optics express*, 21(8):10376–10382, 2013.

[108] Daoxin Dai, Jian Wang, and Yaocheng Shi. Silicon mode (de) multiplexer enabling high capacity photonic networks-on-chip with a single-wavelength-carrier light. *Optics letters*, 38(9):1422–1424, 2013.

[109] Byung-Tak Lee and Sang-Yung Shin. Mode-order converter in a multimode waveguide. *Optics letters*, 28(18):1660–1662, 2003.

[110] John D Love and Nicolas Riesen. Single-, few-, and multimode y-junctions. *Lightwave Technology, Journal of*, 30(3):304–309, 2012.

[111] Jeffrey B Driscoll, Richard R Grote, Brian Souhan, Jerry I Dadap, Ming Lu, and Richard M Osgood. Asymmetric y junctions in silicon waveguides for on-chip mode-division multiplexing. *Optics letters*, 38(11):1854–1856, 2013.

[112] Hermann A Haus. *Waves and fields in optoelectronics*, volume 1. Prentice-Hall Englewood Cliffs, NJ, 1984.

[113] Rajiv Ramaswami, Kumar Sivarajan, and Galen Sasaki. *Optical networks: a practical perspective*. Morgan Kaufmann, 2009.

[114] Fuad E Doany, Benjamin G Lee, Solomon Assefa, William MJ Green, Min Yang, Clint L Schow, Christopher V Jahnes, Sheng Zhang, Jonathan Singer, Victor I Kopp, et al. Multichannel high-bandwidth coupling of ultradense silicon photonic waveguide array to standard-pitch fiber array. *Lightwave Technology, Journal of*, 29(4):475–482, 2011.